

26726



National Library
of Canada

Bibliothèque nationale
du Canada

CANADIAN THESES
ON MICROFICHE

THÈSES CANADIENNES
SUR MICROFICHE

NAME OF AUTHOR NOM DE L'AUTEUR _____

TITLE OF THIS EDITION TITRE DE LA THÈSE _____

UNIVERSITY UNIVERSITÉ _____

DEGREE FOR WHICH THESIS WAS PRESENTED
GRADE POUR LEQUEL CETTE THÈSE FUT PRÉSENTÉE _____

YEAR THIS DEGREE CONFERRED ANNÉE D'OBTENTION DE CE GRADE _____

NAME OF SUPERVISOR NOM DU DIRECTEUR DE THÈSE _____

Permission is hereby granted to the NATIONAL LIBRARY OF
CANADA to microfilm this thesis and to lend or sell copies
of the film.

The author reserves other publication rights, and neither the
thesis nor extensive extracts from it may be printed or other-
wise reproduced without the author's written permission.

L'autorisation est, par la présente, accordée à la BIBLIOTHÈ-
QUE NATIONALE DU CANADA de microfilm cette thèse et
de prêter ou de vendre des exemplaires du film.

L'auteur se réserve les autres droits de publication ni la
thèse ni de longs extraits de celle-ci ne doivent être imprimés
ou autrement reproduits sans l'autorisation écrite de l'auteur.

DATED DATE _____ SIGNED SIGNÉ _____

PERMANENT ADDRESS RÉSIDENCE FIXE _____

THE UNIVERSITY OF ALBERTA

A NUMERICAL SIMULATION OF THE INITIATION
OF GRAVEL GROWTH

by



LAWRENCE HING-LUN CHENG

A THESIS

SUBMITTED TO THE FACULTY OF GRADUATE STUDIES AND RESEARCH
IN PARTIAL FULFILMENT OF THE REQUIREMENTS FOR THE DEGREE
OF MASTER OF SCIENCE

IN
METEOROLOGY

DEPARTMENT GEOGRAPHY

EDMONTON, ALBERTA

FALL, 1975

THE UNIVERSITY OF ALBERTA
FACULTY OF GRADUATE STUDIES AND RESEARCH

The undersigned certify that they have read,
and recommend to the Faculty of Graduate Studies and
Research, for acceptance, a thesis entitled ...A.....
.....PARTIAL SIMULATION OF THE INITIATION OF GRAUPEL.....
.....SUBMITTED.....
.....
submitted by LAW YEEHUNG-HUEN CHEUNG.....
in partial fulfilment of the requirements for the degree
of Master of Science in Meteorology.

Robert E. Johnson
Supervisor

Supervisor

.....
.....
.....

Date ... Aug. 28 / 75

ABSTRACT

The initiation of graupel growth was simulated by approximating a hexagonal ice crystal to be a very thin oblate spheroid. The flow of air passing oblate spheroids of ice with Reynolds numbers of 10 and 20 was calculated by solving the steady state Navier-Stokes equation in oblate spheroidal co-ordinates for spheroids with aspect ratio of 0.05. The flow field of air around the water drop was evaluated by two methods: solving the Navier-Stokes equation in spherical co-ordinates for spheres of $Re=0.1$ and using the analytical solution of Stokes flow for spheres of $Re=0.1$ as suggested by Le Clair et al (1970). The hydrodynamic interaction between an ice crystal and a water drop was simulated by using a superposition model of their combined flow fields. The trajectories of water droplets approaching ice spheroids were calculated by equations of motion which considered the gravitational force and the drag force on the bodies under consideration. These equations were integrated by the Hamming method and initiated by the Runge Kutta method. The maximum angle that water droplets would collect on the edge of an ice crystal was also investigated. The flow fields around an oblate spheroid of axis ratio 0.05 agreed quite well with those obtained by Pitter et al (1973) but the trajectories generated in the present study were

significantly different from those of Pitter et al (1974) in that droplets approaching the center of the spheroid were not forced out and past the spheroid. The maximum angle that water drops accreted on the edge of an ice crystal supported the theory of graupel growth suggested by List. Hence, a thin oblate spheroid was used to approximate a hexagonal ice crystal and the theory of Knight and Knight which involved corner effects on accretion patterns was not covered.

ACKNOWLEDGMENT

I wish to express my gratitude to the many people who have made this thesis possible.

I would first like to thank my departmental supervisor, Dr. R. B. Charlton, for his suggestions and review of this report. I also wish to thank Dr. E. Lozowski and Dr. N. Rajaratnam for their help and willingness to serve on the examination committee.

I wish to express my appreciation to the helpful discussions held with several of my colleagues.

My thanks go also to the Atmospheric Environment Service and the University of Alberta for financial support of this study.

Finally, I wish to thank my parents for their enthusiasm and encouragement. Without them this thesis would never have been a reality.

TABLE OF CONTENTS

	PAGE
ACKNOWLEDGEMENT	I
LIST OF TABLES	V
LIST OF FIGURES	VI
LIST OF COMMONLY USED SYMBOLS	VIII
ABSTRACT	X
CHAPTER	
I. INTRODUCTION AND LITERATURE REVIEWS	1
1.1 Objective of this dissertation	1
1.2 Graupel: its definitions and seasonal occurrence	3
1.3 Review of the theories of conical graupel formation	5
II. VISCOUS FLOW PAST ICE CRYSTALS AND CLOUD DROP	10
2.1 Introduction	10
2.2 The equation representing flow around a spheroid or sphere	11
2.3 Analytic solutions to flow around spheres and spheroids	15
2.4 Numerical solutions of flow around spheres and spheroids	21
2.5 Finite Difference equation formulation of flow around spheres and spheroids	23
2.5.1 Spheroids	23
2.5.2 Spheres	29

CHAPTER	PAGE
2.5.3 Formulation od boundary condition for spheroids	32
2.5.4 Formulation of boundary conditions for spheres	35
III. HYDRODYNAMIC INTERACTION OF AN ICE CRYSTAL AND A CLOUD DROPLET	37
3.1 Introduction	37
3.2 The mathematical model	38
3.3 Evaluation of the drag coefficient, the terminal velocity and the radius of body normal to the flow	49
IV. NUMERICAL PROCEDURES AND ASSUMPTIONS	58
4.1 Numerical procedures	58
4.2 Assumptions of the numerical simulation of the initiation of graupel growth	63
V. NUMERICAL RESULTS AND DISCUSSION	67
5.1 The flow field around an oblate spheroid (ice crystal)	67
5.2 Flow fields around spherical drops	77
5.3 Trajectories of water drops relative to an ice oblate spheroid	78
VI. CONCLUSIONS AND RECOMMENDATION	89
BIBLIOGRAPHY	91

	PAGE
APPENDIX I. COMPUTER PROGRAM FOR SOLUTION OF FLOW PAST AN OBLATE SPHEROID	98
APPENDIX II. COMPUTER PROGRAM FOR SOLUTION OF FLOW PAST A SPHERE	104
APPENDIX III. COMPUTER PROGRAM FOR DROP TRAJECTORIES PAST AN ICE CRYSTAL	108

LIST OF TABLES

Table	Description	Page
5.2.1	Reynolds Numbers, Drag Coefficient, Radius and Terminal Velocity of Spherical Water Drops in Atmosphere of -10°C, 700 mb	77

LIST OF FIGURES

Figure	Page
2.1 Oblate Spheroidal Coordinate System	25
2.2 Oblate Spheroidal Mesh System	30
2.3 Spherical Mesh System	33
3.1 Illustration of Grid-points for the Bi-quadratic Interpolation	48
3.2 Action of the Normal and Tangential Stresses on an "Element" of Area of the Sphere	51
5.1.1 Dimensionless Stream Function of an Oblate Spheroid of $Re = 20$ and $Ar = 0.05$	68
5.1.2 Dimensionless Vorticity Field around an Oblate Spheroid of $Ar = 0.05$ and $Re = 20$	69
5.1.3 Dimensionless Stream Function of an Oblate Spheroid of $Re = 10$ and $Ar = 0.05$	70
5.1.4 Dimensionless Vorticity of an Oblate Spheroid of $Re = 10$ and $Ar = 0.05$	71
5.1.5 Variation of the Surface Vorticity with Polar angle and Reynolds Numbers for Oblate Spheroids	73
5.1.6 Dimensionless Vertical Velocity of Air passing an Oblate Spheroid of $Re = 10$ and $Ar = 0.05$ due to the Motion of the Particle	74

Figure	Page
)	
5.1.7 Dimensionless Horizontal Velocity of Air passing an Oblate Spheroid of $Re = 10$ and $Ar = 0.05$	75
5.1.8 Variation with Reynolds Number of the Length of the Standing Eddy at the Downstream End of Oblate Spheroids of $Ar = 0.05$	76
5.2.1 Dimensionless Stream Function of a Sphere of $Re = .1$	79
5.2.2 Dimensionless Vorticity of a Sphere of $Re = .1$	80
5.3.1 Trajectories of a 5.91 microns Water Drop Relative to an Oblate Spheroid of Ice of $Re = 20$	82
5.3.2 Trajectories of a 19.14 microns Water Drop Relative to an Oblate Spheroid of Ice of $Re = 20$	83
5.3.3 Maximum angle that a 5.91 microns Water Drops formed on an Oblate Spheroid of $Re = 20$	85
5.3.4 Variation of Outer Maximum Angle that Water Drops of Various Reynolds Number Created on an Oblate Spheroid of $Re = 10$ and $Re = 20$	86

LIST OF COMMONLY USED SYMBOLS

A;C	Radial step size in spheroidal co-ordinate system; in spherical co-ordinate system
A_r	Axis ratio
a	Semi-major axis length of oblate spheroid; radius of sphere
B;D	Angular step size in spheroidal co-ordinate system; in spherical co-ordinate system
C_D	Drag coefficient
F	Modified vorticity
G	Modified vorticity
g	Acceleration of gravity
I	Index for angular co-ordinate
J	Index for radial co-ordinate
L	Subscript denoting oblate spheroid
P	Pressure
p	Size ratio
q	Ratio of density of crystal to density of drop
R	Position vector
r	Radial co-ordinate in spherical co-ordinate system
s	Surface area normal to the flow; subscript denoting sphere
t	Time
U	Velocity of medium due to motion of body
V	Velocity of body

\mathbf{v}	Velocity; $\mathbf{v} = v \mathbf{i} + w \mathbf{j}$
\mathbf{u}	Horizontal velocity, positive outward from disk; subscript: radial, r -component
z	Axial co-ordinate, positive downward; radial co-ordinate in modified spherical co-ordinate system; subscript: azimuthal, ϕ -component
Ω	Vorticity
ζ	Scalar vorticity
η	Polar co-ordinate in oblate spheroidal co-ordinate system
θ	Polar co-ordinate in spherical co-ordinate system
μ	Dynamic viscosity
ν	Kinematic viscosity
ξ	Radial co-ordinate in oblate spheroidal system
ρ_a	Density of air
Ψ	Stream function
∇	Nabla operator
*	Dimensional quantity

CHAPTER I INTRODUCTION AND LITERATURE REVIEW

1.1 Objective of this dissertation

It is believed that hailstones initiate from smaller pellets called 'graupel'. According to Fletcher (1969), hail represents an extreme case of cloud droplet accretion. There is also a qualitative difference between a hailstone and a graupel. A hailstone is formed by a fast accretion process during which the heat conducted away from the stone is not sufficient to freeze all the accreted water. Therefore, part of the water remains unfrozen and the stone becomes covered with a liquid skin which freezes relatively slowly to a dense, more or less transparent mass with air bubbles in it. On the other hand, when the accretion rate is slow, each collected cloud droplet freezes almost immediately upon impact. The resulting structure is porous and of low density and the particle formed is identified as a graupel or snow pellet. Since the Nineteenth Century, there have been many theories involving the formation of graupel. These theories will be reviewed in the later section. For almost two hundred years no widely accepted formulation of the development of graupel has ever been provided. The commonness of graupel in convective storms during the cool

days of spring suggests that they are one of the fastest-growing of all the precipitation forms and that they must be common within summer thundershower clouds although on warm summer days they would melt into raindrops before reaching the ground. They must also act as hailstone embryos in the cold regions of thunderclouds. As such, they are very important in explaining the effectiveness of rain-making or hail suppression mechanisms.

There is no strong reason to suppose that there are differences in origin between graupel of various shapes. Dissection of small hexagonal graupel always clearly reveals an ice crystal within. It is logical therefore to believe that graupel start as a rimed ice crystal in some way or another. As the ice crystal continues to rime it could either break up to form several graupel embryos (Knight and Knight, 1973) or it could continue to grow into a single graupel with an ice crystal at its center (List, 1958) which would be difficult to identify in a laboratory dissection. Since the shape of large graupel is often conical it would be of interest to know the side of the original ice crystal on which the riming originally begins, i.e. fanning out into the wind (Reynolds, 1876) to form the blunt end of the cone or pointing into the wind (Arenberg, 1941) to start the pointed end of the cone. The main interest of this thesis is to find the direction of growth of a graupel pellet during its early stage of growth by using a numerical model which can also calculate

the angle of the point of graupel which, from reports in the literature, varies from 60° to 120° (Arenberg, 1941; Flogel, 1877). Wilkins and Auer (1970) reported that the onset of riming is mainly on plane ice crystals between 300 microns and 800 microns in diameter. These atmospheric ice crystals typically have Reynolds numbers less than 100 and greater than 1 which lie between the values described by Stokes and potential theories. It is, therefore, necessary to obtain solutions for the viscous flow past ice crystals at intermediate Reynolds numbers in order to calculate reasonable flow fields and hydrodynamic interactions between ice crystal and approaching water drops.

1.2 Graupel: its definitions and seasonal occurrence

The word graupel is frequently used by cloud physicists and its definition is still vague. Evidently it is derived from the German word 'Graupeln' for hulled barley or hulled grain. It is usually translated in German-English dictionaries as 'sleet', an ill-defined term in the English language with various regional interpretations, or 'ice pellet' which is clearly contrary to 'snow pellets' or 'soft hail' as graupel is defined by Mason (1971). According to Mason, the International Commission for Ice and Snow recommended, in 1956, the definition of graupel should be: "Snow pellets (soft hail, graupel). These are white, opaque, rounded or conical pellets of diameter up to

about 6 mm. They are composed largely of small cloud droplets individually frozen together, have a low density, and are readily crushed. They may break up on striking a hard surface."

According to Nakaya (1951, 1954), Schaefer (1951) and Magono and Lee (1966), graupel are the extreme stage of riming of ice particles (usually snow crystals) before further accretion leads to harder growth, making hail. Some hailstone embryos and small hailstones are most probably soaked or partially melted and then refrozen graupel (List, 1958).

There are three typical forms of graupel: hexagonal, conical and lumpy or granular (Nakaya, 1951; Schaefer, 1951; Magono and Lee, 1966). Hexagonal graupel are obviously heavily rimed snow or ice crystals (rimed plates and stellar dendrites) which retain their general shape. Conical graupel are sometimes pointed and sometimes not and they occur more frequently than the other two types in convective thunderstorms. Lumpy graupel may be rimed snow crystals or ice crystals or parts thereof which tumble along in the process of riming.

Very often, the words snow crystal and ice crystal are used interchangeably. In fact, there is a difference between the two terms. Ice crystal refers to ice particles grown in an ice-supersaturated atmosphere by diffusion of water vapour to their growing surfaces, and

may exist as individual units of simple geometric shape, for example hexagonal prismatic columns (needles and prisms) and hexagonal plates, or, under suitable conditions, may grow into complex richly-branched forms. Snow crystal includes all solid precipitation in nature. They can grow by any of the three possible process: (1) growth by diffusion in the presence of supercooled drops, (2) growth by collision with other solid hydrometeors in the atmosphere, or (3) growth by coalescence of supercooled water droplets. Thus, the term snow crystal can be implied for ice crystal, but not vice versa. The above definitions of these two terms will be used in this study.

Graupel fall to the ground during three rather distinct seasonal weather phenomena. These are (1), heavy winter convective snow storms (2), convective storms in the early Spring; and (3), as hailstone embryos in Summer. It is rare to find hexagonal graupel in vigorous convective storms or occurring as hailstone embryo, (Knight and Knight, 1973) and conical graupel predominates in all three of the above storms.

1.3 Review of the theories of conical graupel formation.

The origin of the three seasonal occurrences of graupel mentioned above is probably quite similar. Every investigator agrees and the observational evidence shows that graupel are a result of riming; i.e. accretion of

supercooled water droplets in conditions such that each drop retains its shape when it freezes on impact. The droplet becomes a little ball of ice adhering to the object being rimed.

While the initiation of snow pellets, or graupel, is generally understood to be due to the riming of settling snow crystals, there are certain features in their development, particularly the conical form, which have not achieved a widely acceptable description.

Arenberg (1941) proposed that conical graupel begin as large snow crystals that become heavily rimed on being carried upwards to the top of cumulus cloud. If the flakes are flat hexagonal plate of various degrees of intricacy they would fall with their flat side facing downward vertically as rime continues to collect on their under side. First they would rime along the edges and then over the entire surfaces. The deposit gradually builds up until the point of the cone is formed. Arenberg admits that this is not the most stable fall attitude for a cone, i.e. pointed side down, but he points out that it is the second most stable attitude. It could be assumed that during the early growth stages when there is little difference in stability between the two stable fall modes that the pointed downward mode could be maintained for long periods if no disturbance occurs. His proposition explains also the observation that graupel are least dense at the top and harder at the base.

Holroyd (1964) suggests that conical graupel start as rimed clusters of two to six rimed needle crystals, as deduced from observations. He proposed that needles falling in their usual horizontal orientation would tilt and descend vertically as rime build-up makes one end heavier than the other. The increasing deposits of rime on the downward end keeps the needles in that orientation. If two rimed needles coalesce they would attach at the bases where their dimensions are greatest and the air flowing past would then force the trailing tips together. Further riming or more coalescence with other rimed needles would develop a conical shape. A conical graupel would have been formed.

While most investigators believe that conical graupel start as ice crystals, studies by Weickmann (1953) and Nagano (1953) suggested that conical graupel can start directly from frozen droplets or tiny, irregular ice particles. Their proposition was based mainly on the fact that snow crystals are seldom recognized within conical hail embryos.

Contrary to Arenberg's pointing downward theory, most writers since the very early investigation of graupel by Reynolds (1876) expect riming to lead to shapes that grow broader on the bottom side, i.e. toward the approaching air and cloud droplets. In such a growth mode, the original snow crystals must then be near the tips of the graupel,

not at the blunt ends. List (1958) shows photographs to illustrate that ice crystals can be found near the pointed ends and he (1960) also points out that about 40 or 50 percent of the graupel he examined in Switzerland had originating snow crystals as centers. If this is the actual way of most graupel growth, for the pointed ends to be truly pointed some capture must occur on the down wind side of the original snow crystal, i.e., in the wake.

Most recently, Knight and Knight (1973) hypothesize that conical graupel should form as follows. A planar or dendritic ice crystal, falling in its most stable orientation with its axis vertical, tends to rime first at the edges of the windward side, in particular it rimes more at the six corners. The riming starts at points of the crystal and fans out into the wind. Further riming on the crystal which is still falling in the same attitude increases the size of the conical shape deposits attached by their tips to each of the six corners of the snow crystal. If turbulence exists or the snow crystal changes its orientation, these conical deposits would break off due to air stress. Graupel could then originate as single cones, which have broken off from the corners of ice crystals, or as groups of cones that have grown together and coalesced at their broader ends. This would explain the difficulty in finding ice crystals within graupel particles.

The fact that the collection efficiency is the

greatest at the edges of the downward facing side of a falling snow crystal of size 150 to 400 microns has been justified by Pitter and Fruppacher (1974) through numerical investigation. Sasyo (1971), after careful study of the formation of precipitation by the aggregation of snow particles and the accretion of cloud droplets on snowflakes, also provided evidence that cloud droplets coalesce in greater amounts at the corners than over the other parts of snow crystal. Using supported models of hexagonal plates of diameter 0.5 cm and 1.0 cm placed in saturated air moving at various relative velocities, he found that the frontal surface captures water droplets of various sizes while the rear surface captures only water droplets smaller than 10 microns in diameter. Furthermore, he discovered that there is a tendency to increase the number of droplets captured by the frontal surface with increasing air velocity at the same time as droplets captured by the rear surface increased. It seems that Knight and Knight's theory of graupel growth is supported by these studies of Sasyo.

2.1 Introduction

The first step in this numerical study is to calculate flow fields around ice crystals and cloud droplets. The second step is to calculate the motion of a cloud droplet as it approaches an ice crystal. There are numerous reports of experimental and theoretical work in the literature on the characteristics of the flow of a viscous fluid past a single sphere and on the forces between two hydrodynamically interacting spheres. (Le Clair et al, 1970, 1972; Namieiec et al, 1967; Shafirir et al, 1970). In contrast, no work has been done on hexagonal discs and relatively little on planar objects. Jayaweera and Cottis (1969), and List and Schemenauer (1971) experimentally showed that the hydrodynamic behaviour of a simple hexagonal plate can be approximated with sufficient accuracy by that of a circular disk. Pitter et al (1973) showed that the hydrodynamic behaviour of a thin oblate spheroid is essentially the same as that of a ~~circular~~ disk of the same thickness to width ratio (aspect ratio). The flow field past a disk can most easily be calculated if its shape is approximated as a thin oblate shperoid of variable aspect ratio. The flow field past a spherical cloud droplet would be equivalent to an aspect ratio equalling 'one'. The

interaction of the calculated flow fields around the plate and the sphere should allow one to calculate the trajectory of a cloud droplet as it is approaches and collides with an ice crystal.

2.2 The equations representing flow around a spheroid or sphere

The motion of a system can be best described by Newton's second law as:

(mass of system)(acceleration of the system)=net force of the system. For a fluid parcel, the net force can be classified as the body (gravity, etc.) force and the surface force. Newton's second law can then be expressed in an equational form as,

$$\text{density } \frac{D\bar{V}}{Dt} = \frac{\text{net body force}}{\text{volume}} + \frac{\text{net surface force}}{\text{volume}},$$

where the time derivative of the velocity is the acceleration ($\frac{D\bar{V}}{Dt}$) of the fluid parcel. For a Stokesian fluid, such as air, water and oil, the net surface force on a fluid parcel per unit volume is formed by two forces; the pressure gradient force and the viscous friction. If the net body force per unit volume is denoted by \bar{F} , and the fluid is incompressible, then the equation of motion and continuity

equation can be written as,

$$\rho \frac{D\bar{V}^*}{Dt} = \bar{P} - \nabla \cdot \bar{V}^* + \mu^* \nabla^2 \bar{V}^* \quad (2.1)$$

$$\bar{V} \cdot \bar{V}^* = 0 \quad (2.2)$$

where \bar{P}^* and \bar{V}^* are the dimensional pressure and velocity, ρ and μ^* are the dimensional density and dynamic viscosity of the fluid. The differential operators: gradient ∇ , divergence $\nabla \cdot$ and Laplacian ∇^2 , in generalized curvilinear orthogonal co-ordinates are:

$$\nabla = \frac{\hat{a}_1}{h_1} \frac{\partial}{\partial q_1} + \frac{\hat{a}_2}{h_2} \frac{\partial}{\partial q_2} + \frac{\hat{a}_3}{h_3} \frac{\partial}{\partial q_3}, \quad (2.3)$$

$$\begin{aligned} \nabla \cdot \bar{V} &= \frac{1}{h_1 h_2 h_3} \left[\frac{\partial}{\partial q_1} (v_1 h_2 h_3) + \frac{\partial}{\partial q_2} (v_2 h_3 h_1) + \right. \\ &\quad \left. \frac{\partial}{\partial q_3} (v_3 h_1 h_2) \right] \end{aligned} \quad (2.4)$$

and

$$\begin{aligned} \nabla^2 &= \frac{1}{h_1 h_2 h_3} \left[\frac{\partial}{\partial q_1} \left(\frac{h_2 h_3}{h_1} \frac{\partial}{\partial q_1} \right) + \right. \\ &\quad \left. \frac{\partial}{\partial q_2} \left(\frac{h_3 h_1}{h_2} \frac{\partial}{\partial q_2} \right) + \frac{\partial}{\partial q_3} \left(\frac{h_1 h_2}{h_3} \frac{\partial}{\partial q_3} \right) \right] \end{aligned} \quad (2.5)$$

q_1, q_2, q_3 , are the curvilinear co-ordinates;

$\hat{a}_1, \hat{a}_2, \hat{a}_3$ are unit direction vectors and h_1, h_2, h_3

are the metric coefficients. The values of the metric coefficients used in the co-ordinate system of this study are given in section 2.4.1. If the fluid is steady state equation (2.1) becomes:

$$\bar{V}^* \cdot \nabla \bar{V}^* - \mu^* \nabla^2 \bar{V} = - \nabla P + \bar{F} \quad (2.6)$$

The calculation of the flow fields in this study is restricted to axial symmetry, i.e. there are no variations with the azimuthal angle. A three dimensional approach would be much more complicated. Once axial symmetry is imposed, i.e. $\frac{\partial}{\partial q_3} = 0$ and $\bar{V}_3 = \text{constant}$, one can define a Stokes' stream function Ψ^* which will satisfy the continuity equation (2.2) automatically, and use it as one of the dependent variables to eliminate the pressure gradient term. If the primitive variables, velocity and pressure, are used; special care must be taken to satisfy the continuity equation as accurately as possible. The stream function Ψ^* can be defined in terms of velocity in the two dimensional curvilinear co-ordinate system with q_1 as the radial and q_2 as the angular coordinates:

$$\left. \begin{aligned} V^*_{q_1} &= \frac{-1}{h_2 h_3} \frac{\partial \Psi^*}{\partial q_2} \\ V^*_{q_2} &= \frac{1}{h_1 h_3} \frac{\partial \Psi^*}{\partial q_1} \end{aligned} \right\} \quad (2.7)$$

The major dependent variable is the vorticity $\bar{\Omega}^* = \nabla \times \bar{V}^*$, because of the symmetry, the only velocity component that survives is the one in the azimuthal direction. This component is designated by ζ^* .

If a curl operator is applied to equation (2.6) the pressure gradient term becomes zero, i.e. $\nabla \times \nabla P = 0$ and the operation of the curl on the velocity vector in a axisymmetric curvilinear coordinates gives:

$$\nabla \times \bar{V}^* = \frac{1}{h_1 h_2} \left[\frac{\partial h_2 V_{q_1}^*}{\partial q_1} - \frac{\partial h_1 V_{q_2}^*}{\partial q_2} \right] \hat{a}_3 = \zeta^*, \quad (2.8)$$

then equation (2.6) becomes:

$$V^* E^{*2} E^{*2} \Psi^* = \frac{1}{h_1 h_2 h_3} \frac{\partial (\Psi^*, E^{*2} \Psi^*/h_3^2)}{\partial (q_1, q_2)} \quad (2.9)$$

where $\zeta^* = \frac{1}{h_1 h_2} \left[\frac{\partial}{\partial q_1} \left(\frac{h_2}{h_1 h_3} \frac{\partial \Psi^*}{\partial q_1} \right) + \frac{\partial}{\partial q_2} \left(\frac{h_1}{h_2 h_3} \frac{\partial \Psi^*}{\partial q_2} \right) \right]$.

The operator $\partial(\Psi^*, E^{*2} \Psi^*/h_3^2)/\partial(q_1, q_2)$ is a Jacobian and it is denoted by the determinant as follows:

$$\frac{\partial(\Psi^*, E^{*2} \Psi^*/h_3^2)}{\partial(q_1, q_2)} = \begin{vmatrix} \frac{\partial \Psi^*}{\partial q_1} & \frac{\partial(E^{*2} \Psi^*/h_3^2)}{\partial q_2} \\ \frac{\partial(E^{*2} \Psi^*/h_3^2)}{\partial q_1} & \frac{\partial \Psi^*}{\partial q_2} \end{vmatrix} \quad (2.10)$$

The other operator E^* is given by:

$$E^{*2} = \frac{h_3}{h_1 h_2} \left[-\frac{\partial}{\partial q_1} \left(\frac{h_2}{h_1 h_3} \frac{\partial}{\partial q_1} \right) + \frac{\partial}{\partial q_2} \left(\frac{h_1}{h_2 h_3} \frac{\partial}{\partial q_2} \right) \right] \quad (2.11)$$

The symbol \mathcal{V}^* in equation (2.9) is the kinematic viscosity and it is defined as the dynamic viscosity μ^* divided by the density ρ . Equation (2.9) is of the fourth order in Ψ^* and it is not linear because of the presence of the inertial term on the right hand side. In general, the equation is called the Navier-Stokes equation in two dimensions.

2.3 Analytic Solutions to Flow Around Spheres and Spheroids

The oldest formulation of flow past an obstacle is called Stokes flow (1851) or creeping flow. The inertial effects are assumed to be negligible in comparison with those of viscosity. The Navier-Stokes equation reduces to:

$$E^{*2} E^{*2} \Psi^* = 0 \quad (2.12)$$

Such a simplification of the equation of motion is very substantial, since the equation of motion thus becomes linear.

The general solution of the creeping flow equation (2.12) for spherical (r, θ) and spheroidal coordinates (ξ, η) was given by Campson (1891). For spheres,

$$\begin{aligned}\Psi^*(r, \theta) = & \sum_0^{\infty} (A_n r^n + B_n r^{-n+1} + C_n r^{n+2} + D_n r^{-n+3}) I_n(\gamma) \\ & + \sum_0^{\infty} (A'_n r^n + B'_n r^{-n+1} + C'_n r^{n+2} \\ & + D'_n r^{-n+3}) H_n(\gamma),\end{aligned}\quad (2.13)$$

where A_n, B_n, C_n, D_n and the corresponding primed terms are constants and γ is defined as $\gamma = \cos \theta$. $I_n(\gamma)$ and $H_n(\gamma)$ are Gegenbauer functions of order n and degree -1 of the first and second type respectively. The constants are evaluated from the applicable boundary conditions. For the no-slip condition at the sphere and a uniform stream function at infinity, equation (2.13) becomes:

$$\Psi^* = \frac{1}{4} U^* a^2 \left(\frac{a}{r} + \frac{3r}{a} + \frac{2r^2}{a^2} \right) \sin^2 \theta, \quad (2.14)$$

where a is the radius of the sphere and U^* is the speed of the undisturbed stream. The drag force experienced by the sphere can be given as:

$$F = 4\pi \mu^* D_2, \quad (2.15)$$

D_p is the constant from equation (2.15). It is equal to $\frac{3}{2} a^{\frac{1}{2}}$. The dimensional surface pressure is given by:

$$P^* = \frac{1}{2} \rho U^* (1 + \frac{6}{Re} \cos \theta). \quad (2.16)$$

For Stokes flow in the spheroidal coordinates (ξ, η) : Ψ^* was given by Lampropoulos (1961) and discussed in Nasilyah (1973) as:

$$\begin{aligned} \Psi^* = & C_0 + D_1 \tau + I_2(\varphi) \left\{ B_1 \tau + C_2 I_2(\tau) + D_2 H_2(\tau) \right. \\ & \left. + B_4' H_4(\tau) \right\} + I_3(\varphi) \left\{ B_3 + D_3 H_3(\tau) + B_5 H_5(\tau) \right\} \\ & + I_4(\varphi) \left\{ B_4 H_2(\tau) + D_4 H_4(\tau) + B_6' H_6(\tau) \right\} \end{aligned} \quad (2.17)$$

where $\tau = \cosh \xi$; $\varphi = \cos \eta$; $I_n(\varphi)$ are the Gegenbauer functions of the first type with corresponding orders; $H_n(\varphi)$ are the Gegenbauer functions of the second type with corresponding orders; and all the C's, B's and D's with or without primes are constant coefficients dependent on boundary conditions. For an oblate spheroid one obtains:

$$\Psi^* = I_n(\varphi) \left\{ i B_2 \lambda + C_2 I_2(i \lambda) + D_2 H_2(i \lambda) \right\}, \quad (2.18)$$

where $i = \sqrt{-1}$, the imaginary unit, and $\lambda = \sinh \xi$. The

spheroidal coordinates are given as in figure (2.1). For the no-slip condition at the spheroid surface and a uniform stream condition at infinity, the stokes stream function given by equation (2.18) becomes:

$$\Psi^* = \frac{1}{2} U^* c^2 (\lambda^2 + 1)(1 - \varphi^2)$$

$$\left\{ 1 - \frac{[\lambda/(\lambda^2+1)] - [(\lambda_a^2-1)/(\lambda^2+1)] \cot^{-1} \lambda}{[\lambda_a/(\lambda_a^2+1)] - [(\lambda_a^2-1)/(\lambda_a^2+1)] \cot^{-1} \lambda_a} \right\}, \quad (2.19)$$

where subscript 'a' denotes the surface and c the focal length of the spheroid.

The drag force experienced by the spheroid is then given as;

$$F = 6\pi \mu^* U^* a_e K, \quad (2.20)$$

where a_e is the major axis radius of the spheroid, and for an oblate spheroid,

$$K = \frac{1}{\frac{3}{4}\sqrt{\lambda_a^2 + 1} [\lambda_a - (\lambda_a^2 - 1) \cot^{-1} \lambda_a]}. \quad (2.21)$$

The dimensionless surface pressure distribution for Stokes flow past an oblate spheroid is given by

$$P = 1 + \frac{6K}{Re} \left(\frac{\lambda_a^2 + 1}{\lambda_a^2 + \cos^2 \eta} \right) \cos \eta. \quad (2.22)$$

In the case where the inertial effects of the flow are small but not negligible, Stokes solution can no longer be considered valid at points far away from the surface unless $Re \rightarrow 0$. At points near the body the inertial forces tend to vanish. This means that Stokes approximation for the flow field is not uniformly valid throughout as it breaks down at a large distance from the surface. The inertial terms are thus, to some extent, taken into account. Goldstein (1929) developed Oseen's (1915) perturbation method of approximating the drag force experienced by a sphere in non-Stokes flow, giving the drag force as a series in Reynold number:

$$F = 6\pi\mu^*aU^* \left[1 + \frac{3}{16}Re - \frac{19Re^2}{1280} + \frac{71Re^3}{20480} - \frac{30179Re^4}{34406400} + \frac{122519Re^5}{56074240} - \dots \right] \quad (2.23)$$

The first term of the above equation is the value given by Stokes (equation 2.15), while the second term is that given by Oseen. Unfortunately, the equation (2.23) is valid only for Reynold number up to and including 2.

Aoi (1955), maintaining conformity with the corresponding creeping flow solution, derived the expression for the total drag force on an oblate spheroid

as:

$$F = 6\pi\mu^*U^*\alpha e K \left\{ 1 + \frac{3KRe}{16} \right\} \quad (2.24)$$

where K and αe are the same as those in equation (2.18), while the Re is based on the diameter of the major axis of the spheroid. Aoi (1955) also developed the ratio of the form (pressure) drag to the skin (friction) drag on an oblate spheroid which is given by:

$$\frac{F_F}{F_s} = \frac{(\lambda_a^2 + 1)(1 - \lambda_a \cot^{-1} \lambda_a)}{1 - (\lambda_a^2 + 1)(1 - \lambda_a \cot^{-1} \lambda_a)} \quad (2.25)$$

Thus, according to the above expression, though the form drag and skin drag of the oblate spheroid depend on its size, the ratio of the drag forces is independent of the Reynolds number.

Proudman and Pearson (1957), instead of obtaining perturbation fields, seek separate asymptotic solutions which are locally valid in separate regions near to, and far from, the body. These inner and outer solutions are each determined by asymptotically matching them in their common domain of validity. The expression for the drag force experienced by a sphere placed in a uniform stream is given by:

$$F = 6\pi\mu^*U^*\alpha \left\{ 1 + \frac{3}{16}Re + \frac{9}{160}Re^2 \ln\left(\frac{Re}{2}\right) \right\}. \quad (2.26)$$

Breath (1961) extended the technique of Proudman and Pearson to apply to ellipsoids of revolution, both prolate and oblate. The expression for the drag force on an oblate spheroid can then be rewritten in the form:

$$F = 6\pi \mu^* U^* a_e K \left\{ 1 + \frac{3}{16} Re + \frac{9}{160} K^2 Re^2 \ln \frac{Re^2}{2} \right\}, \quad (2.27)$$

with a_e and K identical to those in equation (2.20). Once again, the first term in the above equation is for creeping flow, the second being Oseen's extension while the third is new. For a sphere, $K=1$ and the equation (2.27) becomes identical to that of Proudman and Pearson (equation 2.26).

2.4 Numerical Solutions of Flow Around Spheres and Spheroids.

The solution of the Navier-Stokes equation via Stokes, Oseen and Proudman and Pearson fail to describe the flow for Reynolds number greater than 2. Approximate solutions using the Galerkin method (Snyder, Spriggs and Stewart, 1964) have been tried by numerous investigators. This method first assumes trial functions, and an approximate solution is then obtained by determining the trial function parameters such as to satisfy the Navier-Stokes equation and the boundary conditions as closely as possible. The optimum trial functions may be determined by variational

calculus or by error distribution methods. The success of this method depends strongly on the choice of the trial polynomial. Hamielec and Johnson (1962), Hamielec et al (1963) used this technique to evaluate the viscous flow around fluid spheres of Reynolds number from 10 to 5000.

Jenson (1959), in his work on spheres, solved the Navier-Stokes equation by splitting it into two simultaneous second order equations representing the stream function and the vorticity. Jenson approximated the vorticity near the surface by a third order polynomial and he used an exponential transformation for radial distance from the surface. Le.Clair and Hamielec (1970) and Hamielec et al (1967) extended Jenson's technique with the aid of digital computers to intermediate and higher Reynolds number.

Rimon and Lugt (1967), using a time-dependent numerical technique, calculated the viscous flow around an oblate spheroid. Unfortunately, their results were limited to $Re = 10$ and $Re = 100$. Masliyah and Epstein (1971) using an adaptation of the relaxation technique of Jenson, obtained numerical solutions of the Navier-Stokes equation for axisymmetric flow past oblate spheroids at particular Reynolds numbers up to 100 and of aspect ratios 0.2 to 0.999. Most recently, Pitter et al (1973) followed the numerical method of Woo (1971), adapted to oblate spheroids and obtained quite satisfactory solutions

of the steady-state Navier-Stokes equation of viscous flow past an oblate spheroidal obstacle of Reynolds numbers 0.1 to 100 and of axis ratio 0.05 to 0.2. Their numerical results for oblate spheroids of aspect ratio 0.2 agree well with those of Masliyah and Epstein (1971).

2.5 Finite Difference Equation Formulation of Flow Around Spheres and Spheroid.

The choice of spherical (for water drops) and spheroidal (for ice crystals) coordinates in this study facilitates the formulation of the boundary conditions. In addition, if these coordinates are given exponential properties, a fine lattice near the surface of the particle and a coarse lattice far away from the body can be formulated. As the influence of the particle on the flow is mainly manifested near the particle's surface and as this influence decreases with distance from the surface, the lattice thus produced serve the purpose of giving a desired lattice gradation.

2.5.1 Spheroids

The Navier-Stokes equation for steady-state axisymmetric or two-dimensional flow, expressed in orthogonal curvilinear coordinates in terms of the dimensional stream

function ψ^* is:

$$\nu^* E^{*2} E^{*2} \psi^* = \frac{1}{h_1 h_2 h_3} \frac{\partial(\psi^*, E^* \psi^*/h_3^2)}{\partial(q_1, q_2)} \quad (2.9)$$

and

$$E^{*2} = \frac{h_3}{h_1 h_2} \left[\frac{\partial}{\partial q_1} \left(\frac{h_2}{h_1 h_3} \frac{\partial}{\partial q_1} \right) + \frac{\partial}{\partial q_2} \left(\frac{h_1}{h_2 h_3} \frac{\partial}{\partial q_2} \right) \right] \quad (2.11)$$

In spheroidal coordinates,

$$q_1 = \xi \quad h_1 = h_2 = c (\sinh^2 \xi + \cos^2 \eta)^{1/2}$$

$$q_2 = \eta \quad h_3 = c \cosh \xi \sin \eta$$

where ξ is the radial and η is the angular coordinates as in figure (2.1) and C is the focal length of the system, i.e. the distance between the two foci of the oblate spheroid, then, equation (2.9) and equation (2.11) become:

$$\nu^* E^{*2} E^{*2} \psi^* = \frac{(\cosh \xi \sin \eta)^{-1}}{C^3 (\sinh^2 \xi + \cos^2 \eta)} \cdot \frac{\partial(\psi^*, E^* \psi^*/C^2 \cosh^2 \xi \sin^2 \eta)}{\partial(\xi, \eta)} \quad (2.28)$$

and

$$E^{*2} = \frac{1}{C^3 (\sinh^2 \xi + \cos^2 \eta)} \left[\frac{\partial^2}{\partial \xi^2} - \tanh \xi \frac{\partial}{\partial \xi} + \frac{\partial^2}{\partial \eta^2} - \cot \eta \frac{\partial}{\partial \eta} \right] \quad (2.29)$$

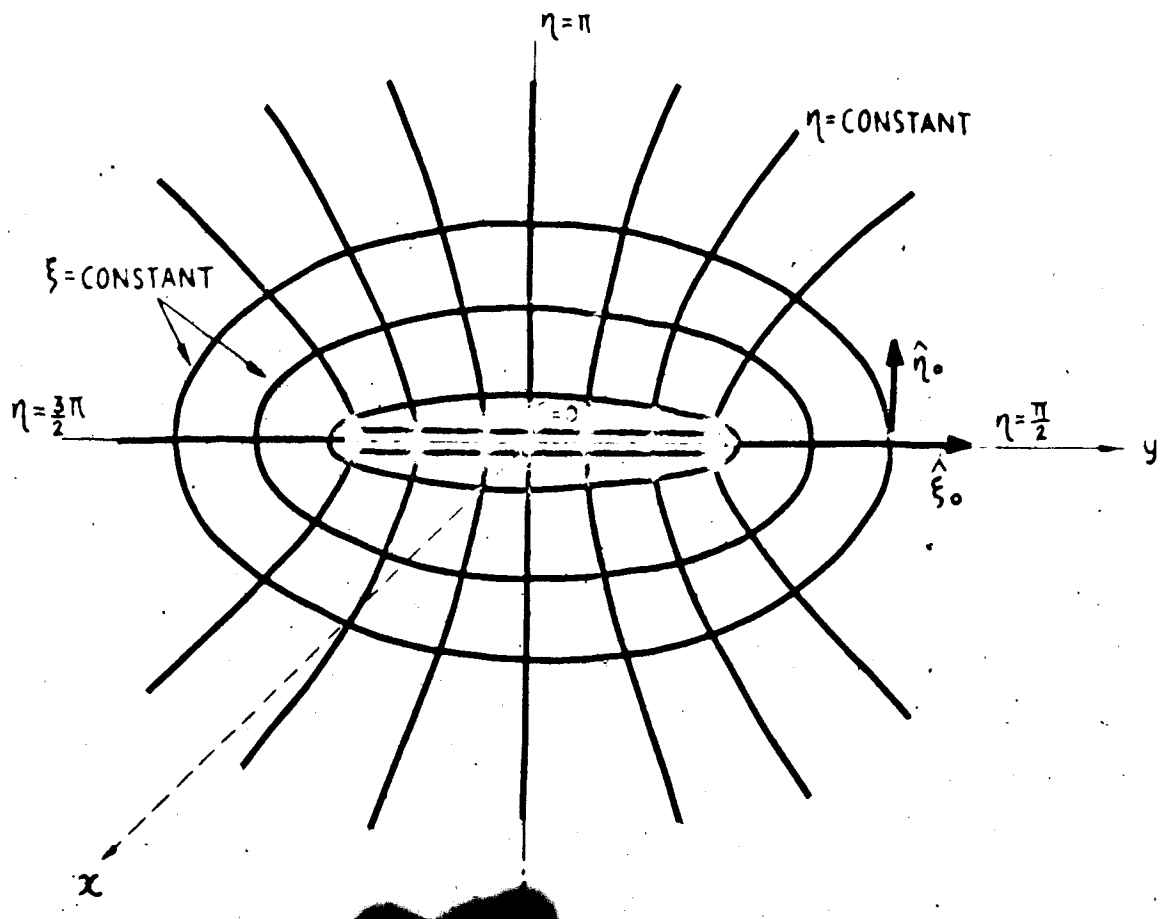


Fig. 2.1

Oblate Spheroid Co-ordinate System

$$\xi < \infty$$

$$\eta \leq 2\pi$$

$$y = a \cosh \xi \sin \eta$$

$$z = a \sinh \xi \cos \eta$$

Define the dimensionless stream function

$\Psi = \Psi^*/U^*a^2$: the dimensionless Froude number $Re = 2aU^*/V^*$; and set $E^2 = a^2R^*^2$ where 'a' is the semi-major axis, $a = c \cosh \xi_a$. ξ_a is the value of ξ at the surface. Equation (2.28) and Equation (2.29) become:

$$\operatorname{sech} \xi_a E^2 (E^2 \Psi) = \frac{Re}{2} \left[\frac{\cosh \xi \sin \eta}{\sinh^2 \xi + \cos^2 \eta} \right] .$$

$$\left[\frac{\partial \Psi}{\partial \xi} \frac{\partial}{\partial \eta} \left(\frac{E^2 \Psi}{\cosh \xi \sin^2 \eta} \right) - \frac{\partial \Psi}{\partial \eta} \frac{\partial}{\partial \xi} \left(\frac{E^2 \Psi}{\cosh^2 \xi \sin^2 \eta} \right) \right] , \quad (2.30)$$

$$E^2 = \frac{\cosh^2 \xi_a}{\sinh^2 \xi + \cos^2 \eta} \left[\frac{\partial^2}{\partial \xi^2} - \tanh \xi \frac{\partial}{\partial \xi} + \frac{\partial^2}{\partial \eta^2} - \cot \eta \frac{\partial}{\partial \eta} \right] .$$

$$(2.31)$$

Putting $E^2 \Psi = \zeta \cosh \xi \sin \eta \operatorname{sech} \xi_a$, where ζ is the non-dimensional vorticity and $\zeta = \zeta^* a / U^*$ and

$\zeta^* = h_3^{-1} E^* \Psi^*$. ξ_a is the value of ξ at the surface, then equation (2.30) can be split into two equations,

$$\operatorname{sech} \xi_a E^2 (\zeta \cosh \xi \sin \eta) = \frac{Re}{2} \left[\frac{\cosh \xi \sin \eta}{\sinh^2 \xi + \cos^2 \eta} \right] .$$

$$\left[\frac{\partial \Psi}{\partial \xi} \frac{\partial}{\partial \eta} \left(\frac{\zeta}{\cosh \xi \sin \eta} \right) - \frac{\partial \Psi}{\partial \eta} \frac{\partial}{\partial \xi} \left(\frac{\zeta}{\cosh \xi \sin \eta} \right) \right] , \quad (2.32)$$

$$\frac{1}{\sinh^2 \xi + \cos^2 \eta} \left[\frac{\partial^2 \Psi}{\partial \xi^2} - \tanh \xi \frac{\partial \Psi}{\partial \xi} + \frac{\partial^2 \Psi}{\partial \eta^2} - \cot \eta \frac{\partial \Psi}{\partial \eta} \right]$$

$$= \zeta \cosh \xi \sin \eta \operatorname{sech}^3 \xi_a . \quad (2.33)$$

Since ξ can become very large at the surface of the spheroid and hard to be handled numerically, it is more convenient to transform the equation (2.32) and equation (2.33) to

$$E^2 G = \frac{R e \cosh \xi_a}{2} \left[\frac{\cosh \xi \sin \eta}{\sinh^2 \xi + \cos^2 \eta} \right] \cdot \left[\frac{\partial \Psi}{\partial \xi} \frac{\partial F}{\partial \eta} - \frac{\partial \Psi}{\partial \eta} \frac{\partial F}{\partial \xi} \right] \quad (2.34)$$

and

$$\frac{1}{\sinh^2 \xi + \cos^2 \eta} \left[\frac{\partial^2 \Psi}{\partial \xi^2} - \tanh \xi \frac{\partial \Psi}{\partial \xi} + \frac{\partial^2 \Psi}{\partial \eta^2} - \cot \eta \frac{\partial \Psi}{\partial \eta} \right] \\ = G \operatorname{sech}^2 \xi_a, \quad (2.35)$$

by defining the non-dimensional quantities:

$$G = \xi \cosh \xi \sin \eta / \cosh \xi_a \quad (2.36)$$

$$F = \xi \cosh \xi_a / \cosh \xi \sin \eta \quad (2.37)$$

Using the finite differencing scheme:

$$\frac{\partial f_j}{\partial \xi} = \frac{f_{j+1} - f_{j-1}}{2A},$$

$$\frac{\partial f_i}{\partial \eta} = \frac{f_{i+1} - f_{i-1}}{2B},$$

$$\frac{\partial^2 f_j}{\partial \xi^2} = \frac{f_{j+1} - 2f_j + f_{j-1}}{A^2},$$

where ρ and β are the radial and angular spacing of a spherical grid, as shown in figure (C.3), equations (C.34) and (C.35) can be converted into finite difference form as given by Madigan (1973):

$$\begin{aligned}
 G(I, J) - \left(\frac{\partial}{\partial I} + \frac{\partial}{\partial J} \right) G(I, J+1) &= G(I, J+1) \left[\frac{2+\lambda \tanh \xi_{\alpha}(J)}{2\lambda} \right] \\
 &+ G(I, J-1) \left[\frac{2+\lambda \tanh \xi_{\alpha}(J)}{2\lambda} \right] + G(I+1, J) \\
 &\left[\frac{2+B \cot \eta(I)}{2B} \right] + G(I-1, J) \left[\frac{2+B \cot \eta(I)}{2B} \right] \\
 - \frac{Bc}{8} \operatorname{sech} \xi_{\alpha} \cos \xi_{\alpha}(J) \sin \eta(I) \\
 \left\{ \frac{[\Psi(I, J+1) - \Psi(I, J-1)]}{AB} [F(I+1, J) - F(I-1, J)] \right. \\
 \left. - \frac{[\Psi(I+1, J) - \Psi(I-1, J)]}{AB} [F(I, J+1) - F(I, J-1)] \right\}
 \end{aligned}$$

and

$$\begin{aligned}
 & \Psi(I, J) \left(\frac{2}{A^2} + \frac{2}{B^2} \right) = \Psi(I, J+1) \left[\frac{2 - A \tanh \xi(J)}{2A^2} \right] \\
 & + \Psi(I, J-1) \left[\frac{2 + A \tanh \xi(J)}{2A^2} \right] + \Psi(I+1, J) \left[\frac{2 - B \cot \eta(I)}{2B^2} \right] \\
 & + \Psi(I-1, J) \left[\frac{2 + B \cot \eta(I)}{2B^2} \right] - \operatorname{sech}^2 \xi_a \left[\sinh^2 \xi(J) \right. \\
 & \quad \left. + \cos^2 \eta(I) \right] G(I, J)
 \end{aligned} \tag{2.39}$$

Equations (2.38) and (2.39) can then be solved simultaneously with appropriate boundary conditions of the dimensionless stream function and non-dimensional vorticity by computer to obtain corresponding values of Ψ and ζ at each grid point.

2.5.2 * Spheres

The non-dimensional Navier-Stokes equation for steady-state axisymmetric flow in spherical co-ordinates (r, θ) can be expressed as:

$$\frac{Re}{2} \left[\frac{\partial \Psi}{\partial r} \frac{\partial}{\partial \theta} \left(-\frac{E^2 \Psi}{r^2 \sin^2 \theta} \right) - \frac{\partial \Psi}{\partial \theta} \frac{\partial}{\partial r} \left(-\frac{E^2 \Psi}{r^2 \sin^2 \theta} \right) \right] \sin \theta = E^2 E^2 \Psi \quad (2.40)$$

where

$$E^2 = \frac{\partial^2}{\partial r^2} + \frac{\sin \theta}{r^2} \frac{\partial}{\partial \theta} \left(\frac{1}{\sin \theta} \frac{\partial}{\partial \theta} \right). \quad (2.41)$$

$$\text{Putting: } E^2 \Psi = \zeta r \sin \theta, \quad (2.42)$$

where ζ as before is the dimensionless vorticity, then equation (2.40) can be reduced to:

$$\begin{aligned} \frac{Re}{2} \left[\frac{\partial \Psi}{\partial r} \frac{\partial}{\partial \theta} \left(\frac{\zeta}{r \sin \theta} \right) - \frac{\partial \Psi}{\partial \theta} \frac{\partial}{\partial r} \left(\frac{\zeta}{r \sin \theta} \right) \right] \sin \theta = \\ \frac{\partial^2}{\partial r^2} (\zeta r \sin \theta) + \frac{\sin \theta}{r^2} \frac{\partial}{\partial \theta} \left(\frac{1}{\sin \theta} \frac{\partial}{\partial \theta} \zeta r \sin \theta \right). \end{aligned} \quad (2.43)$$

and equation (2.42) becomes:

$$\frac{\partial^2 \Psi}{\partial r^2} + \frac{\sin \theta}{r^2} \frac{\partial}{\partial \theta} \left(\frac{1}{\sin \theta} \frac{\partial \Psi}{\partial \theta} \right) = \zeta r \sin \theta \quad (2.44)$$

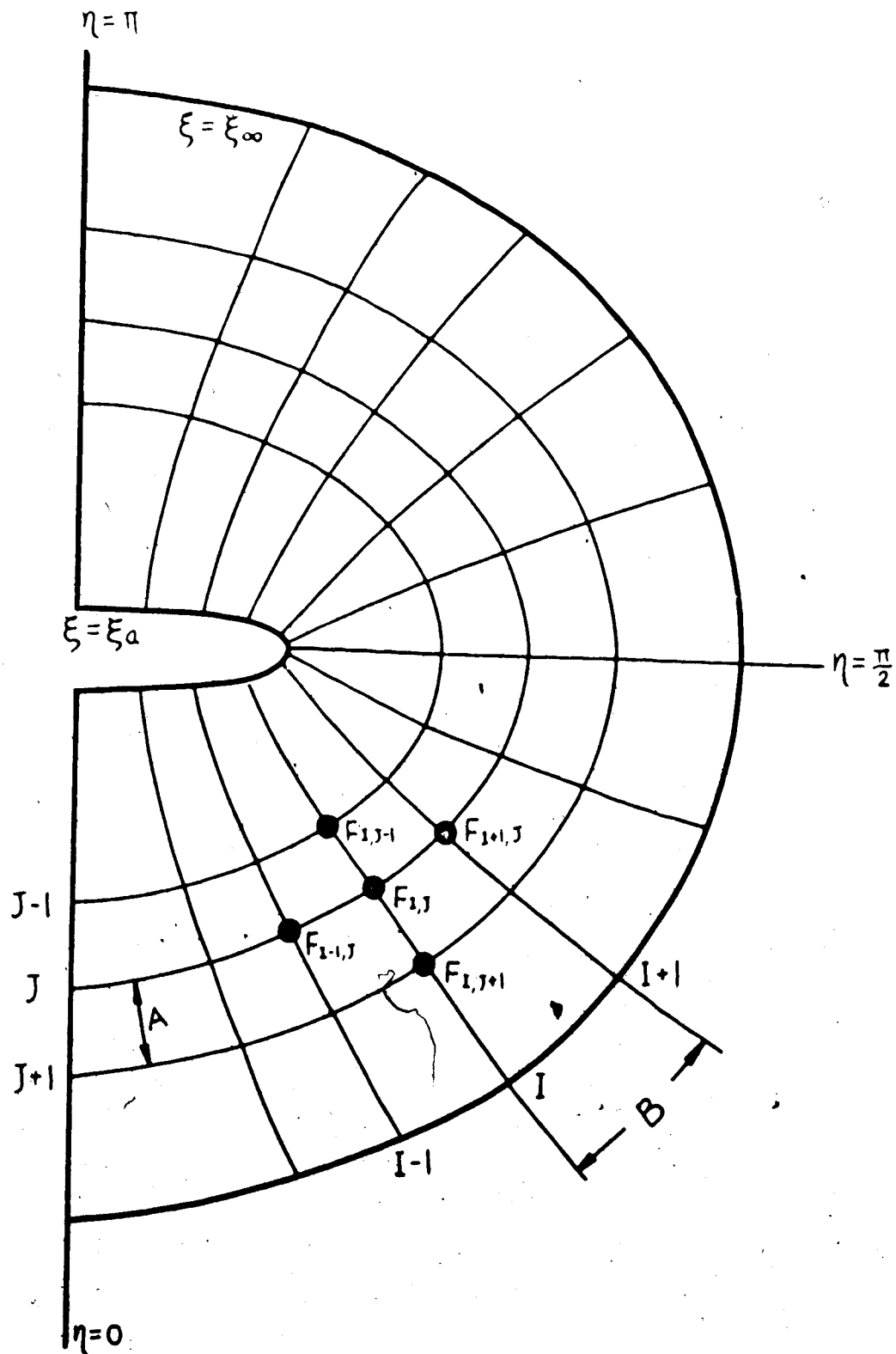


Fig. 2.2

Oblate Spheroidal Mesh System

for the sake of having exponential properties which would give a fine lattice near the surface, the radial co-ordinate r is transformed into $r = e^z$. The equation (2.43) and (2.44) are now given as,

$$\begin{aligned} -\frac{Re}{2} \left[\frac{\partial \Psi}{\partial Z} \frac{\partial}{\partial \theta} \left(\frac{\zeta}{e^z \sin \theta} \right) - \frac{\partial \Psi}{\partial \theta} \frac{\partial}{\partial Z} \left(\frac{\zeta}{e^z \sin \theta} \right) \right] e^z \sin \theta = \\ e^{2z} \left\{ \frac{\partial^2}{\partial Z^2} \left(\zeta e^z \sin \theta \right) + \frac{\sin \theta}{e^{2z}} \frac{\partial}{\partial \theta} \left(\frac{1}{\sin \theta} \frac{\partial \zeta}{\partial \theta} e^z \sin \theta \right) \right\}, \end{aligned} \quad (2.45)$$

and

$$-\frac{\partial^2 \Psi}{\partial Z^2} + \frac{\sin \theta}{e^{2z}} \frac{\partial}{\partial \theta} \left(\frac{1}{\sin \theta} \frac{\partial \Psi}{\partial \theta} \right) = e^{3z} \zeta \sin \theta. \quad (2.46)$$

As for the same reasons mentioned in the case of spheroid, the transformations:

$$F = \zeta / e^z \sin \theta \quad (2.47)$$

$$G = \zeta e^z \sin \theta \quad (2.48)$$

are taken. The Navier-Stokes equation in spherical co-ordinates is finally expressed as:

$$\begin{aligned} -\frac{Re}{2} \left[\frac{\partial \Psi}{\partial Z} \frac{\partial F}{\partial \theta} - \frac{\partial \Psi}{\partial \theta} \frac{\partial F}{\partial Z} \right] e^z \sin \theta - e^{2z} \frac{\partial^2 G}{\partial Z^2} \\ + \sin \theta \frac{\partial}{\partial \theta} \left(\frac{G}{\sin \theta} \right) = 0 \end{aligned} \quad (2.49)$$

and

$$\frac{\partial^2 \Psi}{\partial Z^2} + \frac{\sin \theta}{e^{2z}} \frac{\partial}{\partial \theta} \left(\frac{1}{\sin \theta} \frac{\partial \Psi}{\partial \theta} \right) = e^{2z} G. \quad (2.50)$$

Taking the finite differencing scheme as before with C and D

as the radial and angular spacing respectively of a spherical mesh shown in fig. (2.3), the equations (2.49) and (2.50), expressed in finite differencing form, can be written as:

$$\begin{aligned} & \Psi(I, J+1) \left(\frac{2-C}{2C^2} \right) + \Psi(I, J-1) \left(\frac{2+C}{2C^2} \right) + \Psi(I+1, J) \left(\frac{2-D \cot \theta(I)}{2D^2} \right) \\ & + \Psi(I-1, J) \left(\frac{2+D \cot \theta(I)}{2D^2} \right) - \Psi(I, J) \left(\frac{2}{C^2} + \frac{2}{D^2} \right) = G(I, J) e^{2Z(J)} \end{aligned} \quad (2.51)$$

and

$$\begin{aligned} & G(I, J+1) \left(\frac{2-C}{2C^2} \right) + G(I, J-1) \left(\frac{2+C}{2C^2} \right) + G(I, J+1) \left(\frac{2-D \cot \theta(I)}{2D^2} \right) \\ & - G(I-1, J) \left(\frac{2+D \cot \theta(I)}{2D^2} \right) - G(I, J) \left(\frac{2}{C^2} + \frac{2}{D^2} \right) - \frac{Re}{2} e^{2Z(J)} \sin \theta(I) \left[\left(\frac{\Psi(I, J+1) - \Psi(I, J-1)}{2C} \right) \right. \\ & \left. - \left(\frac{F(I+1, J) - F(I-1, J)}{2D} \right) - \left(\frac{\Psi(I+1, J) - \Psi(I-1, J)}{2D} \right) \left(\frac{F(I, J+1) - F(I, J-1)}{2C} \right) \right] = 0 \end{aligned} \quad (2.52)$$

The equations (2.51) and (2.52) can be solved simultaneously by computer for appropriate boundary conditions.

2.5.3 Formulation of Boundary Conditions for Spheroids.

The numerical analysis is confirmed between an inner surface represented by the spheroid itself and by an outer envelope which, like the spheroidal surface, coincides with one of the spheroidal co-ordinate grid lines.

As the two flow equations are of second order, four boundary conditions must be satisfied. The boundary

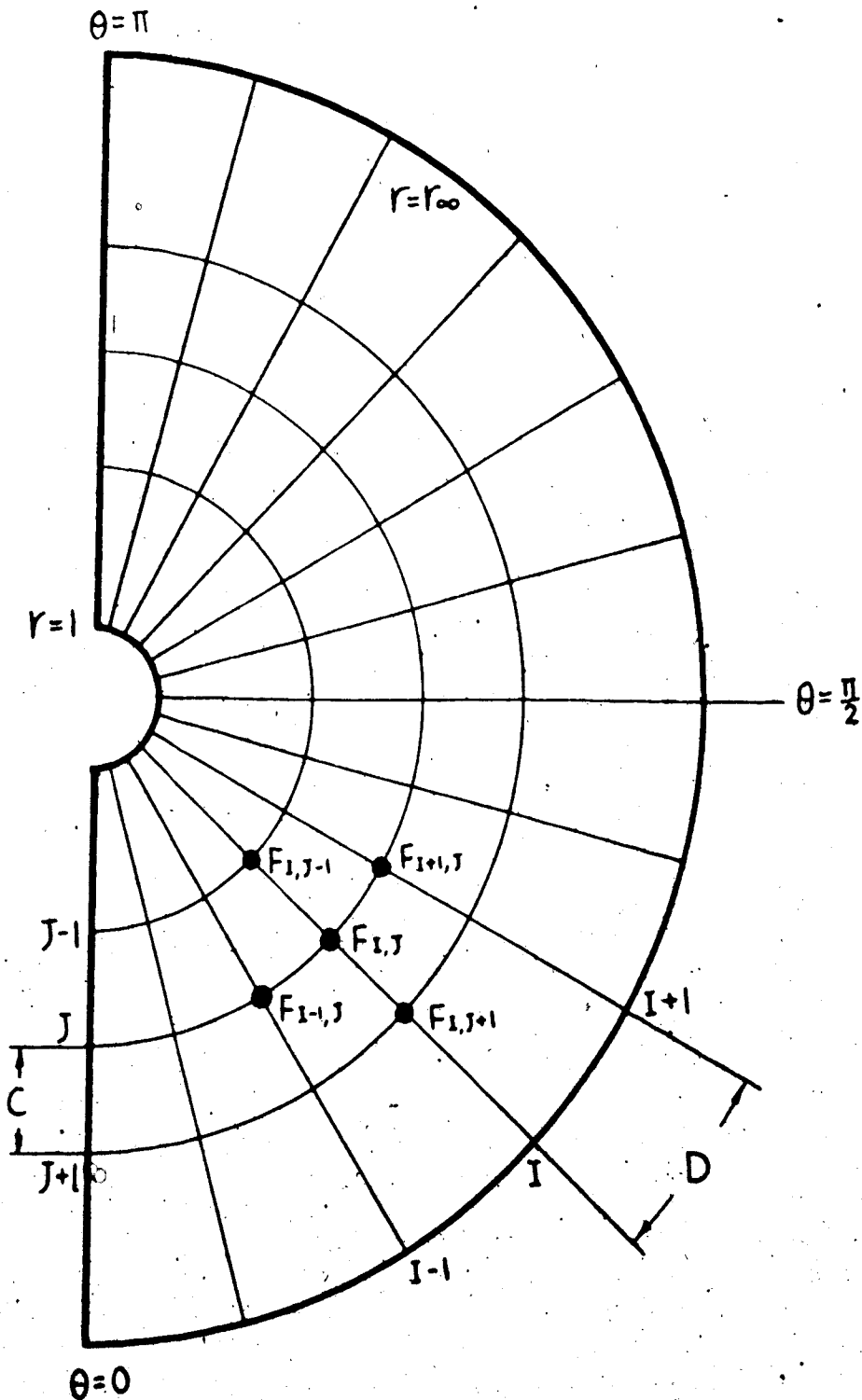


Fig. 2.3.
Spherical Mesh System

conditions for the stream function Ψ are:

$$\left. \begin{array}{l} \text{for } \eta = 0, \quad \Psi = 0 \\ \text{for } \eta = \pi, \quad \Psi = 0 \\ \text{for } \xi = \xi_a, \quad \Psi = 0 \end{array} \right\} \text{ defines the axis of symmetry,}$$

at the surface of the spheroid.

At the outer boundary, $\xi = \xi_\infty$ the flow is assumed to be a streaming parallel flow, giving $\Psi = \frac{1}{2} \sin^2 \eta \cosh^2 \xi_\infty \operatorname{sech}^2 \xi_a$. The boundary conditions for the vorticity ζ are:

$$\left. \begin{array}{l} \text{for } \eta = 0, \quad \zeta = 0 \\ \text{for } \eta = \pi, \quad \zeta = 0 \end{array} \right\} \text{ defines the axis of symmetry,}$$

$$\text{for } \xi = \xi_a, \quad \zeta = E^2 \Psi \cosh^2 \xi_a / \sin \eta - \text{at the surface of the spheroid,}$$

$$\text{for } \xi = \xi_\infty, \quad \zeta = 0 \quad - \text{in the undisturbed flow.}$$

The boundary condition for ζ at $\xi = \xi_a$, which originates from equation (2.35), can be explained as follows: At the surface, the no-slip conditions noted above require that

$$\Psi = \frac{\partial \Psi}{\partial \eta} = \frac{\partial \Psi}{\partial \xi} = \frac{\partial^2 \Psi}{\partial \eta^2} = 0 .$$

Equation (2.35) therefore reduces to

$$G(I, 1) = \frac{\cosh^2 \xi_a}{\sinh^2 \xi_a + \cos^2 \eta} \left| \frac{\partial^2 \Psi}{\partial \xi^2} \right|_{\xi=\xi_a}, \quad (2.53)$$

$J=1$ is the value of J at the surface of the spheroid.

Using the values of Ψ at $J=2$ and $J=3$ and expanding equation (2.53) as a Taylor's series to the third order, gives

$$G(I,1) = \frac{\cosh^2 \xi_a [8\Psi(1,2) - \Psi(1,3)]}{2A^2 [\sinh^2 \xi_a + \cos^2 \eta(1)]}, \quad (2.54)$$

which is equivalent to

$$\zeta(I,1) = \frac{\cosh^2 \xi_a [8\Psi(1,2) - \Psi(1,3)]}{2A^2 [\sinh^2 \xi_a + \cos^2 \eta(1)] \sin \eta(1)}. \quad (2.55)$$

2.5.4 Formulation of Boundary Conditions for Spheres.

The no-slip boundary conditions for a sphere are about the same as those for spheroid, namely for they are:

$$\text{for } \theta = 0, \quad \Psi = 0$$

$$\text{for } \theta = \pi, \quad \Psi = 0$$

$$r = 1, \quad \Psi = 0$$

Far from the sphere, there is undisturbed parallel flow:

$$r = r_\infty, \quad \Psi = \frac{1}{2} r_\infty^2 \sin^2 \theta.$$

The boundary conditions for ζ are:

$$\text{for } \theta = 0, \quad \zeta = 0$$

$$\theta = \pi, \quad \zeta = 0$$

$$r = 1, \quad \zeta = E^2 \Psi / \sin \theta$$

$$r = r, \quad \zeta = 0$$

The boundary conditions for ζ at $r=1$, can be as follows. At the surface, the no-slip conditions require:

$$\Psi = \frac{\partial \Psi}{\partial \theta} = \frac{\partial \Psi}{\partial r} = \frac{\partial^2 \Psi}{\partial \theta^2} = 0$$

Then equation (2.44) reduces to:

$$\frac{\partial^2 \Psi}{\partial r^2} = \zeta r \sin \theta \quad (2.56)$$

Expanding as a Taylor's series to the third term, equation (2.56) takes the following finite difference form:

$$\zeta(1,1) = \frac{8\Psi(1,2) - \Psi(1,3)}{2A^2 \sin \theta(1)} \quad (2.57)$$

CHAPTER III HYDRODYNAMIC INTERACTION OF AN ICE CRYSTAL AND A CLOUD PROLET

3.1 Introduction

The basic shape of ice crystals grown by diffusion is that of a hexagonal prism. Depending on the ambient temperature, growing ice crystals possess either prominent c-axis growth (hexagonal columns) or a-axis growth (thin hexagonal plates). In atmospheric clouds the warmest temperature at which glaciation begins is generally between -10° to -13°C giving ice crystals with predominantly plate type growth. That temperature range corresponds to growth mainly in the form of thin hexagonal plates with or without dendritic extensions. The dendritic (i.e. intricate) crystals are caused by fast growth due to high supersaturations. These facts have incited the study of the collision behaviour of plate-like ice crystals with water drops as a study of the riming behaviour of ice crystals. Pitter and Pruppacher (1974) computed the collision efficiencies of water spheres with oblate ice spheroids of axis ratio 0.05 and assumed that these collision efficiencies closely approximate those for thin hexagonal plates of ice. The hydrodynamic behaviour of an oblate spheroid was shown to be essentially the same as that of a circular disk of the same aspect ratio (Pitter et al, 1973).

Also, Jayaweera and Cottis (1969) and List and Schrenk (1971) have shown experimentally that the hydrodynamic behaviour of a simple hexagonal plate can be idealized with sufficient accuracy by that of a circular disk. For these reasons, ice oblate spheroids are used in this study to approximate the simple hexagonal ice plates in the numerical simulation of the initiation of graupel growth computations. The tendency of ice plates to accrete droplets at their corners as proposed by Knight and Knight (1973) is, of course, not covered by this type of approximation.

3.2 The Mathematical Model.

In order to model the hydrodynamic interactions between the ice crystals and cloud drops with as much physical realism and convenience as possible, the superposition scheme of Shafirir and Gal-Chan (1971) and Pitter and Pruppacher (1974) is used. The model neglects the close boundary effects, since it assumes that each body moves in the stream caused by the fluid motion around the other body in isolation. The equations governing this model are described later, but some physical aspects are described as follows. This approach gives only moderately accurate accounts of the hydrodynamic interaction of the two bodies, especially when the two bodies are very near

to each other or they have a very low relative velocity. However, the accelerative forces which occur during a hydrodynamic interaction of the falling bodies are small as compared to the product of the particle mass and the gravitational acceleration. Since total force associated with the flow field is approximately proportional to the mass of the body (Steinberger et al., 1970), a reasonable parameter for evaluating the effect of the flow field around the smaller body on the larger body is the mass ratio of the two bodies. The use of the superposition method described above would, therefore, be justified if the mass ratio of the small body over the larger one is small enough.

This argument also permits the neglecting of the possibility of the flow field around the drop causing the ice crystal to tilt. If angular acceleration is proportional to the torque and inversely proportional to the moment of inertia of the body, which in turn is proportional to the mass of the body, the torque on the spheroid is due to the effect of the flow field around the sphere which is proportional to the energy in the wake of the sphere, therefore, the ability of the water sphere to cause the ice spheroid to tilt is approximately proportional to the mass ratio of the bodies. If the mass ratio is always kept small, significant tilting of the ice spheroid is unlikely to occur. This has proved to be acceptable since the horizontal velocity of the ice spheroid calculated from the model is

apparently zero for all cases of study.

A thin oblate spheroid falling freely in air would have its broadest extension perpendicular to the flow so as to maximize its drag. In such a way, its axis of symmetry is parallel to the axis of the flow. For a body dropping vertically in air, it is subject to two forces: the gravitational and the drag force due to its motion. If the air is moving, the drag force on the body would be the one due to the relative motion of the body and air. The force on a body moving at \bar{V}^* and embedded in flow moving at \bar{U}^* could be approximated by $C_D \rho^* A |\bar{V}^* - \bar{U}^*|^2$ in the direction of $\bar{U}^* - \bar{V}^*$; where A is the projection area of the body perpendicular to the flow, and ρ^* is the density of the medium. As the oblate spheroid is assumed to be in steady state, the cross section area of the body normal to the flow is just a circle with radius of the semi-major axis of the spheroid, i.e. $A = \pi a_L^{*2}$. The dimensional drag force \bar{F}_d is then written as,

$$\bar{F}_d = \frac{1}{2} C_D \pi a_L^{*2} \rho^* |\bar{V}^* - \bar{U}^*|^2 \frac{(\bar{U}^* - \bar{V}^*)}{|\bar{U}^* - \bar{V}^*|}$$

$$\text{or } \bar{F}_d = \frac{1}{2} C_D \pi a_L^{*2} \rho^* |\bar{V}^* - \bar{U}^*| (\bar{V}^* - \bar{U}^*)$$

The Reynolds number Re_L is defined for the above body as

$$Re_L = \frac{2 a_L^* \rho^* |\bar{V}^* - \bar{U}^*|}{\mu}, \text{ so the drag force can be}$$

$$\text{rewritten as } \bar{F}_d = - \frac{\pi}{4} C_D Re_L \mu^* a_L^* (\bar{V}^* - \bar{U}^*). \text{ Thus, the}$$

trajectories of a large elliptical spheroidal ice crystal and a small spherical water drop can be described by the equations of motion as given by Chafrin and Gal-Chan (1971) and Litter and Pruppacher (1974):

$$m_L^* \frac{d\bar{V}_L^*}{dt^*} = m_L^* \bar{g}^* - \frac{\pi}{4} \mu^* C_D L R_{el,L} a_L^* (\bar{V}_L^* - \bar{U}_L^*) \quad (3.1)$$

and

$$m_s^* \frac{d\bar{V}_s^*}{dt^*} = m_s^* \bar{g}^* - \frac{\pi}{4} \mu^* C_D s R_{el,s} a_s^* (\bar{V}_s^* - \bar{U}_L^*) \quad (3.2)$$

The first terms of the right-hand side of the above equations are the gravitational forces and the second terms are the drag forces on the bodies due to their relative motion in air. 'm*'s denote the masses, 'v*'s' the velocities 'C_D's' the drag coefficients and 'a*'s' the semi-major axes normal to the flow. 'U*'s' denote the flow fields due to the motion of the other bodies and the subscripts 'L' and 's' represent the ice crystal and water drop, respectively. 'g*' and 'μ*' are the gravity acceleration and dynamic viscosity of air. The buoyancy of ice or water in air has been left out.

The quantities in equation (3.1) and (3.2) can be non-dimensionalized by the relations:

$$\begin{aligned}\bar{V} &= \bar{V}^*/V_{\infty}^* \\ \bar{U} &= \bar{U}^*/V_{\infty}^* \\ \bar{s} &= \bar{s}^* a_t^* / V_{\infty}^{*2} \\ t &= t^* V_{\infty}^* / a_t^* \\ \mu &= \mu^* a_t^{*2} / m_t^* V_{\infty}^*\end{aligned}$$

m_t^* , a_t^* and V_{∞}^* are the dimensional mass, the semi-major axis length of the spheroid and the terminal velocity of the ice crystal. \bar{V} , \bar{U} , \bar{s} and t are the dimensionless quantities corresponding to those with subscripts. During interaction of the ice spheroid and water sphere, the Reynolds numbers and the drag coefficients of the particles vary due to changes in their terminal velocity. The variation in the product ReC_D for the ice spheroid is negligible since change in its terminal velocity due to the flow field of the small water drop is negligible. For the small sphere, the drag coefficient times Reynolds number was found to change by a factor of about "two" as it approached the spheroid. Pitter's assumption that ReC_D is constant would be good for Stokes flow where C_D is inversely proportional to Re . However for the larger Re encountered here it appears to be inadequate. The effect is more predominant if the mass ratio of the small water drop to the large ice crystal is small. In the computation of the trajectories, the variation in drag coefficient and Reynolds number of the large i.e spheroid is not be taken into account but that of the small water

drag is included. The correction is, therefore, taken in every step of the computation of the particle trajectories as they approach the spheroid. For the large particle, the drag coefficient and Reynolds number are those for a body at its terminal velocity in an undisturbed medium and for the small particle, the drag coefficient and Reynolds number at the terminal velocity when falling in steady state are used to start the computation of trajectories and they are changed to correspond to the variation in velocity.

Applying the relations (3.3), equation (3.1) can be written in dimensionless form as,

$$\frac{d\bar{V}_L}{dt} = \bar{g} - \frac{\pi}{4} \mu C_{D_L} R_{e_L} (\bar{V}_L - \bar{U}_s) . \quad (3.4)$$

In the case of the ice spheroid falling at its terminal velocity in an undisturbed medium:

$$\frac{d\bar{V}_L}{dt} = 0 , \quad \bar{U}_s = 0 \quad \text{and} \quad \bar{V}_L = \bar{V}_{L\infty} = 1 ,$$

then equation (3.4) gives

$$\bar{g} = \frac{\pi}{4} \mu C_{D_L} R_{e_L} \quad (3.5)$$

For convenience, the parameter Q_L is equated to the scalar magnitude of the non-dimensional acceleration of gravity,

i.e.

$$U_L = \frac{\pi}{4} \mu C_D \rho_e R e_t , \quad (3.6)$$

which is dependent on variables which are constants for a given ice crystal and environment. Equation (3.2) is also non-dimensionalized with respect to the terminal velocity and semi-major axis of large ice crystal for convenience.

Since,

$$m_L = 4\pi a_L^3 A_r \rho_L / 3$$

$$\text{and } m_s = 4\pi a_s^3 \rho_s / 3 ,$$

where A_r is the aspect ratio, then the ratio of masses of the two particles is

$$\frac{m_s}{m_L} = \frac{a_s^3 \rho_s}{a_L^3 A_r \rho_L}$$

Defining the ratio $p = \frac{a_s}{a_L}$ and $q = \frac{\rho_s}{\rho_L}$, the mass ratio can be rewritten as,

$$\frac{m_s}{m_L} = \frac{p^3}{q A_r} .$$

Thus, equation (3.2) can be expressed in non-dimensional form as

$$\frac{d\bar{v}_s}{dt} = \bar{g} - \frac{\pi C_D s R e_s q A_r \mu}{4 p^2} (\bar{v}_s - \bar{U}_L) \quad (3.7)$$

For simplicity, the parameter μ is denoted as

$$Q_s = \frac{\pi C_{ds} R_{eq} A_{rm} \mu}{4 \rho^2} \quad (3.8)$$

where μ is a variable which depends on constants for a given ice crystal, water drop and atmosphere and varies with the velocity of the water drop.

3.3 Formulation of Computational Equations.

Velocity is the time derivative of position. In the case of either the oblate ice spheroid or the water drop, the relation

$$\frac{d\vec{R}}{dt} = \vec{V} \quad (3.9)$$

holds true. \vec{R} is the position vector. A system of eight first order differential equation can be specified for the water sphere and the thin oblate spheroid trajectories by resolving equations (3.9), (3.7) and (3.4) into their components with the simplification of equations (3.6) and (3.8). Namely, the equations in their component forms are:

$$\left. \begin{aligned}
 \frac{dR_{Lz}}{dt} &= V_{Lz} \\
 \frac{dV_{Lz}}{dt} &= Q_L [1 - (V_{Lz} - U_{Sz})] \\
 \frac{dR_{Ly}}{dt} &= V_{Ly} \\
 \frac{dV_{Ly}}{dt} &= -Q_L (V_{Ly} - U_{Sy}) \\
 \frac{dR_{Sz}}{dt} &= V_{Sz} \\
 \frac{dV_{Sz}}{dt} &= Q_L - Q_S (V_{Sz} - U_{Lz}) \\
 \frac{dR_{Sy}}{dt} &= V_{Sy} \\
 \frac{dV_{Sy}}{dt} &= -Q_S (V_{Sy} - U_{Ly})
 \end{aligned} \right\} \quad (3.10)$$

Subscripts Z and Y denote the vertical and horizontal components respectively. The first four equations of (3.10) are those for the vertical and horizontal time derivatives of position and velocity of the ice crystal and the last four equations govern those of the water drop.

The above equations are solved numerically using the Hamming predictor-corrector-modifier method. (James et al, 1967). The Hamming method for numerical solution of ordinary differential equations is of fourth order accuracy. The disadvantage of this method is that it requires four initial known step values for calculating the value of the next step. To overcome this, the Runge-Kutta method (Gerald, 1970) is used to start the integration.

The Runge-Kutta scheme is of fourth order accuracy also, but it requires longer computational times. The integration routine is given in the Appendix III. During the integration of the trajectories, it is assumed that each body experiences an external force due to the presence of the other body as though the flow field of the second body acts at the center of the first body. The flow fields are evaluated at the specific points at each step of the integration by using bi-quadratic interpolation in the appropriate co-ordinate systems. That is, by taking sixteen grid-point values (see figure 3.1) around the point in question. The value at that point is found using the expressions below. The Q's are interpolated with the four grid-point values P's along the lines passing them and the magnitude of X is then determined by the four values of Q's with the equations,

$$Q_N = P_{2,N} + (P_{3,N} - P_{2,N})\delta y \\ + (P_{1,N} + P_{4,N} - P_{3,N} - P_{2,N})(\delta y^2 - \delta y)/4$$

$$X = Q_2 + (Q_3 - Q_2)\delta x \\ + (Q_1 + Q_4 - Q_2 - Q_3)(\delta x^2 - \delta x)/4$$

The flow fields due to the motions of the ice crystal and water drop are calculated by using the finite difference scheme as discussed in Chapter 2 and the computer programs

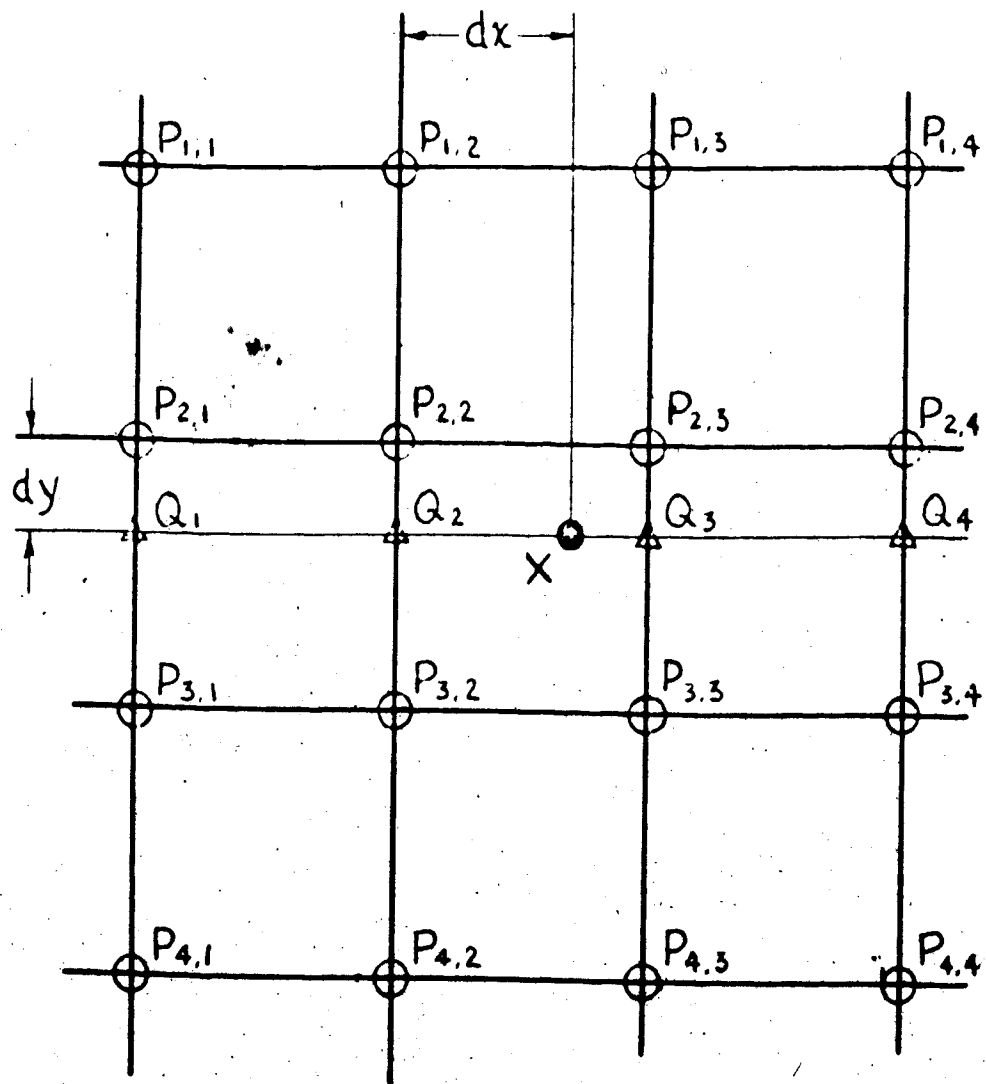


Fig. 3.1

Illustration of Grid-points for the Bi-quadratic Interpolation.

are given in Appendix I and Appendix II respectively.

Beyond the outer boundaries used to determine the flow fields, the fluid is assumed to be unperturbed by the presence of the moving body. Within the boundaries, the flow fields are assumed to remain the same as those caused by the fluid motion due to the movement of the body in isolation despite the presence of the other body — superposition, as discussed in section 3.1 of this chapter.

The vertical and horizontal separations between the centers of the oblate ice spheroid and the water sphere are determined by:

$$\left. \begin{array}{l} Z = R_{sz} - R_{lz} \\ Y = R_{sy} - R_{ly} \end{array} \right\} \quad (3.11)$$

and these values are assigned as the position for evaluating the flow fields acting on the other body by using the bi-quadratic interpolation method as mentioned above.

3.4 Evaluation of the Drag Coefficient, the Terminal Velocity and the Radius of Body Normal to the Flow

Le Clair et al (1970), after an extensive study of variation of drag coefficient with Reynolds number of spheres, suggest the drag coefficient for a sphere of Reynolds number less than 0.1 can be approximated by the

expression

$$C_D = \frac{C_D}{Re} \left(1 + \frac{3}{16} Re \right).$$

Ever since the study of fluid started, no simple relation of drag coefficient with size of an oblate spheroid moving in a medium has been established. For this reason, the drag coefficient of an oblate spheroid is calculated by the method discussed as follows:

The dimensionless local shear stress at the surface of a sphere $\tau_{re}|_{r=1}$ in terms of vorticity $\zeta_{r=1}$ and Reynolds number is given by Masilyah (1973) as

$$\tau_{re}|_{r=1} = 4 \zeta_{r=1} / Re \quad (3.12)$$

The surface of the sphere for $x=0$ is given by $Z^2 + Y^2 = 1$, where

$$\begin{aligned} Z &= r \cos\theta \\ Y &= r \sin\theta \end{aligned} \quad \left. \begin{array}{l} \\ \end{array} \right\} \quad r=1$$

The surface area of the circular strip in fig (3.2) on which the shear stress is considered to act is $2\pi y(dz^2 + dy^2)^{1/2}$. The drag force in the direction of the undisturbed flow acting on the whole surface due to the shear stress alone is then given by

$$F = 2\pi y(dz^2 + dy^2)^{1/2} \tau_{re}|_{r=1} \cos\alpha \quad (3.14)$$

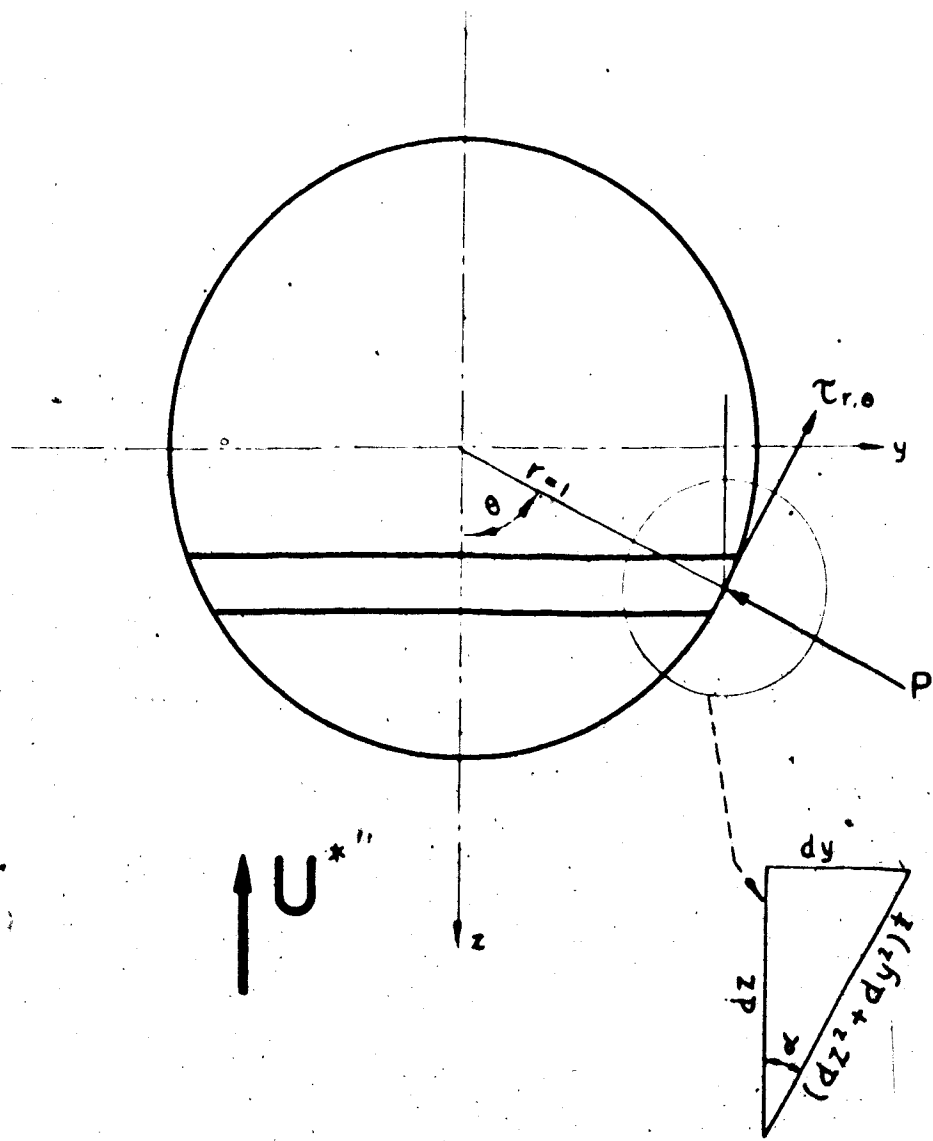


Fig. 3.2

Action of the normal and tangential
stresses on an element of area of a
sphere.

where α can be expressed as $\alpha = \frac{\pi}{2} - \theta$. The drag on a body is usually expressed in terms of a dimensionless drag coefficient,

$$C_D = \frac{\text{drag force in the flow direction}}{(\text{projection area normal to the direction of flow}) \times \text{kinetic pressure.}}$$

Therefore, the skin (friction) drag coefficient can be written from equation (3.14) as,

$$C_{DS} = \frac{\int_0^{\pi} 2\pi (dz^2 + dy^2) \sin \theta \tau_{rel|r=1}^* \cos \alpha}{\pi (\frac{1}{2} \rho^* U^*{}^2)} \quad (3.15)$$

Now $\cos \alpha = \frac{dy}{(dz^2 + dy^2)^{1/2}}$,

$$dz = \cos \theta d\theta \quad ,$$

$$dy = \sin \theta d\theta \quad ,$$

the dimension relation, $\tau = \tau^*/2 \rho^* U^*{}^2$, and making use of equation (3.12), equation (3.15) yields

$$C_{DS} = \frac{8}{Re} \int_0^{\pi} \sin^2 \theta \zeta_{r=1} d\theta \quad (3.16)$$

The above equation gives the skin drag coefficient for a sphere. For the case of an oblate spheroid, using the same

arguments, equation (2.16) can be transformed to

$$C_{DS} = \frac{8}{Re} \tanh \xi_a \int_0^\pi \sin^2 \eta \zeta_{\xi=\xi_a} d\eta. \quad (3.17)$$

The pressure distribution around a sphere is obtained by considering the radial and angular components of the Navier-Stokes equation. Taking the curl of the equation and applying the continuity equation, the equation (2.4) becomes:

$$\bar{v}^* \times \bar{\Omega}^* = \frac{1}{\rho} \nabla P^* + \frac{1}{2} \nabla V^*{}^2 + \nu \nabla \times \bar{\Omega}^*. \quad (3.18)$$

Now consider the angular component of equation (3.18) which is given by:

$$-h_1 V_r^* \zeta^* = \frac{h_2}{\rho} \frac{\partial P^*}{\partial \theta} + \frac{1}{2} h_2 \frac{\partial V^*{}^2}{\partial \theta} - \nu h_1 h_3 \frac{\partial}{\partial r} \left(\frac{\zeta^*}{h_3} \right). \quad (3.19)$$

At the surface, $V^*{}^2 = 0$, $V_r^* r = 0$ and for an oblate spheroid, $h_1 = h_2$, so that equation (3.19) becomes

$$\frac{\partial P^*}{\partial \theta} \Big|_{r=1} = \mu \left\{ \frac{\partial \zeta^*}{\partial r} \Big|_{r=1} + h_3 \zeta^* \frac{\partial}{\partial r} \left(\frac{1}{h_3} \right) \right\}. \quad (3.20)$$

Introducing the dimensionless pressure

$$= \frac{P^* - P^*_{\infty}}{\frac{1}{2} \rho U^*{}^2} \quad (3.20 a)$$

where P_{∞} is the dimensional frontal stagnation pressure, substituting for V_r and rendering all terms dimensionless, the equation (3.20) becomes:

$$\frac{Re}{4} \frac{\partial P}{\partial \theta} \Big|_{r=1} = \frac{\partial \xi}{\partial r} \Big|_{r=1} + \xi_{r=1} . \quad (3.21)$$

Integration of equation (3.21) along the surface gives

$$F - F_0 = \frac{1}{Re} \int_0^\theta \left[\frac{\partial \xi}{\partial r} \Big|_{r=1} + \xi_{r=1} \right] d\theta . \quad (3.22)$$

where F_0 is the dimensionless frontal stagnation pressure (at $\theta = 0$) and F is the dimensionless pressure at any one point on the surface of the sphere.

The dimensionless stagnation pressure F_0 is obtained by consideration of the radial component of equation (3.18). Using the axisymmetric properties, equation (3.18) yields for the radial direction as

$$h_2 V_\theta^* \xi^* = \frac{h_1}{P} \frac{\partial P^*}{\partial r} + \frac{1}{2} h_1 \frac{\partial V^*}{\partial r}^2 + V h_2^2 h_3 \frac{\partial}{\partial \theta} \left(\frac{\xi^*}{h_3} \right) . \quad (3.23)$$

Along the axis of the spheroid, $V^* \theta = 0$, hence equation (3.23) becomes:

$$\frac{-4}{Re} \left(\xi \cot \theta + \frac{\partial \xi}{\partial \theta} \right) \Big|_{\theta=0} = 2 V_r \frac{\partial V_r}{\partial r} + \frac{\partial P}{\partial r} , \quad (3.24)$$

where all quantities have been rendered dimensionless and the values of α_1 , β_1 and γ_1 for a sphere have been substituted. At the outer boundary $R = 0$ and $V=1$ and at the surface $R=r_0$ and $V=0$. On the axis of the sphere the integration of equation (3.24) from the surface to the outer boundary, therefore, becomes:

$$\Gamma_0 = 1 + \frac{4}{\pi r_0} \int_1^{r_0} \left(\zeta \cot \theta + \frac{\partial \zeta}{\partial \theta} \right) \Big|_{\theta=0} dr . \quad (3.25)$$

Along the axis $\theta=0$, $\cot \theta = \infty$ and $\zeta=0$, using l'Hospital's rule, equation (3.25) becomes:

$$\Gamma_0 = 1 + \frac{8}{\pi r_0} \int_1^{\infty} \frac{\partial \zeta}{\partial \theta} \Big|_{\theta=0} dr . \quad (3.26)$$

From figure (3.1), the form (pressure) drag coefficient is given by:

$$C_{DF} = \frac{\int_0^\pi 2\pi (dz^2 + dy^2)^{\frac{1}{2}} \sin \alpha P}{\pi} \quad (3.27)$$

where $\sin \alpha = dz/(dz^2 + dy^2)^{\frac{1}{2}}$ and at the surface, $z = \cos \theta$ and $dz = -\sin \theta d\theta$, rendering equation (3.27),

$$C_{DF} = \int_0^\pi P \sin 2\theta d\theta \quad (3.28)$$

Equations (3.22), (3.26) and (3.28) can be transformed for the case of an oblate spheroid as given by Pitter et al (1973)

$$1 - \frac{1}{\rho_a} = \frac{1}{\rho_a} \int_0^{\eta} \left[\frac{\partial \zeta}{\partial \xi} \Big|_{\xi=\xi_a} + \zeta_{\xi=\xi_a} \tanh \xi_a \right] d\eta, \quad (3.29)$$

$$1 - \frac{1}{\rho_a} = 1 + \frac{g}{\rho_a e} \int_{\xi_a}^{\xi_\infty} \frac{\partial \zeta}{\partial \eta} \Big|_{\eta=0} d\xi, \quad (3.30)$$

and

$$C_D = \int_0^{\pi} P \sin 2\eta d\eta. \quad (3.31)$$

the total drag coefficient is obtained by adding the skin and form drag coefficients, i.e. $C_D = C_{Df} + C_{Dw}$.

For a spherical body falling in steady state in air, the gravitational force acting on the body should be neutralized by the drag force caused by the motion.

Using the definition of Re and m_s this concept can be written as

$$\frac{\pi}{4} C_D Re a_s V_{\infty s} u = m_s g \frac{(P_s - P_a)}{P_s} \quad (3.32)$$

and can be rewritten as

$$C_D Re^2 = 32 g a_s^2 (P_s - P_a) \rho_a / \mu^2. \quad (3.33)$$

For known Reynolds number and drag coefficient solving for

The relation of the radius, a_s , and

$$a_s = (3 \mu^2 C_d R_e^2 / 32 g (\rho_s - \rho_a) \rho_a)^{1/3} . \quad (3.34)$$

The terminal velocity can then be found using the relation of Reynolds number to radius and terminal velocity of a sphere.

For an oblate spheroid, following the same arguments with the mass, $m_s = \frac{4}{3} \pi a_s^3 A r \rho_s$, thus

$$C_d R_e^2 = 32 g a_s^3 A r (\rho_s - \rho_a) \rho_a / u^2 \quad (3.35)$$

or

$$a_s = (3 \mu^2 C_d R_e^2 / 32 g (\rho_s - \rho_a) \rho_a A r)^{1/3} . \quad (3.35a)$$

The drag coefficients for the spheroid and the sphere in equations (3.15), (3.28), (3.17) are integrated using finite difference method with the vorticities calculated from the flow field routine. They are then used for solving the radii of the bodies normal to the flows and the terminal velocities of the bodies which are to be applied to initiate the computation of the trajectories.

CHAPTER IV NUMERICAL METHODS AND ALGORITHMS

4.1 Numerical procedures

The flow field of the ice crystal is evaluated with the finite difference method discussed in section (2.5.1) of Chapter 2. The grid points used are in oblate spheroidal co-ordinates with radial step size $\Delta\xi = A = 0.1$ and angular step size $\Delta\eta = \pi = 6$. Boundary conditions shown in section (2.5.3) are used. Outer boundaries are located at 50 crystal semi-major axis lengths. Approximate grid-point values are evaluated from the analytical solutions of the Stokes flow around a sphere (equation 2.14). A relaxation technique is then employed to achieve more accurate grid values. The solutions are considered to have converged when successive values at all grid points for both the dimensionless stream function and the non-dimensional vorticity fields have fractional changes of less than 0.001. An over-relaxation method is used for equation (2.39) while an under-relaxation is applied to equation (2.38), as the former equation is mathematically linear and the second is not.

Two methods are used to calculate the flow field of the water drop. For droplets of Reynolds number greater than or equal to 0.1, the finite difference method of solving the complete Navier-Stokes equation numerically

and discussed in section 2.6.1. It is used at grid-points in modified spherical co-ordinates with radial step size $C = 0.05$ and angular step size $\theta = 3^\circ$. Boundary conditions shown in section (2.5.4) are used with outer boundaries located at 80 drop radii. Approximate initial grid-values are taken from analytic solution of creeping flow past a spherical obstacle (equation 2.14). Relaxation techniques and convergence criteria are followed the same as that for the spheroid. For drops of Reynolds number smaller than 0.1, the flow fields are computed using a procedure suggested by Le Clair et al (1970). This involves the Stokes solution for a bounded fluid.

The flow fields evaluated from the above discussions are in terms of dimensionless stream functions and vorticities. These values have to be converted into non-dimensional velocities. In two-dimensional curvilinear co-ordinates, the dimensional velocities can be related to the dimensional stream function by the expressions:

$$\left. \begin{aligned} v_{q_1}^* &= \frac{-1}{h_2 h_3} \frac{\partial \Psi^*}{\partial q_2} \\ v_{q_2}^* &= \frac{1}{h_1 h_3} \frac{\partial \Psi^*}{\partial q_1} \end{aligned} \right\} \quad (4.1)$$

and

h_1, h_2, h_3 are defined as the same in Chapter 2. Therefore, in spheroidal co-ordinates, the non-dimensional velocities

can be expressed as:

$$v_\xi = \frac{-\cosh^2 \xi_a}{(\sinh^2 \xi + \cos^2 \eta) \cosh \xi \sin \eta} \left. \frac{\partial \Psi}{\partial \eta} \right\} \quad (4.2)$$

and

$$v_\eta = \frac{\cosh^2 \xi_a}{(\sinh^2 \xi + \cos^2 \eta) \cosh \xi \sin \eta} \left. \frac{\partial \Psi}{\partial \xi} \right\},$$

and in the modified spherical co-ordinates with $r=c^z$, the dimensionless velocities are

$$v_r = \frac{-e^{-2z}}{\sin \theta} \left. \frac{\partial \Psi}{\partial \theta} \right\} \quad (4.3)$$

and

$$v_\theta = \frac{e^{-2z}}{\sin \theta} \left. \frac{\partial \Psi}{\partial z} \right\}$$

In order to save computing time, the symmetry condition around the α -axis is used, thus implying that

$$v_\eta \Big|_{\eta=0,\pi} = \frac{\partial v_\xi}{\partial \eta} \Big|_{\eta=0,\pi} = \Psi \Big|_{\eta=0,\pi} = \xi \Big|_{\eta=0,\pi} = 0 \quad (4.4)$$

and

$$v \Big|_{z=0,\pi} = \frac{\partial v_\theta}{\partial \theta} \Big|_{\theta=0,\pi} = \Psi \Big|_{\theta=0,\pi} = \xi \Big|_{\theta=0,\pi} = 0. \quad (4.5)$$

Using l'Hospital's rule and equations (4.2) and (4.3), we have:

$$v_\eta \Big|_{\eta=0,\pi} = 0 \quad (4.6)$$

$$v_\xi \Big|_{\eta=0,\pi} = -\frac{\cosh^2 \xi_a}{\cosh^2 \xi} \left. \frac{\partial^2 \Psi}{\partial \eta^2} \right.$$

and

$$\begin{aligned} V_\theta |_{\theta=0,\pi} &= 0 \\ V_r |_{\theta=0,\pi} &= e^{-2z} \frac{\partial^2 \Psi}{\partial \theta^2} \end{aligned} \quad (4.7)$$

The flow fields calculated from the previous arguments are for stationary obstacles in a moving stream. For a body moving in a calm fluid the velocities would be relative to those calculated above. Thus, the velocities would be the differences between the terminal velocity of the body and those calculated from the case of a stationary obstacle in a moving medium.

The corrected flow fields are then applied into the trajectory calculations. In the trajectories computation routine, the ice spheroid and the water drop are initially vertically separated by three semi-major axes of the crystal. This separation is believed to be enough since the change in the velocity of the flow due to the spheroid's approach is practically negligible at a distance of three semi-major axis upstream. The horizontal separation of the fall paths of the two particles is varied for each calculation. Therefore, the initial horizontal and vertical acceleration of the ice crystal and the water drop are

taken to be zero and the vertical velocities are their terminal velocities non-dimensionalized by the terminal velocity of the ice crystal. Initially, the flow field caused by one body at the location of the other body is taken to be zero. The bodies are initially falling vertically at their terminal velocities. That is, the horizontal velocities are taken to be zero at the beginning of the integration.

The non-dimensional time difference used between every step in the integration of the trajectories is 0.01. For an ice crystal of semi-major axis of 400 microns and falling at a speed of 45 cm sec^{-1} , the actual time step would be less than 0.1 msec. This amount of time has proved to be small enough to avoid errors due to the numerical integration.

The hydrodynamic interaction process is assumed to be taking place in an atmosphere of temperature -10°C and of pressure 700 mb. The density of air is therefore $9.267 \times 10^{-4} \text{ gm cm}^{-3}$ and the dynamic viscosity of air is 1.667×10^{-4} poise. The density of ice is taken as 0.92 gm cm^{-3} and the density of water is 1 gm cm^{-3} . After proper non-dimensionalization, these values are used with appropriate Reynolds number, radii of particles, drag coefficients and terminal velocities to obtain the parameters for the computation routine.

4.2 Assumptions of The Numerical Simulation of the Initiation of Graupel Growth.

There is no perfect modeling that can fully illustrate the happenings in a graupel growing cloud. In every cloud model or graupel or hail growth model, there must be some limitations and assumptions involved. There is no exception in this model. As it is impossible to include a random sample of size distribution of cloud droplets and ice crystals in the model, the model is restricted to a particular ice crystal and it assumes that drops of the same radius are distributed everywhere in the region under consideration. This assumption implies that no collision between drops occurs. If collision between drops exists, then the size of drops can no longer be the designed one. Moreover, that water drop must retain its spherical shape during the whole process of calculation, along its trajectory and after collision with the ice crystal. In another words, the water drop must be spherical all the time and it must freeze completely without any distortion in shape when it touches the surface of a crystal. The drop will remain at the point of impact. This is not likely to happen exactly in the atmosphere, because according to Maruyama (1968) the frozen cloud droplets are found to have accreted together with one another so tightly that no vacant gaps are seen at the points of

adherence in the interior structure. This suggests that water drops do not freeze completely right after the impact, but some of the water remains at its surface until another cloud droplets accrete on them. Besides, results of density measurements suggest that cloud droplet accretion is nearly uniform during the growth from a small graupel to a large one. According to Mason (1960), the density of a graupel is around 0.6 gm cm^{-3} or less. This density is much smaller than that of pure ice. This implies that air bubbles should be trapped inside a graupel.

As particular interest is on critical collision parameters, only these are calculated. That is, the range of discrepancy between the lines of motion of the crystal (oblate spheroid) and the sphere which results in a collision is evaluated. The outer (or inner) most critical point of impact is defined as that critical offset on the ice crystal that away from (or inside of) which collision never occurred and inside of (or away from) which collision always occurred for particular size of cloud droplets. After a critical point of impact, either inner or outer, has been calculated, the critical point on which a second drop would just touch the first drop is evaluated. It is assumed that the flow field around the ice crystal does not change even when there is a water drop frozen on its surface. This is the most agreeable assumption. If this change in flow field were taken into account, the new

flow field would have to be calculated again from the complete Navier-Stokes equation. Then the inner boundaries would no longer be the shape of a simple oblate spheroid. It becomes a combination of an oblate spheroid and a small sphere. The oblate spheroidal co-ordinate system would no longer provide the convenience it gave before. No simple co-ordinate system is suitable for an obstacle of this shape. Moreover, the computer time used to generate a flow field around a symmetric obstacle, by solving the Navier-Stokes equation numerically using the finite difference method, is very long already. It would take even much longer to obtain the flow field around an irregular particle. To grow a whole graupel is not the object of this study. The object of this model is to determine the maximum angle that accreted water drops would form with the ice crystal. Two or three drops adhered at the outer most or inner most side of the ice crystal would be good enough to illustrate the solution. If a few small drops are attached to the surface of an ice crystal, the flow field around it would not be changed a very great deal from that of a clean and smooth one of the same size. For all these reasons, the flow field around the water drop adhered ice crystal is taken from that of an ice oblate spheroid of the same Reynolds number and aspect ratio.

It has been mentioned in the Chapter 3 that the drag coefficient and Reynolds number of the ice crystal

The assumed to be constant throughout the integration of the trajectories of the two particles though there is a very small deceleration of order of 10^{-7} are reported from the model. In addition to all the assumptions discussed above, the buoyancy effect of ice and water in air are neglected in the calculations.

CHAPTER V - NUMERICAL RESULTS AND DISCUSSION

5.1 The Flow Fields around an Oblate Spheroid (Ice Crystal).

In most continental clouds, the drops are too small to grow by collision and coalescence with other drops. In such clouds, when portions of cloud become cooled enough, ice crystals are nucleated. The ice crystals formed usually grow in two stages: initially by diffusion of water vapour, and subsequently by riming. Ono (1969) and Wilkins and Auer (1970) showed that, after nucleation, thin hexagonal ice plates must grow by vapour diffusion to at least 200 microns in radius before riming may commence. For this reason and due to the limitation of time and computing funds, two sizes of ice oblate spheroids are studied, namely with Reynolds number 10 and 20, which correspond to radii of 289.2 and 396.3 microns. The drag coefficients obtained from the converged numerical solution of the Navier-Stokes equation of motion for viscous flow past an oblate spheroid of axis ratio 0.05 of Reynolds number 10 and 20 are 2.81 and 3.92. The stream function and vorticity fields near the spheroid are plotted for Reynolds number 20 in figures 5.1.1 and 5.1.2, and for Reynolds number 10 in figures 5.1.3 and 5.1.4. The computed values of the vorticity at the surface of the body of Reynolds number 20

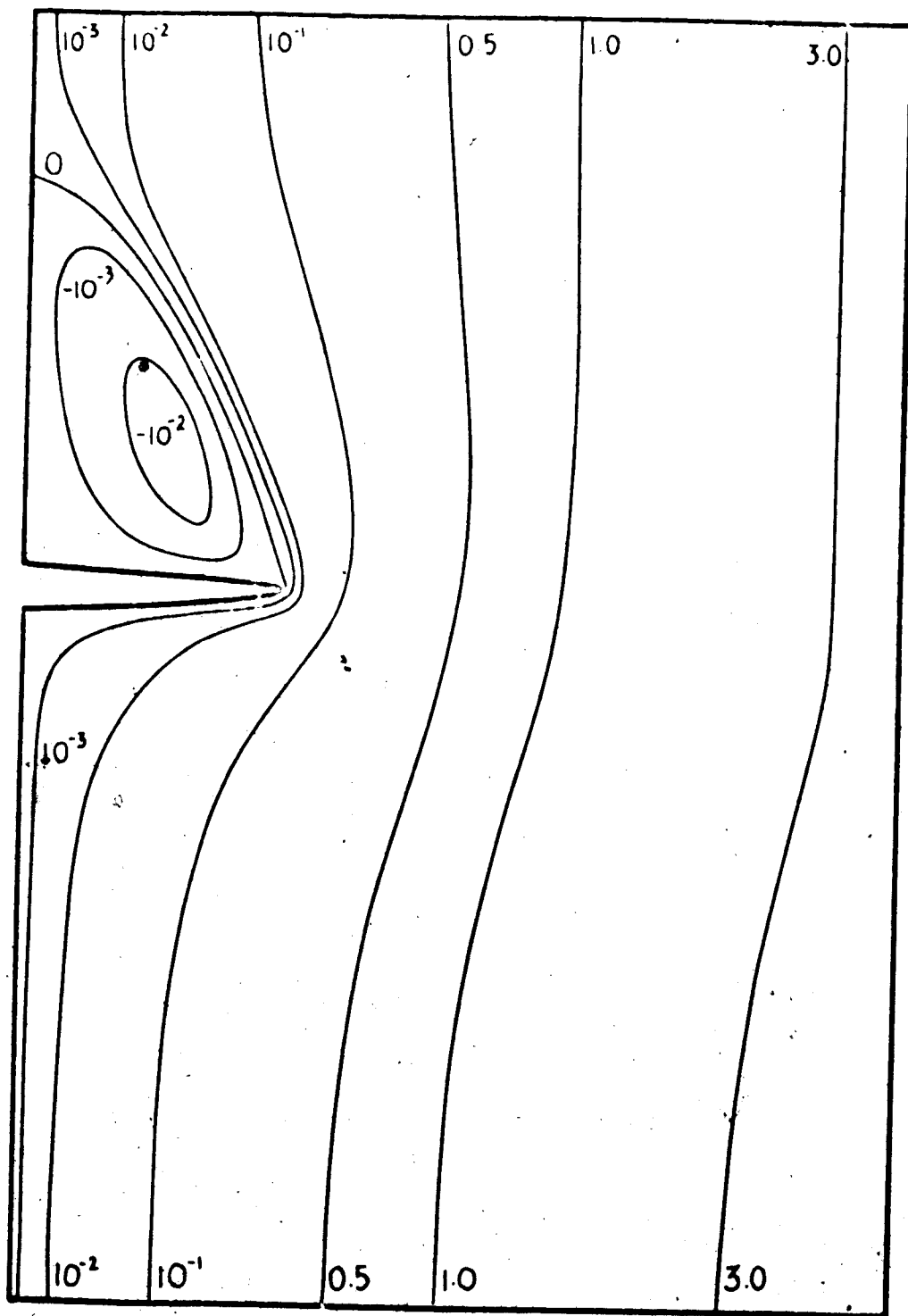


Fig. 5.1.1

Dimensionless Stream function of an Oblate Spheroid
of $Re = 20$ and $Ar = 0.05$

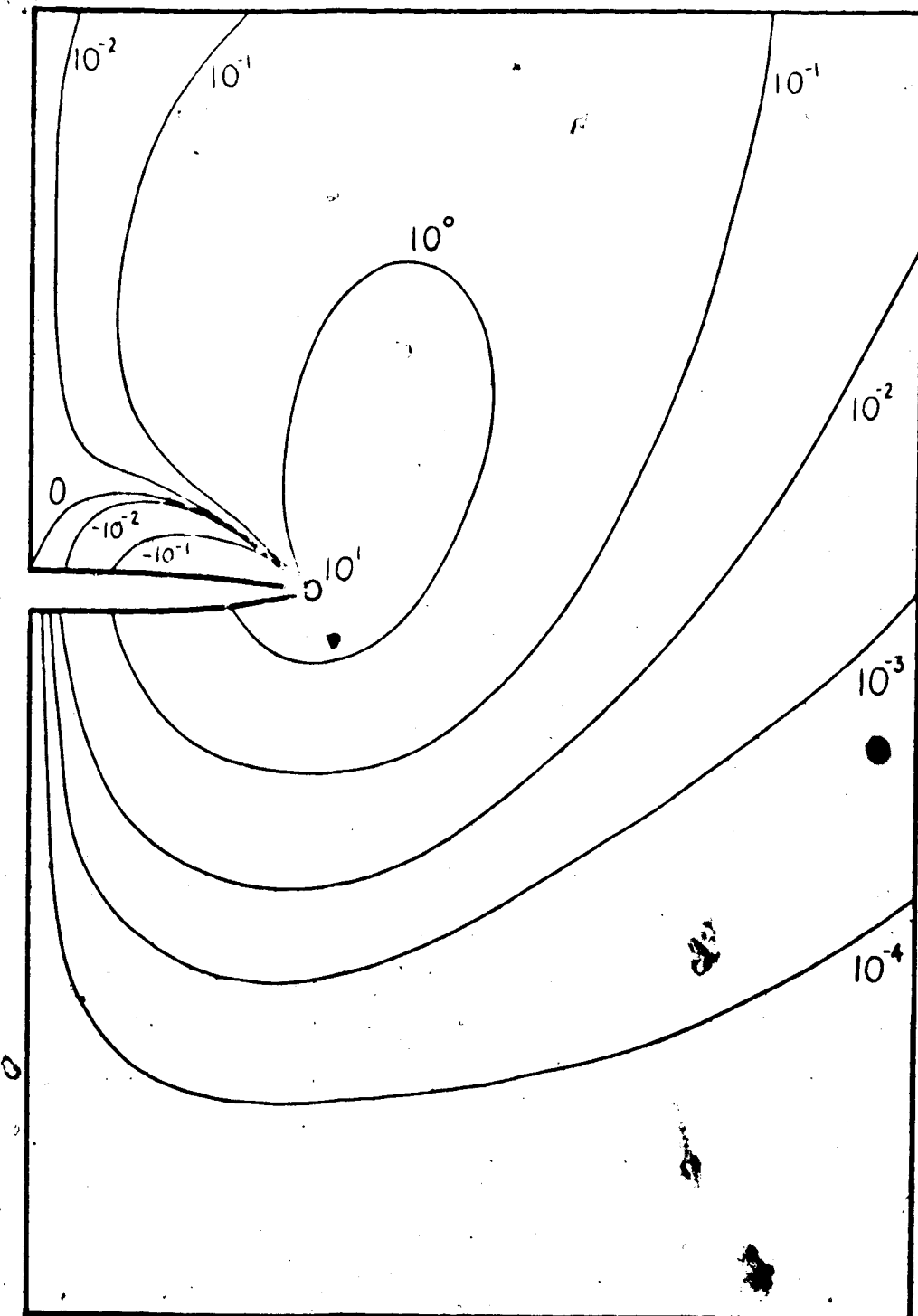


Fig. 5.1.2

Dimensionless Vorticity Field Around An Oblate Spheroid of $Ar = 0.05$, $Re = 20$

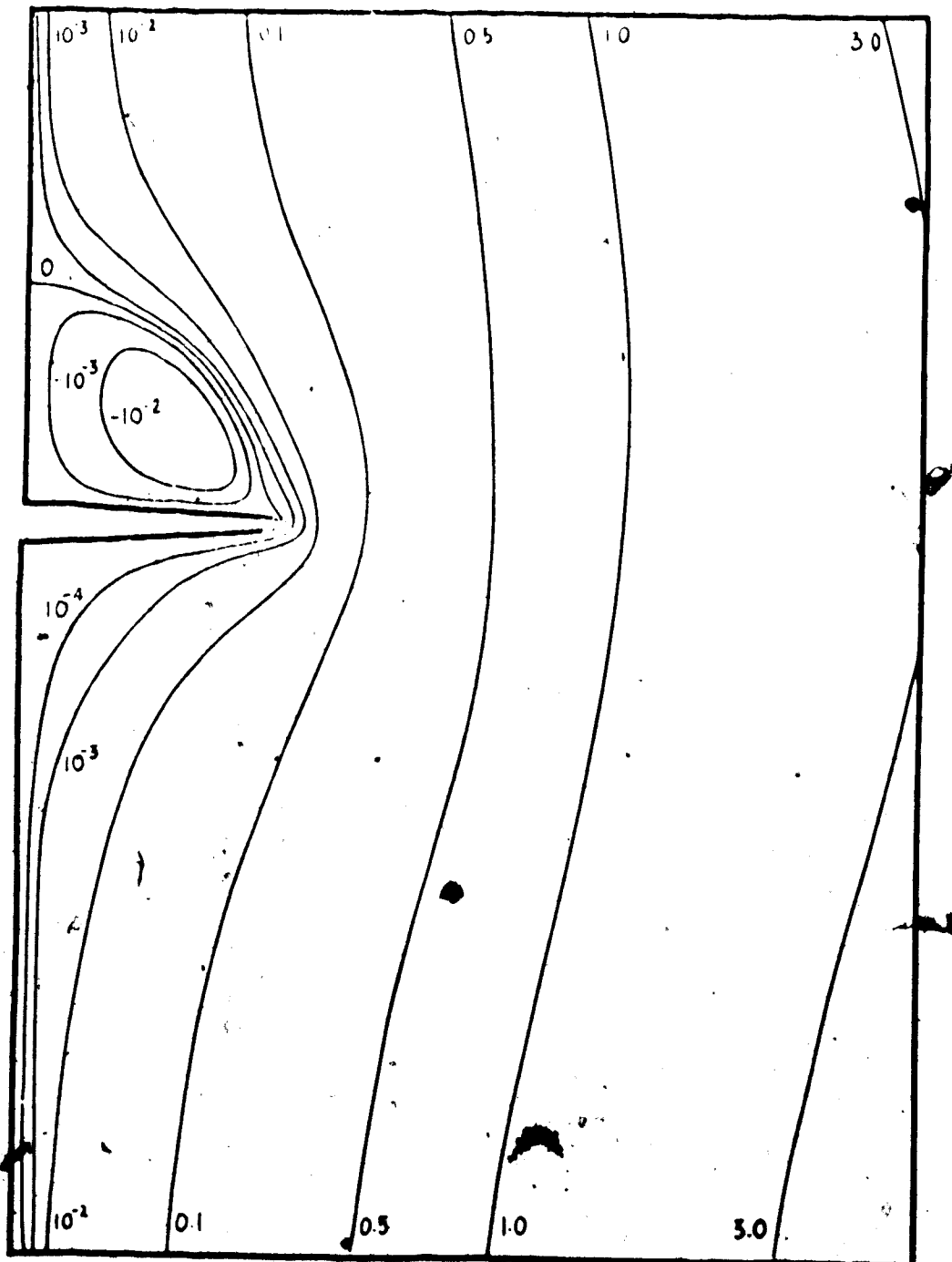


Fig. 5.1.3

Dimensionless Stream Function Field Around An
Oblate Spheroid of $\text{Ar} = 0.05$ $\text{Re} = 10$

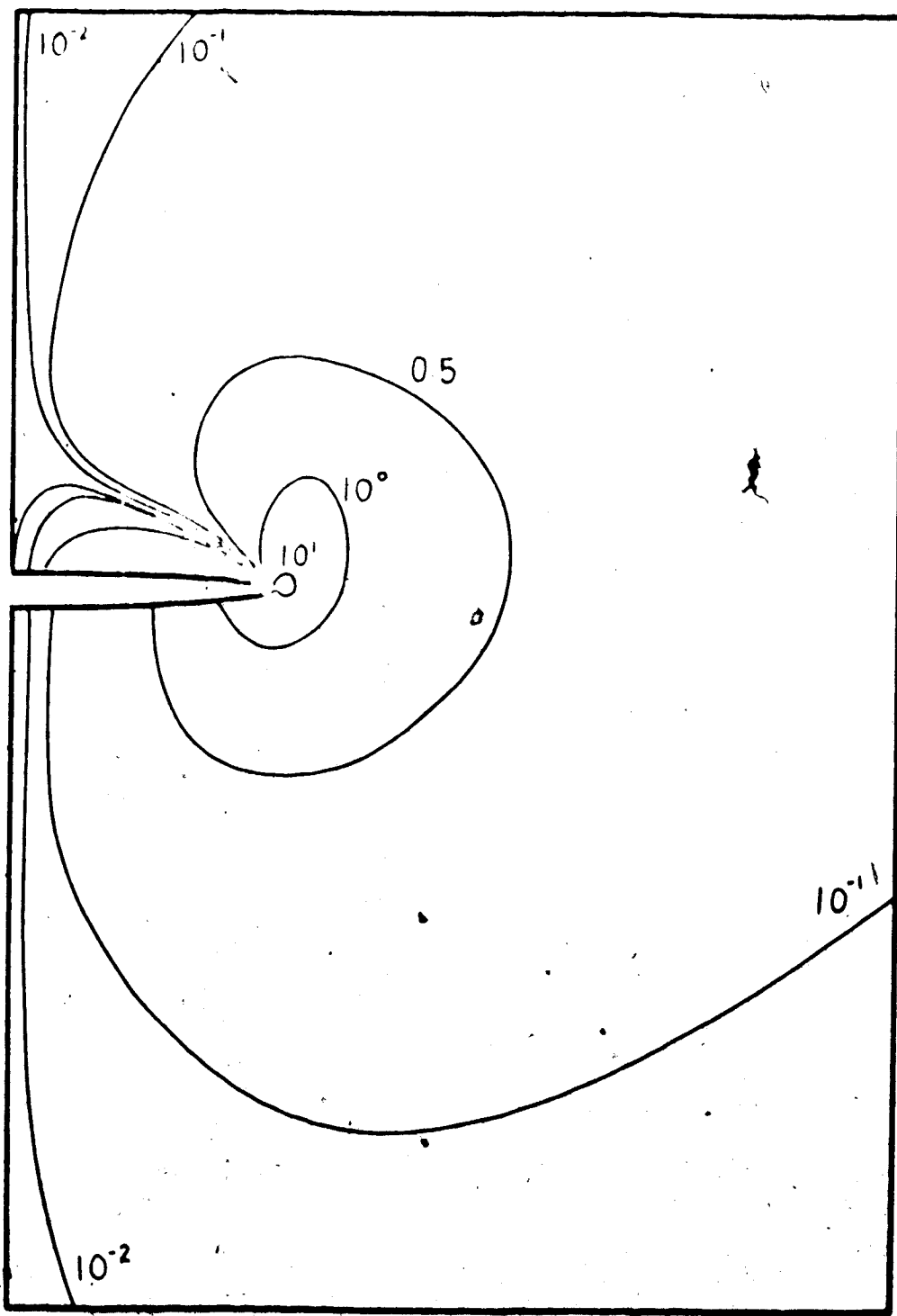


Fig. 5.1.4

Dimensionless Vorticity of Oblate Spheroid of

• $Re = 10$, $Ar = 0.05$

and 10 together with those from Fitter et al (1973) for $Ar = 0.05$ and those from McHugh and Epstein for $Ar = 0.05$ are shown in figure 5.1.5. After converting from the stream functions, the vertical and horizontal velocity fields of air passing the oblate spheroid of Reynolds number 10 relative to free air due to the motion of the particle are plotted in figures 5.1.6 and 5.1.7. The vorticity on the surface of the oblate spheroids seem to agree pretty well with those of Fitter et al and the dimensionless stream functions at the windward side of the oblate spheroid of $Re = 20$ is almost the same as those from their result. However, there are some small deviations in the stream function field at the downstream side of the oblate spheroid. This deviation is most probably due to the difference in the converging criteria and the computation routine. Anyway, a very well developed eddy at the downstream end of the oblate spheroid both for $Re = 20$ and $Re = 10$ can be seen. The eddy length — the ratio of the length of the wake to the major axis of the oblate spheroid — of the present results are plotted in figure 5.1.8 in conjunction with the curve given by Fitter et al for oblate spheroids of $Ar = 0.05$ and various Reynolds numbers. It is clear from the diagram that the eddy length of the present results agree quite well with those obtained by the previous workers.

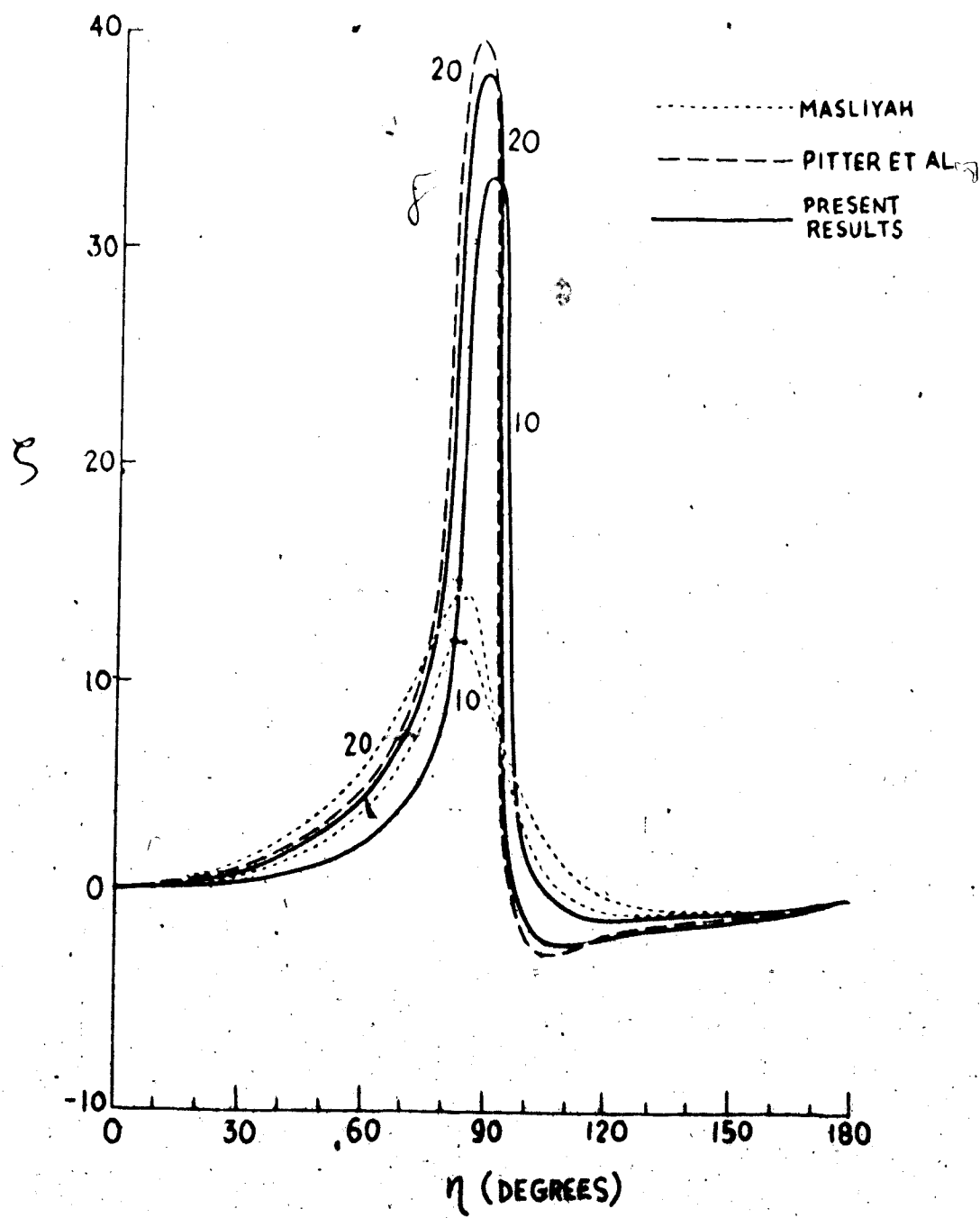


Fig. 5.1.5

Variation of the Surface Vorticity with
Polar Angle and Reynolds Numbers for
Oblate Spheroids

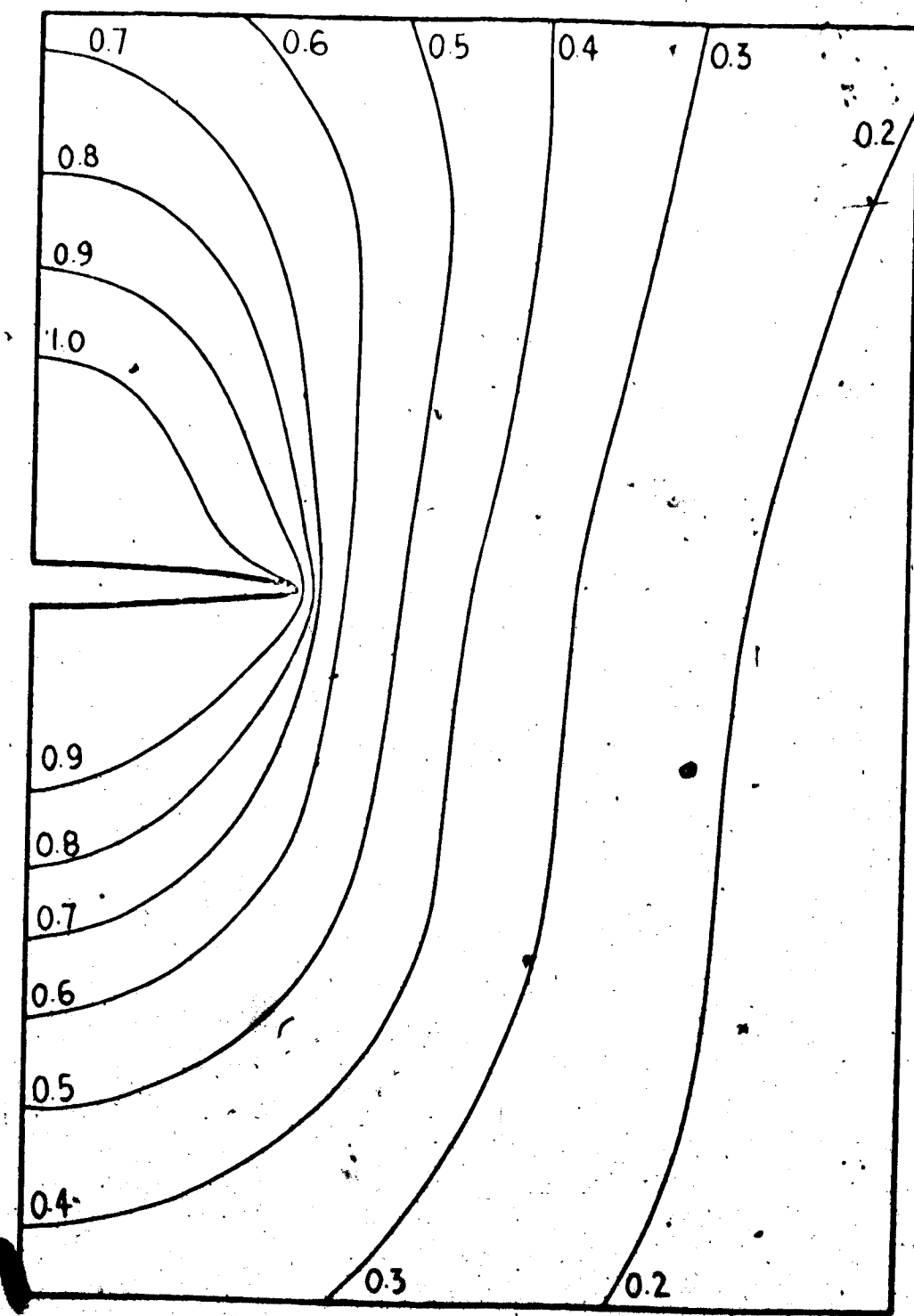


Fig. 5.1.6

Dimensionless Vertical Velocity of Air Passing Oblate Spheroid of $Re=10$.

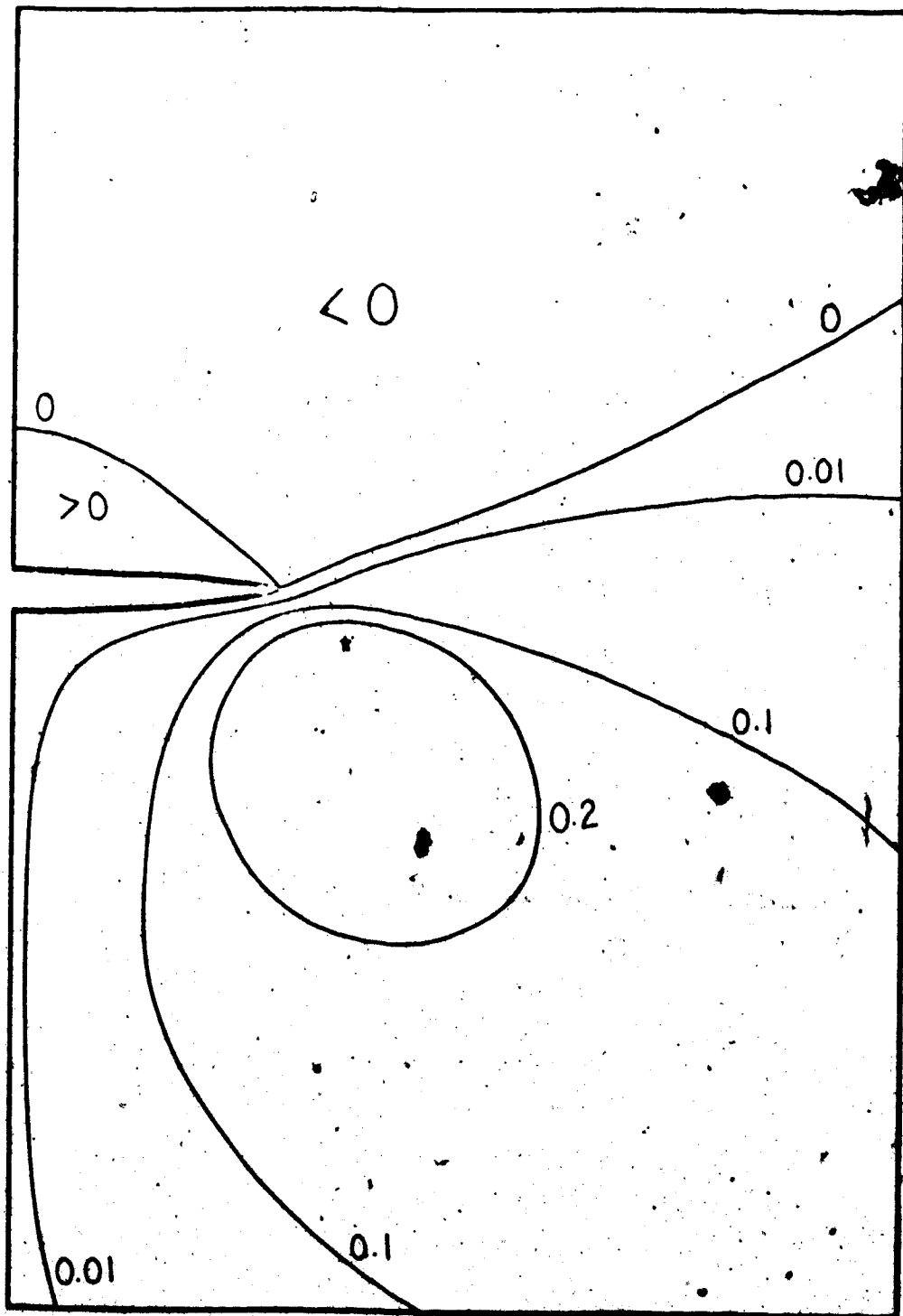


Fig. 5.1.7

Dimensionless Horizontal Velocity of Air

Passing an Oblate Spheroid of $Re = 10$

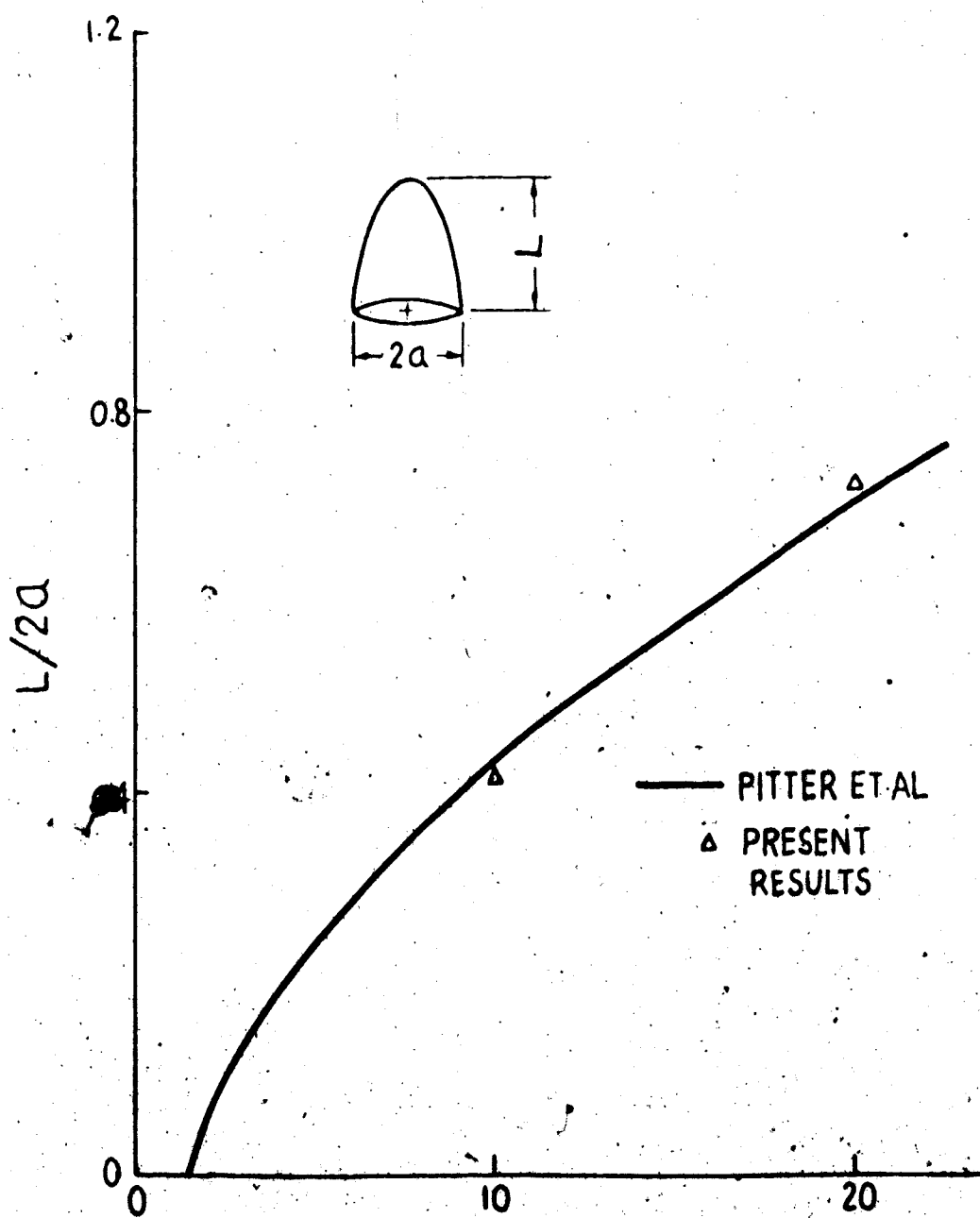


Fig. 5.1.8

Variation with Reynolds Number of the Length of
the Standing Eddy at the Downstream End of
Oblate Spheroids of Axis Ratio 0.05

5.2 Flow fields around spherical drops.

Wilkins and Auer (1970) in their field study of the riming properties of hexagonal ice crystals showed that the size distribution of droplets accreted on ice crystals of radius smaller than 400 microns lies in the range of 5 to 13 microns in radius. Fletcher (1969) suggests that the droplets in continental convective clouds have radii mainly smaller than 10 microns in range. Therefore, only spherical drops of Reynolds numbers smaller than 0.1 (radius less than 17 microns) are considered in this study.

Figures 5.2.1 and 5.2.2 represent the dimensionless stream function and vorticity fields of air passing a sphere of Reynolds number of 0.1. A summary of the radii, drag coefficients and terminal velocities of spheres of various Reynolds numbers in an atmosphere of -10°C and 700 mb are given in Table 5.2.1.

Reynolds Number	$10^4 \times \text{radius}$ (cm)	Terminal Vel (cm sec $^{-1}$)	Drag coeff from numer-	Drag coeff. Le Clair's cal method approx,
0.1	19.14	4.70	243.50	244.5
0.01	8.83	1.02	2399.93	2404.5
0.005	7.01	0.64	4802.89	4804.5

0.004	6.51	0.55	6010.93	6004.5
0.003	5.91	0.40	8001.38	8004.5

Table 5.2.1 Reynolds Number, Drag Coefficient, radius and Terminal Velocity of spherical Water Drops in Atmosphere of 10°C , 700 mb
 $(\rho = 9.267 \times 10^{-4} \text{ gm cm}^{-3},$
 $\mu = 1.667 \times 10^{-4} \text{ poise})$

Table 5.2.1 shows the two drag coefficient's calculated by the method discussed in section 3.3 using the analytic flow field solution for Stokes flow and the relation of drag coefficient and Reynolds number suggested by Le Clair et al (1970) for small speres of Reynolds number less than 0.1. The differences between the two methods are well within 1 percent.

5.3 Trajectories of Water Drops Relative to an Ice Oblate Spheroid.

The superposition method is employed with the ice spheroids of Reynolds numbers of 10 and 20, and water spheres of Reynolds number of 0.003, 0.004, 0.005, 0.01 and 0.1. The trajectories of a water sphere of 5.91 microns and of 19.14 microns radius (Reynolds number 0.003 and 0.1 respectively) interacting with an ice spheroid with semi-major axis of 396.3 microns (Reynolds number 20) are



Fig. 5.2.1

Dimensionless Stream Function of Sphere at $Re = 0.1$

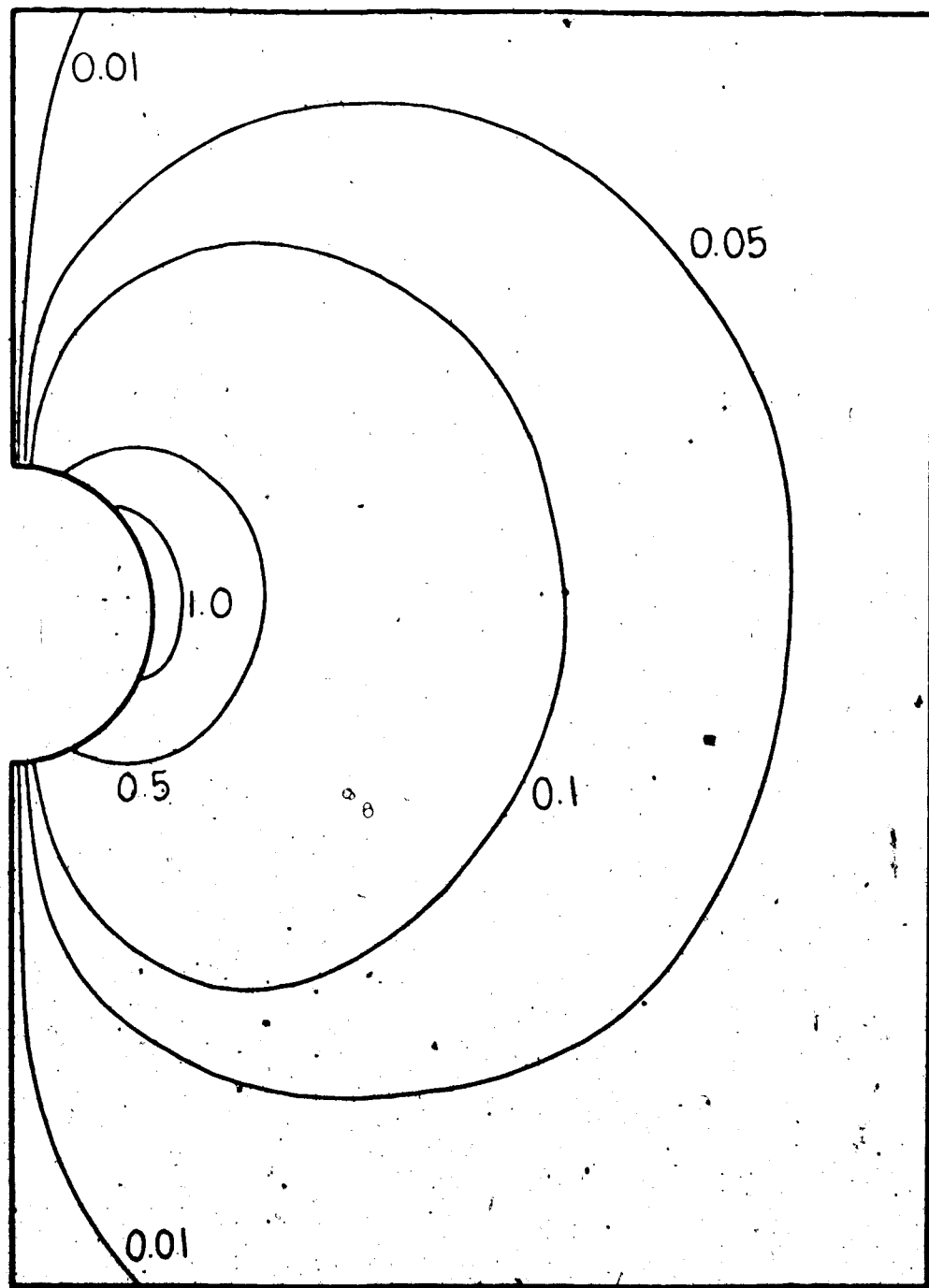


Fig. 5.2.2

Dimensionless Vorticity of a Sphere of $Re = 0.1$

plotted in figures 5.3.1 and 5.3.2. The curvature of the trajectories in all the cases of this study is not as great as those obtained by Pitter et al (1974) and the annular behaviour — no accretion of droplets in the center of the ice crystal, even for drops as small as 5.91 microns in radius, is not so predominant. This would be mainly due to the correction of the parameter Q_s , in equation 3.10, as a result of the change of velocity of the water drop.

When the ice oblate spheroid approaches the water drop, the velocity of the drop increases due to the fluid motion immediately surrounding the ice particle. As a result, the Reynolds number of the water sphere increases proportionally.

The Best number $C_D R e^2$ of a body moving in a fluid is a constant. If the Reynolds number of the water drop increases, the product of the drag coefficient and the Reynolds number decreases, i.e. the parameter Q_s reduces in magnitude.

Then the terminal velocity of the water sphere is never able to increase to the terminal velocity of the oblate spheroid before collision. Therefore the horizontal forces are not great enough to move a water sphere which approaches the center of the spheroid around the oblate spheroid.

In Pitter et al's study, the Reynolds number of the water sphere is assumed constant throughout the whole interaction.

The parameter Q_s is, therefore, held constant. The vertical and horizontal acceleration of the water sphere is then capable of becoming large enough to enable the drop to speed

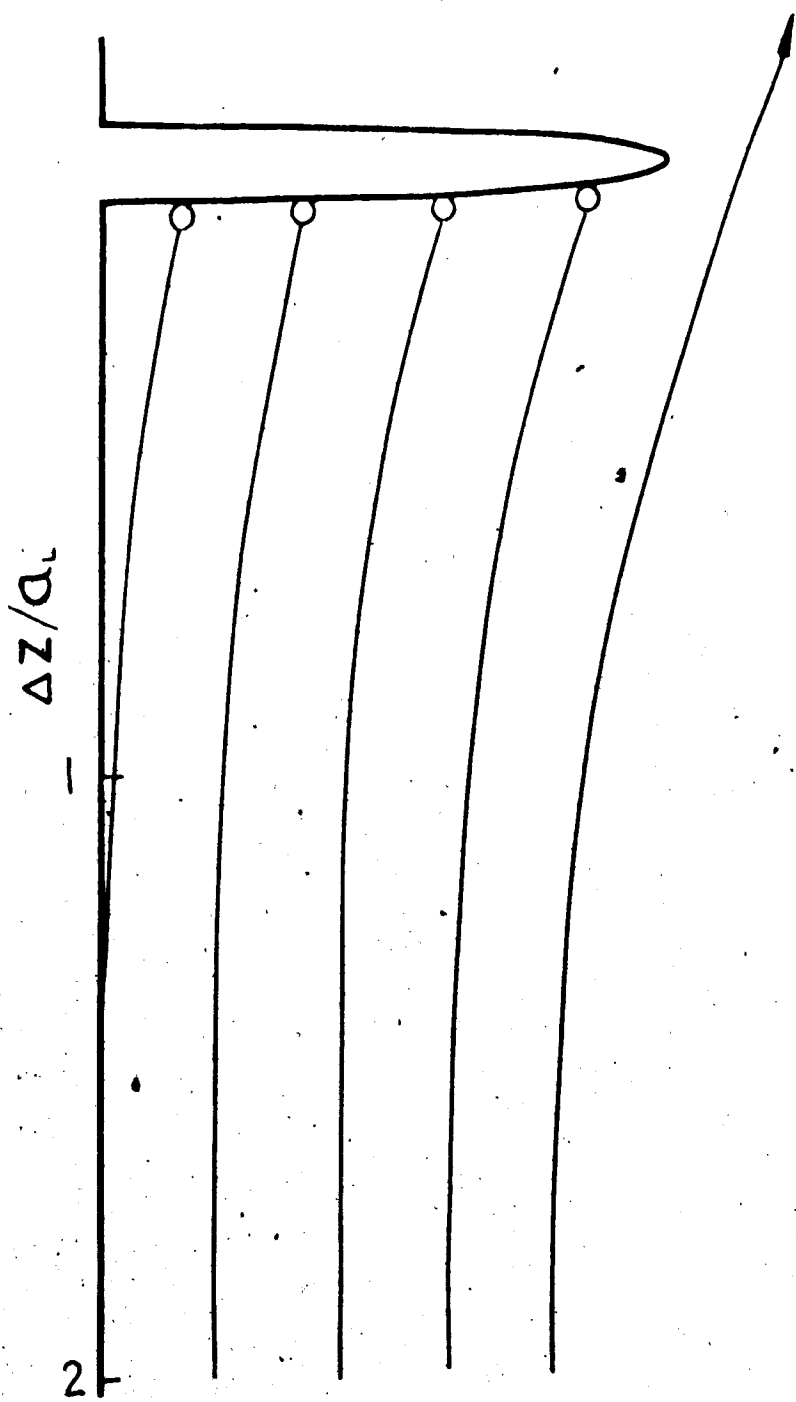


Fig. 5.3.1

Trajectories of 5.91 micron Water Drop Relative
to an Oblate Spheroid of ice of $Re = 20$

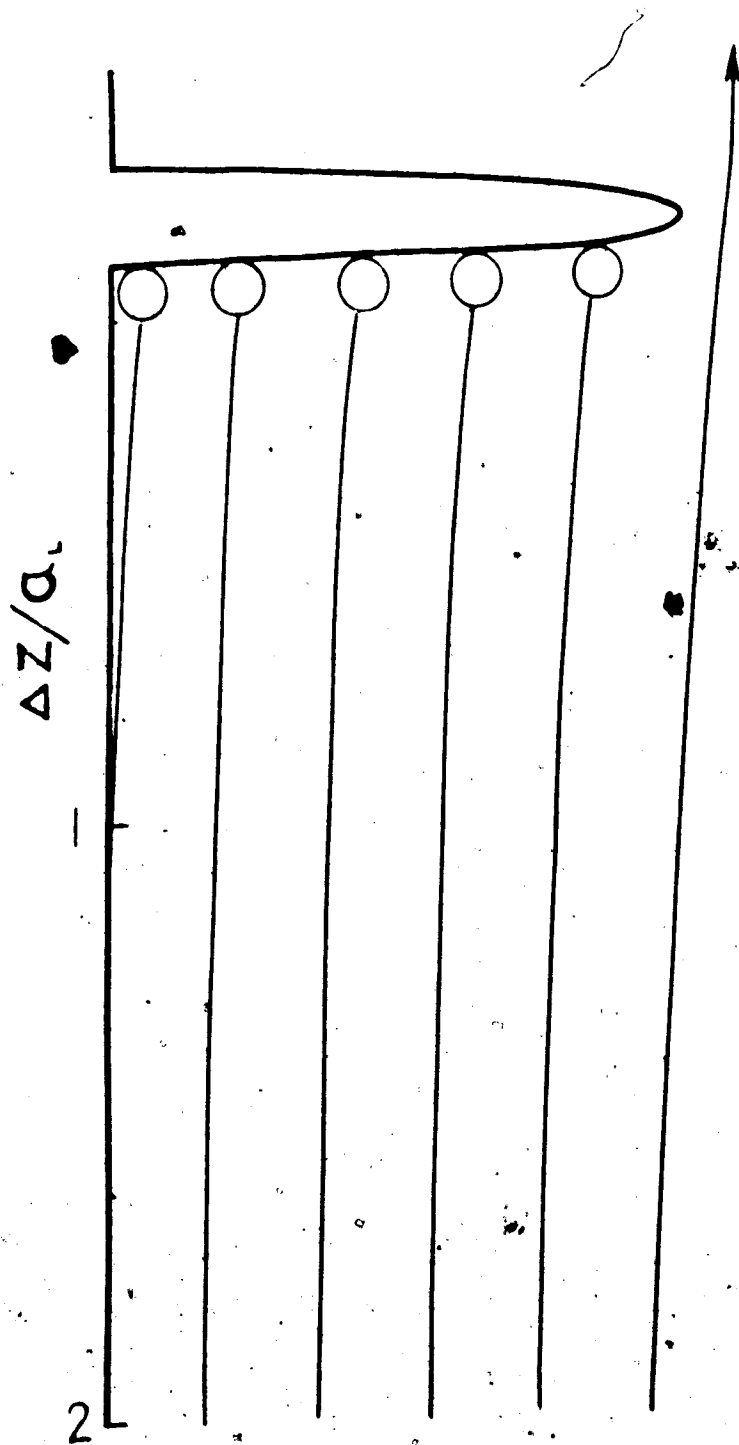


Fig. 5.3.2

Trajectories of 19.14 microns Water Drop

Relative to an Oblate Spheroid of Ice of Re

up and to go around the oblate spheroid of ice without collision.

The maximum angle that water drops of radius 5.91 microns formed when they collected at the outer edge of an oblate ice spheroid of Reynolds number 20 is drawn in figure 5.3.3. Figure 5.3.4 represents the variation of the outer maximum angles that water drops may create on oblate spheroids of Reynolds number 10 and 20 with various Reynolds numbers of water spheres. Since no water droplet which approaches the middle part of the ice crystal expelled around without collision occurred, the inner critical angle would no longer be of any importance and they are not recorded. The outer critical angle that water sphere would create on an oblate ice spheroid is rather large, but they are the maximum angle that the drop just touched the other drop. However, in the atmosphere, the second drop most likely cannot attach to a single drop adhered to the oblate spheroid of ice by just touching it. Therefore, the vertex angle that a graupel would have should be smaller than twice the maximum angle given above. The bigger the ice crystal and the smaller the cloud water droplet, the sharper would be the angle of the point of the graupel.

In all the cases of this study, no capture of water drops in the wake of an ice oblate spheroid is ever detected. Examining the vertical and horizontal isotachs

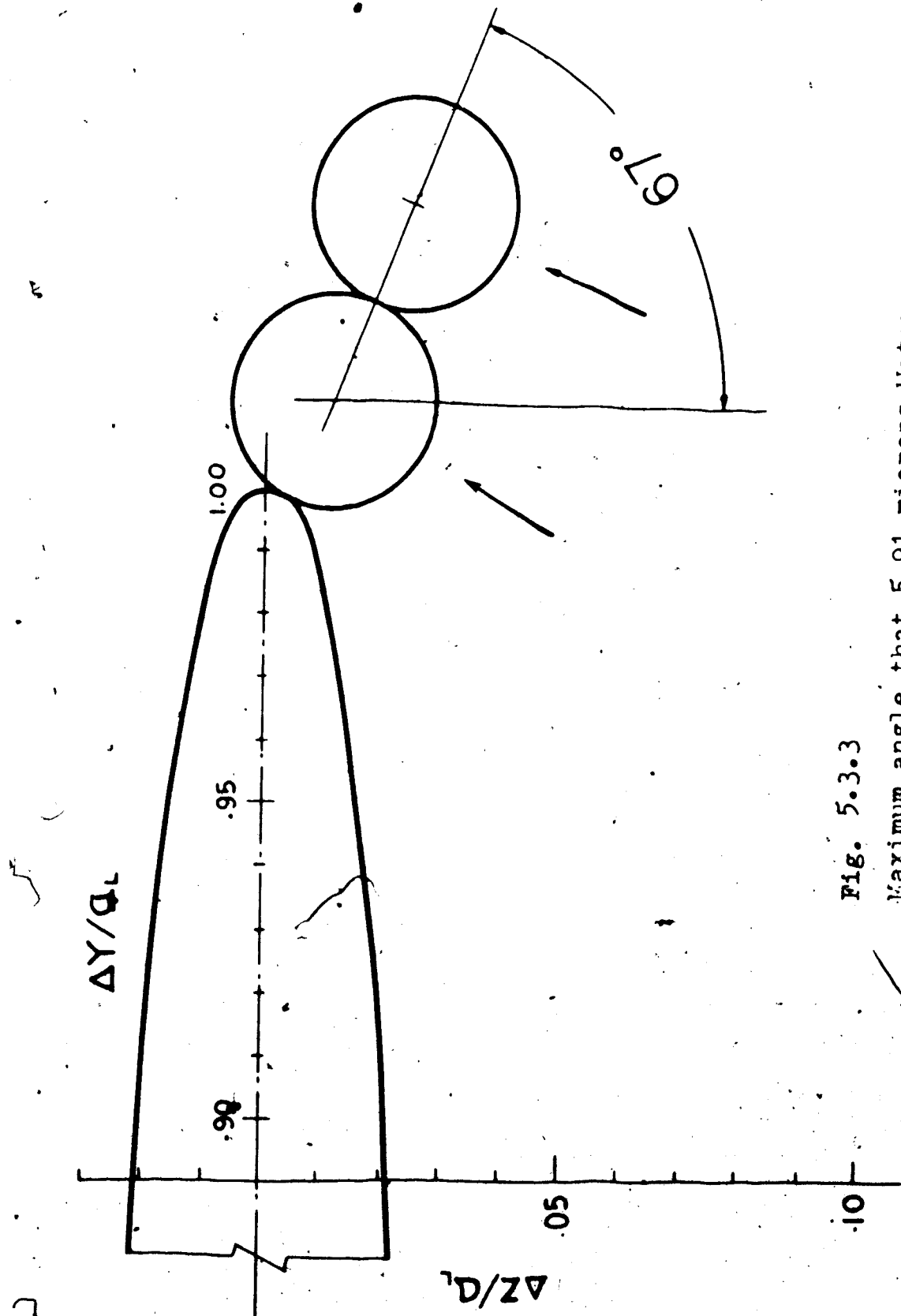


Fig. 5.3.3
Maximum angle that 5.91 microns Water
Drops forms on an Oblate Spheroid of $Re = 20$

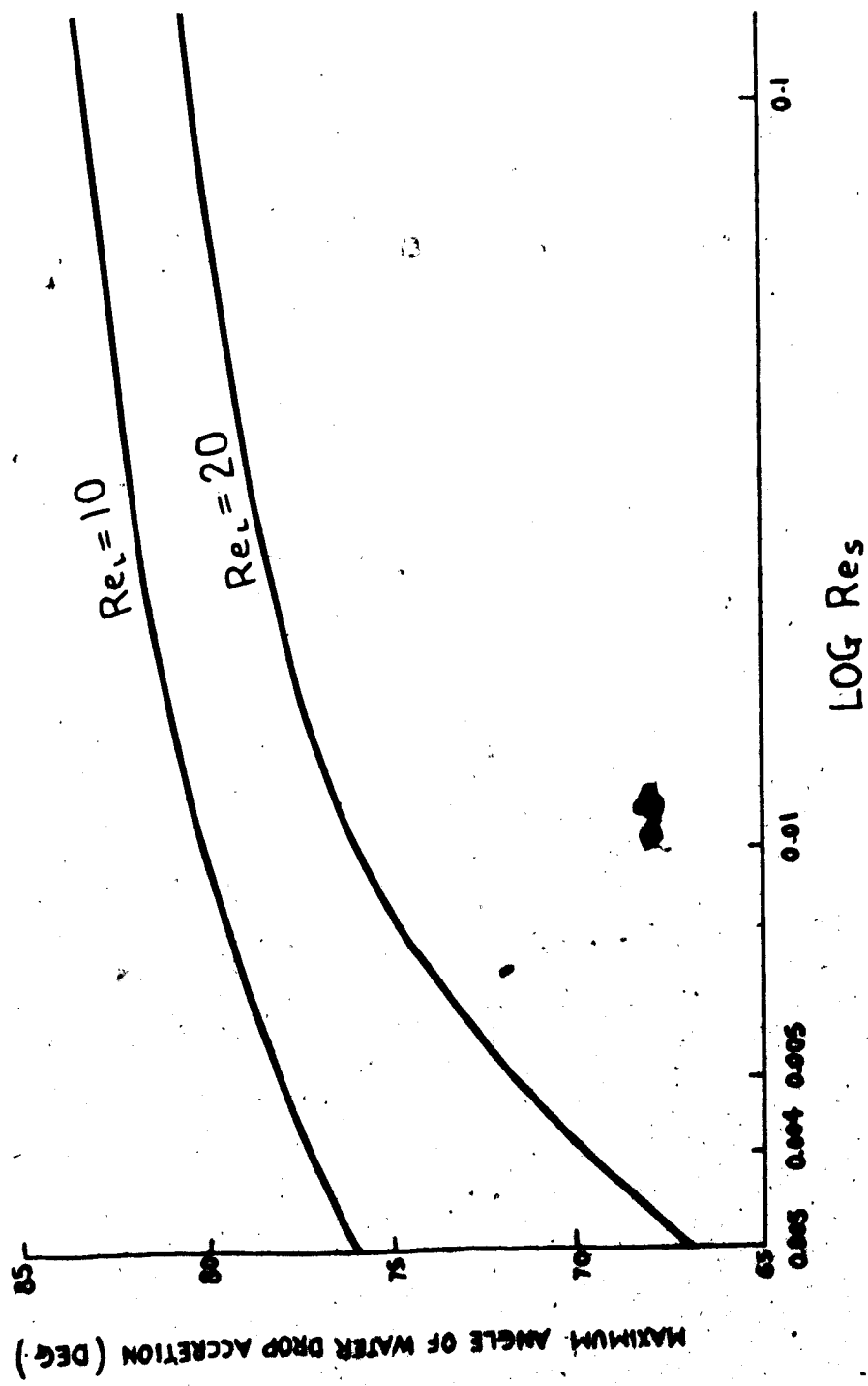


Fig. 5.3.4

Variation of Outer Maximum Angle that Water Drops of Various Reynolds Number Created on an Oblate Spheroid of $Re=20$ and $Re=10$.

plots in figures 5.1.6 and 5.1.7, when a very small water sphere passes the ice spheroid, there is a tendency to move the water sphere towards the axis of the ice particle and the vertical flow field at the rear of the ice body may push the water drop downward (i.e. back toward the trailing end of the spheroid). If the parameter Q_s in equation 3.10 still remains comparably very large after passing around the ice spheroid, it may be able to accelerate to a velocity to catch up with the larger particle which is in fact momentarily decelerating very slowly due to the flow field of the water drop. It will, however, soon regain its terminal velocity again. This may explain why the tip of a graupel is seen in laboratory studies to be formed by very small cloud droplets.

CHAPTER VI CONCLUSIONS AND RECOMMENDATION

The model made in this study was fairly successful though it only dealt with two dimensionals. Convergence to the steady-state Navier-Stokes equation was slow. The computing time was therefore very long, up to 30 minutes CPU time in the IBM 360 computer of the University of Alberta. 1581 grid-point values for the thin oblate spheroids of ice and 4941 grid-point values for the spherical water drop were evaluated to get the flow field. However, the model preliminarily revealed the following:

- (1) The length of the wake formed at the down-stream end of the ice crystal is longer for higher Reynolds numbers.
- (2) For small Reynolds number (5.1), the drag coefficient can be successfully approximated by the expression: $C_D = \frac{24}{Re} \left(1 + \frac{3}{16} Re\right)$.
- (3) Water drops of Reynolds number 0.003 to 0.1 approaching a thin oblate spheroid of ice of Reynolds number 10 or 20 would not pass around the ice particle without collision.
- (4) This study suggests that ice crystals appear to accrete droplets primarily on their upstream side. This supports the theory of graupel growth suggested by List as discussed in section 1.3.

- (5) No wake capture was found in this study.
- (6) The maximum angle that water drops would accrete on an ice crystal's edge depends on both the size of the crystal and that of the droplet. Small crystals and big droplets give larger angles of riming growth beyond the edge of the ice crystals.

Since only minimal annular behaviour was detected when an ice crystal was approximated by a thin oblate spheroid, the theory of the formation of conical graupel at the points and the edge of hexagonal plates as hypothesized by Knight and Knight could not be further justified. The collision efficiency is no doubt greater along the edge. Trajectories showing droplets passing around the ice particle as obtained by Pitter were not found. The reason of this discrepancy was explained earlier.

In order to fully understand the growth of graupel, a three dimensional model should be used instead — that is, a hexagonal plate should be used rather than an oblate spheroid. The boundary conditions at the corners and along the sharp edges of the hexagonal plate may first have to be investigated by experimental technique. This is important as the corner effects would affect the flow field drastically. Another numerical method should be used instead of the finite differencing method used in this study. The finite differencing scheme is rather slow and

a convenient co-ordinate system is hard to seek for a hexagonal plate. The best alternate numerical method would be the finite element method. This scheme deals in infinitesimal area but not in grid-points. It is faster in converging and it can deal with a three dimensional object of any shape in simple Cartesian coordinate system. The superposition model would be still valid provided the mass ratio is small. The flow field around the ice crystal, after a water drop is adhered on it, would be better calculated again. For the finite element method, this procedure would not be a hazard since the scheme, as mentioned before, is suitable for an object of any shape and the computation time is far shorter than the finite differencing method. If possible, the range of water droplets under study should be enlarged so that the feasibility of wake capture would be fully investigated.

BIBLIOGRAPHY

Aoi, T. : The steady flow of viscous fluid past a fixed spheroidal obstacle at small Reynold number.

J. Phys. Soc. Japan, 10, 119 1955.

Arenberg, D.L.: The formation of small hail and snow pellets.

Bull. Amer. Meteor. Soc., 22, 113-116, 1941.

Atkinson, B.; Brocklebank, M.P.; Card, C.C.M.; and Smith, J.M.: Low Reynold numbers developing flows.

A.I.Ch. Eng. J., 15, 548-53, 1969.

Breath, D.R.: Slow flow past ellipsoids of revolutions.

J. of Fluid Mech., 10, 306-314, 1961.

Fletcher, N.H.: The Physics of Rainclouds.

Cambridge University Press, 1969.

Flogel W.: Ferner Zur. Kenntnis der Struktur des Hagels.

Met. Zeits, 116, 1877.

Gerald, C.F.: Applied Numerical Analysis.

Addison-Wesley Publishing Company, 1970.

Goldstein, S.: The forces on a solid body moving through a viscous fluid.

Proc. Roy. Soc., London, A 123, 216-235, 1929.

Hamielec, A.E.; Storey, S.H.; and Whitehead, J.M.: Viscous flow around fluid spheres at intermediate Reynolds number (II)

Can. J. Chem. Eng., 41; 246, 1963.

----- and Johnson, A.I.: Viscous flow around fluid spheres at intermediate Reynolds number

Can. J. Chem. Eng., 40, 41, 1962.

----- ; Hoffman, T.W.; and Ross, L.L.: Numerical solution of the Navier-Stokes equation for flow past spheres. Part I. Viscous flow around spheres with and without radial mass efflux.

A.I. Ch. E. Journal, 212 - 219, March, 1967.

Heymsfield, A.: Ice crystal terminal velocities
Technical note No. 41, Cloud Phys. Lab., U. of Chicago.

Hindman II, E.E.; and Johnson, D.B.: Numerical simulation of ice particle growth in a cloud of supercooled water droplets.

J. Atmos. Sci., 29, 1313 - 1321, 1972.

Hocking, L.M.: The collision efficiency of small drops.
Quart. J. Roy. Meteor. Soc., 85, 44 - 50, 1959.

----- ; and Jonas, P.R.: The collision efficiency of small drops.

Quart. J. Roy. Meteor. Soc., 96, 722 - 729, 1970.

Holroyd III, E.W.: A suggested origin of conical graupel.

J. Appl. Meteor. 3, No. 5, 633 - 636, 1964.

James, M.L.; Smith, G.M.; and Wolford, J.C.: Applied numerical methods for digital computation with Fortran.

International Textbook Company, Scranton, Pennsylvania.

Jayaweera, K.O.L.F.; and Cottis, P.E.: Fall velocity of plate-like and columnar crystals.

Quart. J. Roy. Meteor. Soc., 95, 703 - 709, 1969.

Jenson, V.G.: Viscous flow around a sphere at low Reynolds number.

Proc. Roy. Soc., A249, 346, 1959.

Knight, C.A.; and Knight, N.C.: Conical Graupel.

J. Atmos. Sci., 30, 118 - 124, 1973.

----- : Hailstone Embryos.

J. Atmos. Sci., 27, 659 - 666, 1970.

----- : Drop freezing in clouds.

J. Atmos. Sci., 31, 1174 - 1175, 1974.

Le Clair, B.P.; and Hamielec, A.E.: An numerical study of the drag on a sphere at low and intermediate Reynolds numbers.

J. Atmos. Sci., 27, 308 - 315, 1970.

List, R.: Kennzeichen atmosphärischer Eispartikeln, I.

Teil. Graupeln als Wachstumszentren von Hagelkörnern.

Z. Angew. Phys., 9A, 180 - 192, 1958.

----- Growth and structure of graupel and hailstones.

Geophys. Monogr., 5, 317 - 324, 1960.

----- ; and Schemenauer, R.S.: Free fall behavior of planar snow crystals, conical graupel and small hail.

J. Atmos. Sci., 28, 110 - 115, 1971.

Macklin, W.C.; Merlival, L.; and Stevenson, C.M.: The analysis of a hailstone.

Quart. J. Roy. Meteor. Soc., 96, 472 - 486, 1970.

Maruyama, H.: On conical graupel and its density.

Paper in Meteorology and Geophys. (Japan), 91, No. 1, 101 - 108, 1968.

Masliyah, J.H.; and Epstein, N.: Numerical study of steady flow past spheroids.

J. Fluid Mech., 44, 493 - 512, 1970.

----- : Symmetric flow past orthotropic bodies, single and clusters.

Ph. D. Thesis, University of British Columbia, 1970.

Mason, B.J. : The Physics of clouds.

Clarendon Press, Oxford, 1971.

Michael, P.: Steady motion of a disk in a viscous fluid.

Phys. Fluids, 2, 466 - 471, 1969.

Nakaya, U.: The formation of ice crystals.

Compendium of Meteorology, Amer. Meteor. Soc.,
207 - 220, 1951.

Oseen, C.W.: Über den widerstand gegen die gleichmassige
Translation eines Ellipsoides in einer reibenden
Flüssigkeit.

Arch. Math. Phys., 24, 108 - 114, 1915.

Pitter, R.L.; Pruppacher, H.R.; and Hamielec, A.E.: A
numerical study of viscous flow past a thin oblate
spheroid at low and intermediate Reynolds number.

J. Atmos. Sci., 30, 125 - 134, 1973.

----- : A numerical investigation
of collision efficiencies of simple ice plate-
colliding with supercooled water drops.

J. Atmos. Sci., 31, 551 - 559, 1974.

----- ; Hamielec, A.E.: A numerical
study of the effect of forced convection on
mass transport from a thin oblate spheroid of ice.

J. Atmos. Sci., 31, 1058 - 1066, 1974.

Proudman, I.; and Pearson, J.R.A.: Expansions at small Reynolds number for the flow past a sphere and a circular cylinder.

J. of Fluid Mech., 2, 237 - 262, 1957.

Reynolds, O.: Formation of rain drops and hailstones.

Nature, 15, 163 - 165, 1876.

Rimon, Y.; and Lugt, H.L.: Laminar flow past oblate spheroids of various thickness.

Phys. Fluid, 12, 2465 - 2472, 1969.

Sampson, R.: Phil. Trans. Roy. Soc., 182, 449, 1891.

Sasyo, Y.: Study of the formation of precipitation by the aggregation of snow particles and the accretion of cloud droplets on snowflakes.

Papers in Meteor. and Geophys. (Japan), 22, 62 - 142, 1971.

Schaefer, V.J.: Snow and its relationship to experimental meteorology.

Compendium of Meteor., Amer. Meteor. Soc., 221 - 234, 1951.

Schlichting, H.: Boundary Layer Theory.

4th ed., McGraw-Hill, New York, 1955.

Shafrir U.; and Gal-Chen, T.: A numerical study of collision efficiencies and coalescence parameters

for droplet pairs with radii up to 300 microns.

J. Atmos. Sci., 28, 741 - 751, 1970.

Snyder, L.J.; Spriggs, T.W.; and Stewart, W.E.: Solution of the equations of change by Galerkin's Method.

A.I. Ch. E. J., 10, 535, 1964.

Steinberger, D.H.; Pruppacher, H.R.; and Neiburger, M.: On the hydrodynamics of pairs of spheres falling along their line of centers in a viscous medium.

J. Fluid Mech., 34, 808 - 819, 1968.

Wilkins, P.D.; and Auer, A.H.: Rimming properties of hexagonal ice crystals.

Reprints Conf. Cloud Phys., Amer. Meteor. Soc., Fort Collins, Colo., 81 - 82, 1970.

Zienkiewicz, O.C.: The Finite Element Method in Engineering Science.

McGraw-Hill, London, 1971.

Zirkmunda, J.: and Vali G.: Fall patterns and fall velocities of rimed ice crystals.

J. Atmos. Sci., 29, 1334 - 1347, 1972.

Woo, S. W. : Ph. D. Thesis, McMaster University, Hamilton, Canada, 1971.

APPENDIX I

COMPUTER PROGRAM FOR SOLUTION OF FLOW PAST
AN OBLATE SPHEROID.

COMPUTATION OF THE ELECTRIC FIELD AROUND AN ELLIPTIC SPHEROID

*SINH2 (J) , COSH2 (J) , SINH (J) , COSH (J) ,
 *COS2A (J) , SIN2A (J) , SIN (J) , COS (J) ,
 *VO (J) , RACRS (J) , RACSC (J) , RACTS (J)
 *R2 (40) , R7 (40)

$R^2 = 1.0$

$R^2 E = 1.0$

$R^2 E G = 0.001$

$R^2 E I = 0.001$

$\delta = 0.1$

$R = 1.0 \times 10^{-6} / 100$

$A = 0.05$

$Z = A103 ((1.0 + ((1.0 + A) / (1.0 - A)))$

$SINH (Z) = SINH (Z)$

$COSH (Z) = COSH (Z)$

$SIN (Z) = SIN (Z)$

$COS (Z) = COS (Z)$

$SINH2 = SINH (Z) * SINH (Z)$

$SINH2 = SINH (Z) * SINH (Z)$

$COSH2 = COSH (Z) * COSH (Z)$

$COSH2 = COSH (Z) * COSH (Z)$

$SIN = SIN (Z) / SINH (Z)$

DO 1 J=1,31

$ZI = ZIA + 1.0 / (J-1) * A$

$SINH (J) = SINH (ZI)$

$COSH (J) = COSH (ZI)$

$COSH2 (J) = SINH (J) * SINH (J)$

$SINH2 (J) = SINH (J) * SINH (J)$

$C1 (J) = (2.0 - A * SINH2 (J)) / COSH2 (J) / 2.0 / E / C5 / A$

$C2 (J) = (2.0 + A * SINH2 (J)) / COSH2 (J) / 2.0 / E / A / C5$

$RACSC (J) = 1.00 / COSH2 (J)$

CONTINUE

DO 2 I=1,31

$BSU = B * PI * C1 (I-1)$

$BSV (I) = SIV (I-1)$

$COS (I) = COS (BSU)$

$SINA (I) = SIV (I) * SIN (I)$

$COS2A (I) = COS (I) * COS (I)$

CONTINUE

DO 10 I=2,30

$C3 (I) = (2.0 - B / SINA (I)) * COSA (I) / 2.0 / B / B / C5$

$C4 (I) = (2.0 + B / SINA (I)) * COSA (I) / 2.0 / B / B / C5$

$RACRS (I) = RACSC / SINA (I)$

CONTINUE

DO 3 I=1,31

READ (1,999) (REL (I,J), J=1,51)

CONTINUE

DO 4 I=1,31

READ (2,999) (VO (I,J), J=1,51)

CONTINUE

DO 5 J=1,51

DO 5 I=1,31
 $GL(I,J) = V0(I,J) * \text{COSH}(J) * \text{SINA}(I) / \text{COSH}Z$
 CONTINUE
 IFLAG=1
 DO 6 J=1,50
 L_0
 $IP(1-IFLAG) 11,90,91$
 30 DO 8 I=2,20
 $IF(I-2) 20,31,30$
 21 DO 21 J=2,50
 $RFL = FEL(I,J+1) * C1(J) + FEL(I,J-1) * C2(J) + FEL(I+1,J) * C3(I)$
 $* + FEL(I-1,J) * C4(I) - GL(I,J) * SECHE/C5 * (\text{SINH2}(J) + \text{COS2A}(I))$
 $D1L = RGL - FEL(I,J)$
 $FEL(I,J) = FEL(I,J) + D1L * PUFF$
 $RGL = GL(I,J+1) * C1(J) + GL(I,J-1) * C2(J) + GL(I+1,J) * C3(I)$
 $* + GL(I-1,J) * C4(I) - RACRC(I) * \text{SINA}(I) * ((FEL(I,J+1) - FEL(I,J-1))$
 $* * (GL(I+1,J) / B / SIN2A(I+1) - GL(I,J) / B / SIN2A(I))) + RACRS(I) * \text{COSHA}(J)$
 $* * ((FEL(I+1,J) - FEL(I-1,J)) * (GL(I,J+1) / COSH2(J+1) - GL(I,J-1)$
 $* / COSH2(J-1)))$
 $D1L = RGL - GL(I,J)$
 $GL(I,J) = GL(I,J) + D1L * PUFF$
 $IF(1-10(D1L).LT..001.AND.ABS(D1L).LT..001) L=L+1$
 CONTINUE
 GO TO 3
 30 IF(I-20) 32,32,32
 32 DO 22 J=2,50
 $RFL = FEL(I,J+1) * C1(J) + FEL(I,J-1) * C2(J) + FEL(I+1,J) * C3(I)$
 $* + FEL(I-1,J) * C4(I) - GL(I,J) * SECHE/C5 * (\text{SINH2}(J) + \text{COS2A}(I))$
 $D1L = RGL - FEL(I,J)$
 $FEL(I,J) = FEL(I,J) + D1L * PUFF$
 $RGL = GL(I,J+1) * C1(J) + GL(I,J-1) * C2(J) + GL(I+1,J) * C3(I)$
 $* + GL(I-1,J) * C4(I) - RACRC(I) * \text{SINA}(I) * ((FEL(I,J+1) - FEL(I,J-1))$
 $* * (GL(I+1,J) / B / SIN2A(I+1) - GL(I,J) / SIN2A(I-1))) + RACRS(I) * \text{COSHA}(J)$
 $* * ((FEL(I+1,J) - FEL(I-1,J)) * (GL(I,J+1) / COSH2(J+1) - GL(I,J-1)$
 $* / COSH2(J-1)))$
 $D1L = RGL - GL(I,J)$
 $GL(I,J) = GL(I,J) + D1L * PUFF$
 $IF(1-10(D1L).LT..001.AND.ABS(D1L).LT..001) L=L+1$
 CONTINUE
 GO TO 3
 33 DO 23 J=2,50
 $RFL = FEL(I,J+1) * C1(J) + FEL(I,J-1) * C2(J) + FEL(I+1,J) * C3(I)$
 $* + FEL(I-1,J) * C4(I) - GL(I,J) * SECHE/C5 * (\text{SINH2}(J) + \text{COS2A}(I))$
~~REPL = FEL(I,J)~~
~~REPL = FEL(I,J) + D1L * PUFF~~
~~RGL = GL(I,J+1) * C1(J) + GL(I,J-1) * C2(J) + GL(I+1,J) * C3(I)~~
~~* + GL(I-1,J) * C4(I) - RACRC(I) * \text{SINA}(I) * ((FEL(I,J+1) - FEL(I,J-1))~~
~~* * (GL(I,J) / B / SIN2A(I) - GL(I-1,J) / SIN2A(I-1))) + RACRS(I) * \text{COSHA}(J)~~
~~* * ((FEL(I+1,J) - FEL(I-1,J)) * (GL(I,J+1) / COSH2(J+1) - GL(I,J-1)~~
~~* / COSH2(J-1)))~~
 $D1L = RGL - GL(I,J)$
 $GL(I,J) = GL(I,J) + D1L * PUFF$
 $IF(1-10(D1L).LT..001.AND.ABS(D1L).LT..001) L=L+1$
 CONTINUE
 CONTINUE
 IFLAG=2
 GO TO 70

```

21      DO 45 J,J=1,15
         J=51+1-JJ
         D=15.1741,15
         T=51+1-TI
         I=(I-15)-40,-1,40
41      REFL=EL(I,I+1)*C1(J)+FEL(I,J-1)*C2(J)+FEL(I+1,J)*C3(I)
         *+FEL(I-1,J)*C4(I)-GL(I,J)*SINH2/C5*(SINH2(J)+COS2A(I))
         D1L=REFL-FEL(I,J)
         FEL(I,J)=REFL(I,J)+D1L*SINFG
         RGL=GL(I,J+1)+C1(J)+GL(I,J-1)*C2(J)+GL(I+1,J)*C3(I)
         *+GL(I-1,J)*C4(I)-PACPC(I)*SINA(I)*((FEL(I,J+1)-FEL(I,J-1))
         **(GL(I,J)/B/SINA(I)-GL(I-1,J)/SINA(I-1)))+PACRS(I)*COSH(A(J)
         **((FEL(I+1,J)-FEL(I-1,J))*((GL(I,J+1)/COSH2(J+1)-GL(I,J-1)
         */COSH2(J-1)))
         D2L=RGL-GL(I,J)
         GL(I,J)=GL(I,J)+D2L*SINFG
         IF(ABS(D2L).LT..001.AND.ABS(D2L).LT..001)L=L+1
         GO TO 15
40      IF(I-2)42,43,42
42      REFL=FEL(I,I+1)*C1(J)+FEL(I,J-1)*C2(J)+FEL(I+1,J)*C3(I)
         *+FEL(I-1,J)*C4(I)-GL(I,J)*SINH2/C5*(SINH2(J)+COS2A(I))
         D1L=REFL-FEL(I,J)
         FEL(I,J)=REFL(I,J)+D1L*SINFG
         RGL=GL(I,J+1)*C1(J)+GL(I,J-1)*C2(J)+GL(I+1,J)*C3(I)
         *+GL(I-1,J)*C4(I)-PACPC(I)*SINA(I)*((FEL(I,J+1)-FEL(I,J-1))
         **(GL(I,J+1)/B/SINA(I+1)-GL(I-1,J)/B/SINA(I-1)))+PACRS(I)*COSH(A(J)
         **((FEL(I+1,J)-FEL(I-1,J))*((GL(I,J+1)/COSH2(J+1)-GL(I,J-1)
         */COSH2(J-1)))
         D2L=RGL-GL(I,J)
         GL(I,J)=GL(I,J)+D2L*SINFG
         IF(ABS(D2L).LT..001.AND.ABS(D2L).LT..001)L=L+1
         GO TO 15
43      REFL=FEL(I,J+1)*C1(J)+FEL(I,J-1)*C2(J)+FEL(I+1,J)*C3(I)
         *+FEL(I-1,J)*C4(I)-GL(I,J)*SINH2/C5*(SINH2(J)+COS2A(I))
         D1L=REFL-FEL(I,J)
         FEL(I,J)=REFL(I,J)+D1L*SINFG
         RGL=GL(I,J+1)*C1(J)+GL(I,J-1)*C2(J)+GL(I+1,J)*C3(I)
         *+GL(I-1,J)*C4(I)-PACPC(I)*SINA(I)*((FEL(I,J+1)-FEL(I,J-1))
         **(GL(I,J+1)/B/SINA(I+1)-GL(I,J)/B/SINA(I)))+PACRS(I)*COSH(A(J)
         **((FEL(I+1,J)-FEL(I-1,J))*((GL(I,J+1)/COSH2(J+1)-GL(I,J-1)
         */COSH2(J-1)))
         D2L=RGL-GL(I,J)
         GL(I,J)=GL(I,J)+D2L*SINFG
         IF(ABS(D2L).LT..001.AND.ABS(D2L).LT..001)L=L+1
15      CONTINUE
45      CONTINUE
        IFLAG=1
70      DO 7 I=2,20
        GGT=(3.*PEL(I,2)-FFL(I,3))*COSH5/2./A/A/(SINH5+COS2A(I))
        GL(I,1)=(GGT-GL(I,1))*RSB+GL(I,1)
7       CONTINUE
        IF(L-1421)5,100,100
5      CONTINUE
100     WRITE(5,500) 2E,AP
        WRITE(5,501) N
        DO 9 I=1,31
          WRITE(9,502) (FEL(I,J),J=1,15)

```

WRITE(6,100) -(V0(I,J),J=1,51)

CONTINUE

DO 13 I=1,31

WRITE(6,504) -(V0(I,J),J=1,51,5)

CONTINUE

WRITE(6,505)

DO 11 J=1,51

DO 11 I=2,31

V0(I,J)=GL(I,J)*COSHZ/COSH(A(J))/SINA(I)

CONTINUE

DO 12 I=1,31

WRITE(6,507) (V0(I,J),J=1,15)

WRITE(6,503) (V0(I,J),J=1,51)

CONTINUE

DO 14 I=1,31

WRITE(6,504) -(V0(I,J),J=1,51,5)

CONTINUE

WRITE(6,505)

CDSKI=0.0

DO 110 I=1,29,2

CDSKI=SINA(I)**2*V0(I,1)+4.*SINA(I+1)**2*V0(I+1,1)+SINA(I+2)**2

*V0(I+2,1)+10.8E

CDSKI=CDSKI**B.0*SINHZ/COSH(A)/B5/2.*B

B1=0.0

DO 111 J=1,12,2

P1=P1+((V0(2,J)**-0.-V0(3,J))+4.* (V0(2,J+1)**4.-V0(3,J+1))+

*(V0(2,J+2)**-,-V0(3,J+2)))/2.0

CONTINUE

P1=1.0+2.*P1*A/3.*B*B*P1

P2(1)=0.0

SINA(33)=0.0

COSA(33)=0.0

PT(33)=0.0

DO 112 I=1,29,2

IIZ=I+2

P2(IZ)=((-V0(I,1)*3.0+4.0*V0(I,2)-V0(I,3))+(-V0(I+1,1)*3.0+4.0*V0(I+1,2)-V0(I+1,3))*4.0+(-V0(I+2,1)*3.0+4.0*V0(I+2,2)-V0(I+2,3)))/2./2.0+(V0(I,1)+V0(I+1,1)*4.0+V0(I+2,1))**SINHZ/COSH(A)+P0(I)

CONTINUE

P2(IZ)=P1+P2(IZ)*4.0/30/3.*B

P2(1)=P1

CDFOP=0.0

DO 113 I=1,29,4

CDFOP=CDFOP*PT(I)*COSA(I)*SINA(I)*2.+8.*COSA(I+2)*PT(I+2)

*SINA(I+2)+2.*PT(I+4)*SINA(I+4)*COSA(I+4)

CDFOP=CDFOP*B/1.5

CDTTP=CDSKI+CDFOP

WRITE(6,506)

WRITE(6,507) RE,CDSKI,CDFOP,CDTTP,P1

WRITE(6,503) (PT(I),I=1,31,2)

AMU=1.667E-4

AIRLO=.9267E-3

CPYLO=.92

RLRSQ=3.*AMU**2/AIRLO/(CRYLO-AIRLO)*PE**2/32.*CDTTP/980./A2

RLF=RLRSQ**(.1./3.)

VTERM=AMU*RE/2./RLP/AIRLO

RLH=RLR*10000.

```

103
401 TE(6,702)
402 TE(6,509) MMH,TELD,TEYLD,AF
403 TE(6,510) TLD,VTR-M
404 FORMAT(13,5.4)
500 FORMAT(//,1X,'YN-10'//,16.16,F=1.5E.2,1, AXIS RATIO =1.5E.3)
501 FORMAT(//,1X,'THE FOLLOWING REQUESTED')
502 FORMAT(//,1X,10.5.3)
503 FORMAT(//,1X,'THE VORTICITY FIELD')
504 FORMAT(//,11E10.4)
505 FORMAT(//,1X,'TOTAL SCOD VALUES = ',I5)
506 FORMAT('1',1X,'REYNOLD NO',9X,'CDSKIN',10X,'CDFORM',10X,
* 'CDTET',13X,'PCD')
507 FORMAT(//,5E13.5)
508 FORMAT(//,10X,'VISCOSITY',3X,'AIR DENSITY',8X,'CRYO DENSITY',
* 3X,'AXIS RATIO'),
509 FORMAT(//,4E20.5)
510 FORMAT(//,1X,'ADVIS=1,F3.2,TER=1,VEL=1,P2.4)
STOP
END

```

APPENDIX II

COMPUTER PROGRAM FOR SOLUTION OF FLOW PAST A
SPHERE.

C CALCULATION OF FLOW FIELD AROUND A SPHERE ****
 DIMENSION C3(61), C4(61), PE(61,81), G(61,81), V(61,81), F(61,81)
 *, SINPI(61), COSPI(61), EXPZ(81), EXPZZ(81), SINPI2(61),
 *PT(65), P2(65) ✓
 RE=.1
 PF=1.5
 PG=0.2
 B=3.*3.1416/180.
 A=.05
 C5=2./A/A+2./B/B
 DO 2 J=1,81
 Z=B*FLOAT(J-1)
 EXPZ(J)=EXP(Z)
 EXPZZ(J)=EXPZ(J)*FX?Z(J)
 2 CONTINUE
 C1=(2.-A)/2./A/A/C5
 C2=(2.+A)/2./A/A/C5
 SINPI(1)=0.0
 COSPI(1)=1.0
 SINPI2(1)=0.0
 SINPI(61)=0.0
 COSPI(61)=1.0
 SINPI2(61)=0.0
 DO 3 I=2,60
 PI=B*FLOAT(I-1)
 SINPI(I)=SIN(PI)
 COSPI(I)=COS(PI)
 SINPI2(I)=SINPI(I)*SINPI(I)
 COTPI=COSPI(I)/SINPI(I)
 C3(I)=(2.-B*COTPI)/2./B/B/C5
 C4(I)=(2.+B*COTPI)/2./B/B/C5
 3 CONTINUE
 P1=1.0/EXPZ(81)
 P3=P1*R1*P1
 P6=P3*P3
 D=2.* (2.*P6-10.-10.*P3+10.*P1)
 DO 6 J=1,81
 DO 6 I=1,61
 PE(I,J)=(FXPZZ(J)/2.+.25/EXPZ(J)-.75*EXPZ(J))*SINPI2(I)
 G(I,J)=15./D/EXPZ(J)*SINPI2(I)*(P3*EXPZ(J)**3-1.0)*2.0
 6 CONTINUE
 DO 4 I=1,61
 PE(I,81)=EXPZZ(81)*SINPI2(I)/2.
 4 CONTINUE
 DO 15 I=2,60
 DO 15 J=1,81
 F(I,J)=G(I,J)/EXPZZ(J)/SINPI2(I)
 15 CONTINUE
 DO 5 J=1,81
 V(1,J)=0.0
 V(61,J)=0.0
 F(1,J)=0.0
 F(61,J)=0.0

```

CONTINUE
IFLAG=1
DO 7 N=1,100
L=0.
IF (IFLAG.EQ.2) GO TO 20
DO 2 I=1,60
DO 2 J=2,90
RFE=FE(I,J+1)*C1+FE(I,J-1)*C2+FE(I+1,J)*C3(I)+FE(I-1,J)
**C4(I)-G(I,J)*EXP2Z(J)/C5
RG=G(I,J+1)*C1+G(I,J-1)*C2+G(I+1,J)*C3(I)+G(I-1,J)*C4(I)
*-RF*EXP2Z(J)*SINFI(I)/(8.*A*B)*((FE(I,J+1)-FE(I,J-1))
**(F(I+1,J)-F(I-1,J)))
*-(FE(I+1,J)-FE(I-1,J))**(F(I,J+1)-F(I,J-1)))/C5
D1=RFE-FE(I,J)
D2=RG-G(I,J)
IF (ABS(D1).LT..001.AND.ABS(D2).LT..001) L=L+1
FE(I,J)=FE(I,J)+FE*D1
G(I,J)=G(I,J)+FG*D2
F(I,J)=G(I,J)/EXP2Z(J)/SINFI(I)
CONTINUE
IFLAG=2
GO TO 60
20 DO 21 JJ=2,80
J=82-JJ
DO 21 II=2,60
I=62-II
RFE=FE(I,J+1)*C1+FE(I,J-1)*C2+FE(I+1,J)*C3(I)+FE(I-1,J)
**C4(I)-G(I,J)*EXP2Z(J)/C5
RG=G(I,J+1)*C1+G(I,J-1)*C2+G(I+1,J)*C3(I)+G(I-1,J)*C4(I)
*-RF*EXP2Z(J)*SINFI(I)/(8.*A*B)*((FE(I,J+1)-FE(I,J-1))
**(F(I+1,J)-F(I-1,J)))
*-(FE(I+1,J)-FE(I-1,J))**(F(I,J+1)-F(I,J-1)))/C5
D1=RFE-FE(I,J)
D2=RG-G(I,J)
IF (ABS(D1).LT..001.AND.ABS(D2).LT..001) L=L+1
FE(I,J)=FE(I,J)+FE*D1
G(I,J)=G(I,J)+FG*D2
F(I,J)=G(I,J)/EXP2Z(J)/SINFI(I)
21 CONTINUE
IFLAG=1
60 IF(L.EQ.50*79) GO TO 100
DO 8 I=2,60
GPP=(8.*FE(I,2)-FE(I,3)-7.*FE(I,1))/2./A/A
G(I,1)=G(I,1)+(GPP-G(I,1))/FG
P(I,1)=G(I,1)/X2(I)
8 CONTINUE
7 CONTINUE
100 WRITE(6,500) N, L
DO 10 I=1,61
WRITE(7,999) (FE(I,J),J=1,91)
WRITE(6,501) (FE(I,J),J=1,61,5)
CONTINUE
WRITE(6,505)
DO 14 I=2,60
DO 14 J=1,91

```

```

V(I,J)=S(I,J)/SINPI(I)/EXPZ(J)
14 CONTINUE
DO 13 I=1,61
  WRITE(6,501) (V(I,J),J=1,61,5)
  WRITE(3,973) (V(I,J),J=1,61)
13 CONTINUE
CDSKIN=0.0
DO 110 I=1,59,2
  CDSKIN=SINPI(I)**2*V(I,1)+4.*SINPI(I+1)**2*V(I+1,1)+SINPI(I+2)
  ***2*V(I+2,1)+CDSKIN
  CDSKIN=CDSKIN*4.0/RE/3.*B
  P1=0.0
  DO 111 J=1,79,2
    P1=P1+((V(2,J)*4.0-V(3,J))+4.*((V(2,J+1)*4.-V(3,J+1))+
  *(V(2,J+1)*4.-V(3,J+2)))/2.0
111 CONTINUE
  P1=1.0*B./RE*A/3.*B*B1
  P2(1)=0.0
  SINPI(63)=0.0
  COSPI(63)=0.0
  PT(63)=0.0
  DO 112 I=1,59,2
    II=I+2
    P2(II)=((-V(I,1)*3.+4.*V(I,2)-V(I,3))+(-V(I+1,1)*3.
    *+4.*V(I+1,2)-V(I+1,3))+4.+(-V(I+2,1)*3.0
    *+4.*V(I+2,2)-V(I+2,3)))/A/2.+((V(I,1)+V(I+1,1)*4.+V(I+2,1))+P2(I))
    PT(II)=P1+P2(II)*4.*RE/3.*B
    PT(1)=P1
    CDFORM=0.0
    DO 113 I=1,59,4
      CDFORM=CDFORM+PT(I)*COSPI(I)*SINPI(I)*2.+8.*COSPI(I+2)
      **SINPI(I+2)*PT(I+2)+2.*PT(I+4)*SINPI(I+4)*COSPI(I+4)
      CDFORM=CDFORM*4/1.5
      CDTT=CDFORM*CDSKIN
      WRITE(6,506)
      WRITE(6,507) RE,CDSKIN,CDFORM,CDTT,P1
      AMU=1.657E-4
      AIRLO=.9267E-3
      CRYLO=1.0
      RLRSO=3.*AMU**2/AIRLO/(CRYLO-AIRLO)*RE**2/32.*CDTT/990.
      RLR=PLRSO**(.1/3.)
      VTERM=AMU*RE/2./RLR/AIRLO
      RLR=RLR*10000.
      WRITE(6,508)
      WRITE(6,509) AMU,AIRLO,CRYLO
      WRITE(6,510) PLP,VTERM
500 FORMAT(//,15,' ITERATIONS REQUIRED ',',', TOTAL GOOD VALUES ',15)
501 FORMAT(/,2X,13F9.4)
505 FORMAT('1')
506 FORMAT('1',5X,'REYNOLD NO',7X,'CDSKIN',8X,'CDFORM',8X,
*'CDTT',8X,'PO')
507 FORMAT(/,5E15.5)
508 FORMAT(//,10X,'VISCOSITY',7X,'AIR DENSITY',6X,'DROP DENSITY')
509 FORMAT(/,3E20.5)
510 FORMAT(//,'RADIUS=',F8.2,', TERM. VEL.=',F8.3)
999 FORMAT(13F9.4)
STOP

```

APPENDIX III

COMPUTER PROGRAM FOR DROP TRAJECTORIES PAST
AN ICE CRYSTAL.

C
C TRAJECTORIES OF ICE CRYSTAL AND WATER DROP
C

C RUNGE-KUTTA METHOD TO START INTEGRATION

DIMENSION RPLZ(4),RLY(4),RVLY(4),RVSY(4),RVLZ(4),RASY(4)

*RVLY(4),RVSY(4),RALZ(4),RASY(4),W(61,81),U(61,81),

*Z(61,81),Y(61,81)

CONS=2.*9.267/1.567

AR=.05

ZIA= ALOG(SQRT((1.+AR)/(1.-AR)))

READ(7,100)RFYL,REYS,VTEFL,VTERP,AXISL,AXISS

WRITE(6,110)

WPITE(6,100)RFYL,VTEFL,VTERP,AXISL,AXISS

READ(7,101)DELT,S,TMAX,01,022,ZZ,YY

READ(7,102)VZ1,ALZ1,RSZ1,PSY1,VSY1,ASZ1,RSR,FLE

WPITE(6,101)DELT,S,TMAX,01,02,ZZ,YY

WRITE(6,851)VLZ1,ALZ1,RSZ1,PSY1,VSY1,ASZ1,RSR,PLR

DO 701 I=1,61

READ(7,102)(W(I,J),J=1,81)

701 CONTINUE

DO 702 I=1,61

READ(7,999)(U(I,J),J=1,81)

702 CONTINUE

DO 703 I=1,31

READ(7,999)(Z(I,J),J=1,51)

703 CONTINUE

DO 704 I=1,31

READ(4,999)(Y(I,J),J=1,51)

704 CONTINUE

DO 10 I=1,61

DO 10 J=1,81

W(I,J)=W(I,J)/.106*VSZ1

10 U(I,J)=-U(I,J)/.106*VSY1

ZAD=0.000

DO 20 N=1,6

DELT=DELT*S/1000.

50 WRITE(6,852)

CONFAC=CONS*RSR*AXISL*VTEFL

RLZ=0.0

RLY=0.000

VLZ=VLZ1

VLY=0.000

ALZ=ALZ1

ALY=0.000

RSZ=RSZ1

RSY=RSY1

VSZ=VSZ1

VSY=0.000

ASZ=ASZ1

ASY=0.000

RRLZ(1)=RLZ

RRLY(1)=RLY

RVLZ(1)=VLZ

RVLY(1)=VLY

RALZ(1)=ALZ

RALY(1)=ALY

PRSZ(1)=RSZ

FSY (1)=FSY
 VSG (1)=VSY
 RVSY (1)=VSY
 RA1= (1)=FSC
 FASY (1)=FASY
 DC (1)=I=1,2
 T=DELT*(1.0A1(1))
 ZFA=ZL+RLZ+RSL
 YFA=YY+LY+FSY
 ZSA=ZFA/FSR*RLF
 YSA=YFA/FSR*RLR
 AK1=DELT*Q1*(1.-(VLZ-UDR(ZSA,YSA,W)))
 AL1=DELT*(-Q1*(VLY-UDR(ZSA,YSA,U)))
 AN1=DELT*(-Q2*(VSY-UCR(ZFA,YFA,Y)))
 AM1=DELT*(Q1-Q2*(VSZ-UCR(ZFA,YFA,Z)))
 ZP1=ZFA+DELT/2.* (VSZ-VLZ)
 YF1=YFA+DELT/2.* (VSY-VLY)
 ZS1=ZF1/FSR*RLF
 YS1=YF1/FSR*RLR
 Q2=Q22*PLYS/(VSZ+AM1/2.-UCR(ZFA,YFA,Z))/CONFAC
 AK2=DELT*Q1*(1.-(VLZ+AK1/2.-UDR(ZS1,YS1,W)))
 AL2=DELT*(-Q1*(VLY+AL1/2.-UDR(ZS1,YS1,U)))
 AM2=DELT*(Q1-Q2*(VSZ+AM1/2.-UCR(ZF1,YF1,Z)))
 AN2=DELT*(-Q2*(VSY+AN1/2.-UCR(ZF1,YF1,Y)))
 ZP2=ZFA+DELT/2.* (VSZ-VLZ+(AM1-AK1)/2.)
 YF2=YFA+DELT/2.* (VSY-VLY+(AM1-AL1)/2.)
 ZS2=ZF2/FSR*RLF
 YS2=YF2/FSR*RLR
 Q2=Q22*PFYS/(VSZ+AM2/2.-UCR(ZP1,YF1,Z))/CONFAC
 AK3=DELT*Q1*(1.-(VLZ+AK2/2.-UDR(ZS2,YS2,W)))
 AL3=DELT*(-Q1*(VLY+AL2/2.-UDR(ZS2,YS2,U)))
 AM3=DELT*(Q1-Q2*(VSZ+AM2/2.-UCR(ZF2,YF2,Z)))
 AN3=DELT*(-Q2*(VSY+AN2/2.-UCR(ZF2,YF2,Y)))
 ZP3=ZFA+DELT*(VSZ-VLZ+(AM2-AK2)/2.)
 YF3=YFA+DELT*(VSY-VLY+(AN2-AL2)/2.)
 ZS3=ZF3/FSR*RLF
 YS3=YF3/FSR*RLR
 Q2=Q22*PLYS/(VSZ+AM3/2.-UCR(ZF2,YF2,Z))/CONFAC
 AK4=DELT*Q1*(1.-(VLZ+AK3-UDR(ZS3,YS3,W)))
 AL4=DELT*(-Q1*(VLY+AL3-UDR(ZS3,YS3,U)))
 AM4=DELT*(Q1-Q2*(VSZ+AM3-UCR(ZF3,YF3,Z)))
 AN4=DELT*(-Q2*(VSY+AN3-UCR(ZF3,YF3,Y)))
 RLZ=RLZ+DELT*(VLZ+(AK1+AK2+AK3)/6.)
 RLY=RLY+DELT*(VLY+(AL1+AL2+AL3)/6.)
 RSZ=RSZ+DELT*(VSZ+(AM1+AM2+AM3)/6.)
 RSY=RSY+DELT*(VSY+(AN1+AN2+AN3)/6.)
 VLZ=VLZ+(AK1+2.*AK2+2.*AK3+AK4)/6.
 VLY=VLY+(AL1+2.*AL2+2.*AL3+AL4)/6.
 VSZ=VSZ+(AM1+2.*AM2+2.*AM3+AM4)/6.
 VSY=VSY+(AN1+2.*AN2+2.*AN3+AN4)/6.
 DP=YY+RSY-RLY
 DH=Z2+RSZ-RLZ
 DHS=DH/RSR*RLR
 DPS=DP/RSF*RLR
 Q2=Q22*PEYS/(VSZ-UCR(ZF3,YF3,Z))/CONFAC
 AL2=Q1*(1.-(VLZ-UDR(DHS,DPS,W)))
 ALY=-Q1*(VLY-UDR(DHS,DPS,U))
 ASZ=Q1-Q2*(VSZ-UCR(DH,DP,Z))
 ASY=-Q2*(VSY-UCR(DH,DP,Y))
 WRITE(6,888) AK1,AK2,AK3,AK4,AL1,AL2,AL3,AL4,

111

VEL1=(V11+V12)/2, RAL1, RLY1, RSY1, R37, P
 RVL1=(V11-V12)/2, RLY1, RSY1, RAS1, RLT1, R38, ASY
 RFLZ1=0
 RVL1P=V11
 RAL1P=V12
 RLY1P=V13
 RSY1P=V14
 RVS1=(V11+V12)=VRS1
 RAS1=(V11-V12)=RAS1
 RPL1=(V11-V12)=RSY1
 RVSY1=(V11+V12)=VSY1
 RASY1=(V11-V12)=RASY1
 CONTI
 WRITB(1,1)
 BANTING'S PREDICTOR-CORRECTOR-MODIFIER METHOD
 T=0, *DP, *Z
 T0=4, *DP, *Z
 VL1=RP=V11+(4)
 VL2=RP=V12+(4)
 VLY1P=VLY1+(4)
 VLY2C=VLY1+(4)
 VSZ3P=PVSZ1+(4)
 VSZ3C=PVSZ1+(4)
 VSY3P=PVSY1+(4)
 VSY3C=PVSY1+(4)
 VLZ4P=VVLZ1+(1)+4./3.*((2.*RALZ1)-RALZ2)+2.*RALZ3)*DELT
 VSZ4P=VVSZ1+(1)+4./3.*((2.*RASZ1)-RASZ2)+2.*RASZ3)*DELT
 VLZ4M=VLZ4P+12./121.*((VLC3P-VLZ3C))
 VSZ4M=VSZ4P+12./121.*((VSZ3P-VSZ3C))
 VLY4P=VLY1+(1)+4./3.*((2.*RALY1)-RALY2)+2.*RALY3)*DELT
 VSY4P=PVSY1+(1)+4./3.*((2.*RASY1)-RASY2)+2.*RASY3)*DELT
 VLY4M=VLY4P+12./121.*((VLY3P-VLY3C))
 VSY4M=VSY4P+12./121.*((VSY3P-VSY3C))
 RLZ4=.125*((9.*RPLZ4)-RRLZ2)+3.*DELT*(VLZ4M+2.*RVLZ4-(VVLZ1))
 RSZ4=.125*((9.*RPSZ4)-RPSZ2)+3.*DFIT*(VSZ4M+2.*RVSZ4-(VVSZ1))
 RLY4=.125*((9.*RPLY4)-RPLY2)+3.*DELT*(VLY4M+2.*PVLY4-(VLY1))
 RSY4=.125*((9.*RRSY4)-RSY2)+3.*DELT*(VSY4M+2.*RVSY4-(VSY1))
 DH=2Z+RSZ4-PLZ4
 DP=YY+RSY4-RLY4
 DHS=DH/FSR*RLR
 DPS=DP/FSR*RLP
 Q2=Q22*PFYS/(VSZ4A-UCP(DH,DP,Z))/CONFAC
 LZ4=Q1*(1.+((VLZ4M-UDR(DHS,DPS,W))))
 LY4=-Q1*((VLY4M-UDR(DHS,DPS,W)))
 SZ4=Q1-Q2*(VSZ4M-UCR(DH,DP,Z))
 SY4=-Q2*(VSY4M-UCR(DH,DP,Y))
 L24C=.125*((9.*RVLZ4)-FVLZ2)+3.*DELT*(ALZ4+2.*RALZ4-(RALZ3))
 S24C=.125*((9.*RVSZ4)-FVSZ2)+3.*DELT*(ASZ4+2.*RASZ4-(RASZ3))
 LZ4F=VLZ4C+9./121.*((VLZ4P-VLZ4C))
 SZ4F=VSZ4C+9./121.*((VSZ4P-VSZ4C))
 LY4C=.125*((9.*EVLY4)-FVLY4)+3.*DELT*(ALY4+2.*RALY4-(RALY3))
 SY4C=.125*((9.*PVSY4)-FVSY4)+3.*DELT*(ASY4+2.*RASY4-(RASY3))
 LY4F=VLY4C+9./121.*((VEY4P-VLY4C))
 SY4F=VSY4C+9./121.*((VSY4P-VSY4C))
 LZ4=.125*((9.*PPLZ4)-RRLZ2)+3.*DELT*(VLZ4F+2.*RVLZ4-(RVLZ3))
 S24=.125*((9.*RRSZ4)-RPSZ2)+3.*DELT*(VSZ4F+2.*RVSZ4-(RVSZ3))

RY4=+1.0*(1.0*ALY4(-1)+1.0*VLY4)+1.0*PLT*(VLY4P+2.*EVLY(4)-EVLY(3))
RY4=+1.0*(1.0*PLT*(4)+1.0*VLY(-1)+1.0*PLT*(VLY4P+2.*EVSY(4)-EVSY(3)))
DLY4Y+RSY4-RVY4

DIF=DP-M1F

IF(G>0. GT. 1.) GO TO 510

DLZ4Z+1.574-PI/2

DPS=DZ4Z*I*112

DPS=DP/E*57.111

DPS=0.72*I*RY4/(VLY4P-UCP(DH,DP,1))/CONFAC

ALY4=Q1*(1.-(VLY4P-UDE(DHS,PPS,0)))

ALY4=-Q1*(VLY4P-UDE(DHS,PPS,0))

ASZ4=Q1-Q2*(VSZ4P-UCE(DH,DP,2))

ASY4=-Q2*(VSY4P-UCR(DH,DP,Y))

DPOV=DP/COSH(ZTA)

IF(DPOV.GT.1.) DPOV=1.

ZAD=COS(A*SIY(DPOV))*SINH(SIY)*FLOAT(2*N-1)*RSP

IF(DH-ZAD)501,501,510

IF(TMAX.LT.T) GO TO 501

IF(DH.GT.1.0) GO TO 521

IF(TK-.10) 521,522,522

WPLTF(6,850) DP,DH,PIY4,ILZ4,RSY4,RSZ4,T

WPLTF(6,851) VL24T,VLY4P,VSZ4P,VSY4P,ALY4,ASZ4,ASY4

TK=-DELT

TK=TK+DELT

DO 4 1-1,3

RALZ(I)=RALZ(I+1)

RVLZ(I)=RVLZ(I+1)

FRIZ(I)=FLZ(I+1)

RALY(I)=RALY(I+1)

RVLY(I)=RVLY(I+1)

FPLY(I)=FPLY(I+1)

RASZ(I)=RASZ(I+1)

RVSZ(I)=RVSZ(I+1)

RRSZ(I)=RRSZ(I+1)

RASY(I)=RASY(I+1)

RVSY(I)=RVSY(I+1)

PRSY(I)=RSY4(I+1)

CONTINUF

RALZ(4)=ALZ4

RVLZ(4)=VLZ4P

VLZ3P=VLZ4P

VLZ3C=VLZ4C

FRILZ(4)=FLZ4

RALY(4)=ALY4

RVLY(4)=VLY4P

VLY3P=VLY4P

VLY3C=VLY4C

RRLY(4)=PLY4

RASZ(4)=ASZ4

RVSZ(4)=VSZ4P

VSZ3P=VSZ4P

VSZ3C=VSZ4C

RRSZ(4)=PSZ4

RASY(4)=ASY4

RVSY(4)=VSY4P

VSY3P=VSY4P

VSY3C=VSY4C

PRSY(4)=RSY4

GO TO 3

511 WRITE(6,714)
 WRITE(6,715) YY, YAD, ZAD, EYY4, RLY4, RSZ4, RLZ4
 WRITE(6,716) YY-YY-15P/2.
 20 CONTINUE
 101 FORMAT(0.000,0)
 110 GO TO 1,10 CRYSTAL IF DROPLET V CRYSTAL V DROPLET R CRYSTAL
 * R DROPLET)
 101 FORMAT(7E12.4,7E15.4,7E10.2)
 102 FORMAT(8E5.4)
 600 FORMAT(//,6X,'SY1',8X,'YAD',8X,'ZAD',8X,'RSY4',8X,'RLY4',
 *8X,'RSZ4',8X,'RLZ4')
 399 FORMAT(12E9.4)
 850 FORMAT(7E15.5)
 851 FORMAT(8E15.9)
 852 FORMAT(//)
 700 FORMAT(//,7E12.4)
 652 FORMAT(//,1 TIME USED = 1,18.3,1 SECONDS)
 STOP
 END
 FUNCTION FCR(PX, PY, P)
 DIMENSION R(31,51),R(4)
 AR=.05
 A1=.1
 B1=6.*3.1416/180.
 ZIA= ALOG(SQRT((1.+AR)/(1.-AR)))
 AZ=ABS(PZ)
 AY=ABS(EY)
 IF(AY.GT.0.0)GO TO 1
 ZIN= ALOG(AZ+SQRT(AZ*AZ+1.))
 ANG=0.0
 GO TO 49
 1 IF(AZ.GT.0.0)GO TO 2
 ZIN=0.0
 ANG=1.5708
 GO TO 49
 2 Y2=AY*AY
 Z2=AZ*AZ
 C=Y2+Z2-1.
 B2P4AC=C**2+4.*Z2
 X=(C+SQRT(B2P4AC))/2.
 SINHAN=SQRT(X)
 IF(SINHAN=0.)40,40,41
 40 ZIN=0.0
 ANG=0.0
 GO TO 49
 41 SRSQP1=SQRT(SINHAN*SINHAN+1.)
 ZIN= ALOG(SINHAN+SRSQP1)
 COSAN=AZ/SINHAN
 IF(COSAN.GE.1.0) GO TO 56
 ANG=ARCOS(COSAN)
 GO TO 49
 56 ANG=0.0
 49 IF(RZ.GT.0.0)GO TO 50
 ANG=3.141596-ANG
 50 ZIN2=(ZIN-ZIA)/A1+1.
 ZIN2=(ZIN-ZIA)/A1+1.
 ANG2=ANG/B1+1.
 NZIN=ZIN2

NANG=ANG
 111 IF (NANG-1) 114, 120, 111
 112 IF (NANG-5) 112, 120, 115
 113 IF (NANG-3) 110, 120, 123
 114 NZIN=1
 GO TO 120
 115 NZIN=50
 120 IF (NANG-1) 121, 130, 122
 121 NANG=1
 GO TO 130
 122 IF (NANG-31) 101, 123, 123
 123 NANG=30
 C BI-LINEAR INTERPOLATION-EXTRAPOLATION
 130 NZINP1=NZIN+1
 NANGP1=NANG+1
 DZIN=ZIN2-FLOAT(NZIN)
 DANG=AANG1-FLOAT(NANG)
 UCR=P(NANG,NZIN)+(P(NANG,NZINP1)-P(NANG,NZIN))*DZIN
 \$+(P(NANGP1,NZIN)+P(NANG,NZIN))*DANG+(P(NANG,NZIN)
 \$+P(NANGP1,NZINP1)-P(NANGP1,NZIN)-P(NANG,NZINP1))*DANG*DZIN
 GO TO 3
 C BI-QUADRATIC INTERPOLATION
 140 DZIN=ZIN2-FLOAT(NZIN)
 DANG=AANG2-FLOAT(NANG)
 NZINP2=NZIN+2
 NZINP1=NZIN+1
 NZINM1=NZIN-1
 FCT=(DZIN**2-DZIN)/4.
 FFT=(DANG**2-DANG)/4.
 DO 145 I=1,4
 N=NANG-2+I
 B(L)=P(N,NZIN)+(P(N,NZINP1)-P(N,NZIN))*DZIN+(P(N,NZINM1)
 \$+P(N,NZINP2)-P(N,NZIN)-P(N,NZINP1))*FCT
 145 CONTINUE
 UCR=B(2)+(B(3)-B(2))*DANG+(B(1)+B(4)-B(2)-B(3))*FFT
 3 RETURN
 END
 FUNCTION UDP(RZ,RY,P)
 DIMENSION P(61,81),BB(4)
 B1=3./180.*3.1416
 A1=.05
 AZ=ABS(RZ)
 AY=ABS(RY)
 IF(AY.GT.0.0) GO TO 1
 ZSP= ALOG(AZ)
 ANG=0.0
 1 IF (AZ.GT.0.0) GO TO 2
 ZSP=0.0
 ANG=1.5708
 GO TO 49
 2 ZSR= ALOG(SQRT(AZ*AZ+AY*AY))
 IP(ZSP.LT.0.0) ZSP=0.0
 ANG=3.1416-ATAN(AY/AZ)
 IP(BZ.LT.0.0) ANG=3.1416-ANG
 ZIN2=ZSP/A1**.
 ANG2=ANG/B1**.
 XZIN=ZIN2
 NANG=ANG2
 IP(NZIN-1) 114, 120, 111

```

111 IF (NAN-1) 120,130,140
112 IF (NANG-60) 140,130,120
114 NZIN=1
115 GO TO 120
116 UDR=0.0
117 GO TO 120
120 IF (NANG-1) 130,130,120
121 NANG=1
122 GO TO 130
123 IF (NANG-61) 130,120,120
124 NANG=60
C BI-LINEAR INTERPOLATION-EXTRAPOLATION
130 NZINP1=NZIN+1
131 NANGP1=NANG+1
132 DZIN=ZIN2-FLOAT(NZIN)
133 DANG=ANG2-FLOAT(NANG)
134 UDR=P(NANG,NZIN)+(P(NANG,NZINP1)-P(NANG,NZIN))*DZIN
135 +(P(NANGP1,NZIN)-P(NANG,NZIN))*DANG+(P(NANG,NZIN)
136 +P(NANGP1,NZINP1)-P(NANGP1,NZIN)-P(NANG,NZINP1))*DANG*DZIN
137 GO TO 2
C BI-QUADRATIC INTERPOLATION
140 DZIN=ZIN2-FLOAT(NZIN)
141 DANG=ANG2-FLOAT(NANG)
142 NZINP2=NZIN+2
143 NZINP1=NZIN+1
144 NZINM1=NZIN-1
145 FCT=(DZIN**2-DZIN)/4.
146 FET=(DANG**2-DANG)/4.
DO 145 L=1,4
N=NANG-2+L
BB(L)=P(N,NZIN)+(P(N,NZINP1)-P(N,NZIN))*DZIN+(P(N,NZINM1)
$+P(N,NZINP2)-P(N,NZIN)-P(N,NZINP1))*FCT
145 CONTINUE
UDR=BB(2)+(BB(2)-BB(1))*DANG+(BB(1)+BB(4)-BB(2)-BB(3))*FET
3 RETURN
END

```

FILE